/
Article / Book Information

( )	
Title(English)	Microscopic study on fluorescence properties of polyfluorene
( )	
Author(English)	Tomonori Nakamura
( )	: , : , : 11950 , :2021 3 26 , : , :VACHA MARTIN, , , ,
Citation(English)	Degree:Doctor (Engineering), Conferring organization: Tokyo Institute of Technology, Report number: 11950 , Conferred date:2021/3/26, Degree Type:Course doctor, Examiner:,,,,
( )	
Type(English)	Doctoral Thesis

Microscopic study on fluorescence properties of polyfluorene

顕微鏡を用いたポリフルオレンの発光特性に関する研究

Tomonori Nakamura

School of Materials and Chemical Technology

Tokyo Institute of Technology

Contents

Chapter I: General introduction

Chapter II: Intrachain Aggregates as the origin of green emission in polyfluorene

Chapter III: Mechanically induced changes of PL properties in single PFO nanoparticles

Chapter IV: Simultaneous nanofishing and SMS study of single π conjugated polymers: Towards the direct control of conformation and fluorescence properties

Chapter V: Conclusion and outlook

Chapter I

General Introduction

1-1. π conjugated polymers

1-1-1. History of π conjugated polymers

Organic materials are mainly composed of carbon and hydrogen, and may include oxygen, nitrogen, and so on. Many classes of materials are categorized as organic materials, for example, petrochemical products or natural products such as proteins and cellulose. Once, organic materials were considered and used as insulating materials. Some organic crystal such as anthracene and naphthalene were shown to exhibit photoconductivity in 1950s [1-3]. In 1970s, H. Shirakawa, A.G. MacDiarmid and A.J. Heeger discovered π conjugated polymers which show high electronic conductivity by chemical doping. The three scientists received Nobel Prize in chemistry in 2000 for "the discovery and development of electronically conductive polymers" [4-10]. This discovery created a new field, polymer electronics. In 1980s, C. W. Tang made and reported the first organic light emitting diode (OLED) and organic photovoltaic (OPV) cell based on amorphous films of small organic molecules [11]. At the same time, A. Tsumura et al yielded the first organic field effect transistor (FET) device based on polythiophene [12-13]. Afterwards, J. H. Burroughes et al developed the first polymer light emitting diodes (PLEDs) using poly (p-phenylene vinylene) (PPV) [14]. These pioneering works received great attention from all over the world and many researchers devoted their efforts to improve performance of these devices. Because of these efforts, OLED display was released for the first time by SONY in 2007. Currently, several companies produce OLED displays for TV sets and mobile devices for wide and increasing public use. In 2020, the market size of OLED displays has been over 1000 million dollars [15].

1-1-2. Structure of π conjugated polymers

π conjugated compounds have unique structure, in which constituent atoms are connected by alternating single and multiple bonds. Carbon atom has 6 electron and its electronic configuration is $1s^2 2s^2 2p^2$. There are two unpaired p electron in outer shell which can bond with other atoms. However, this is not a correct electronic configuration of a carbon atom when it connects with other atoms. Actually, one 2s electron transfers to a 2p orbital and mixes to generate a new orbital. This is called "hybridization". There are three hybridized orbitals: sp^3, sp^2 and sp (Fig. 1-1).
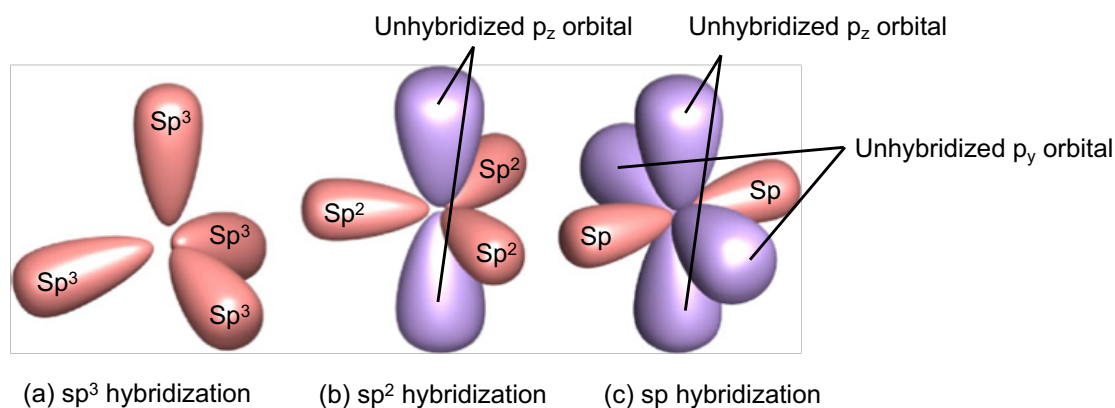
Fig. 1-1 Spatial arrangement of sp^3, sp^2, sp orbitals [16]

The sp^3 orbital is created by combining one 2s electron and three 2p electrons (Fig. 1-2). It can form four σ-bonds with neighboring atoms which are strongly localized in σ-orbital and they are classified as single bonds. The bond angle between adjacent σ-bonds is 109.5° (Fig. 1-1 (a)).
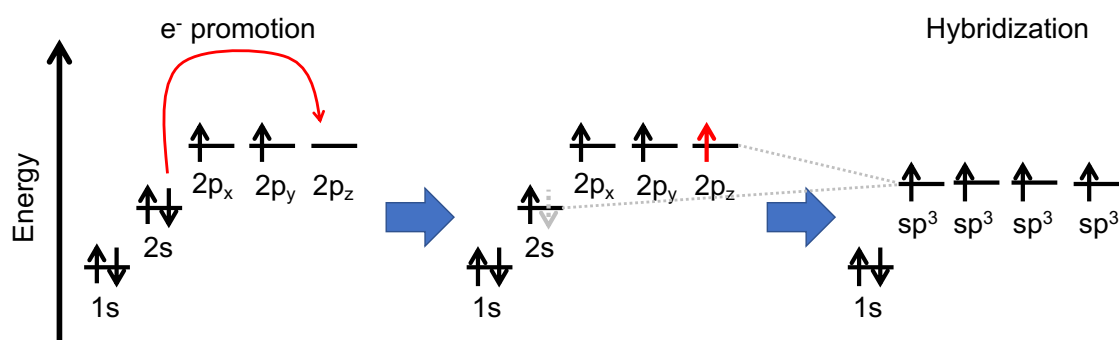
Fig. 1-2 Energy level of sp^3 orbital

The sp^2 orbital is created by combining one 2s electron and two 2p electrons (Fig. 1-3). It can form three σ-bonds with neighboring atoms. These are coplanar and the bond angle between adjacent σ-bonds is 120° (Fig.1-1(b)). The remaining one 2p electron is located perpendicular to the plane of the sp^2 orbital. If a neighboring atom also has an unpaired 2p electron, an additional π-bond will be formed by overlapping of the two 2p electrons. π electrons are delocalized between neighboring atoms and positioned above and below the plane of the σ-bond (Fig. 1-4). In addition to the one σ-bond there is the π-bond, and overall the bond between the two atoms is classified as double.
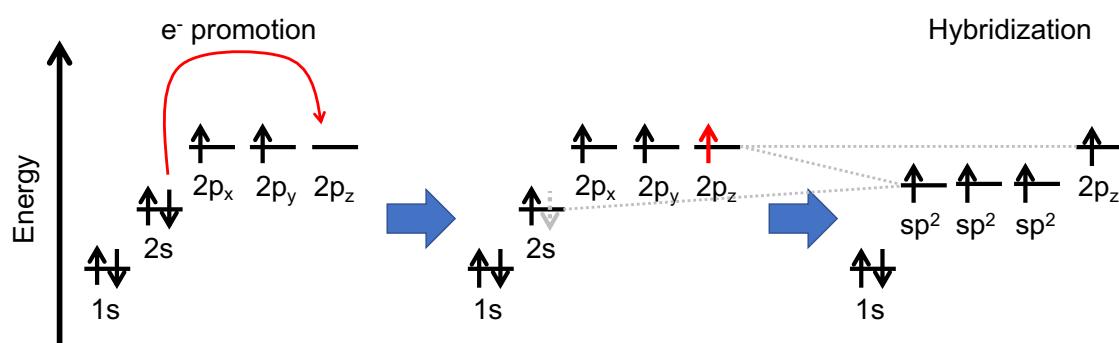
Fig. 1-3. Energy level of sp^2 orbital
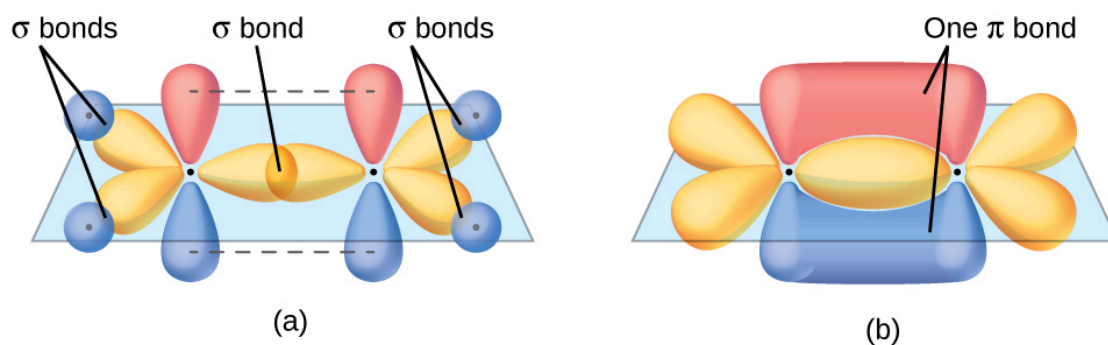
Fig. 1-4 Electronic orbital of ethylene ($_2$HC=CH$_2$) [17]

The sp orbital is created by combining one 2s electron and one 2p electron (Fig. 1-5). It can form two σ-bonds with neighboring atoms. Bond angle between the adjacent σ-bonds is 180º (Fig. 1-1(c)). In the case of acetylene (HC≡CH), the remaining two 2p electrons form two π bonds. (Fig. 1-6). Overall, the bond has one σ-bond and two π bonds, and is classified as a triple bond.
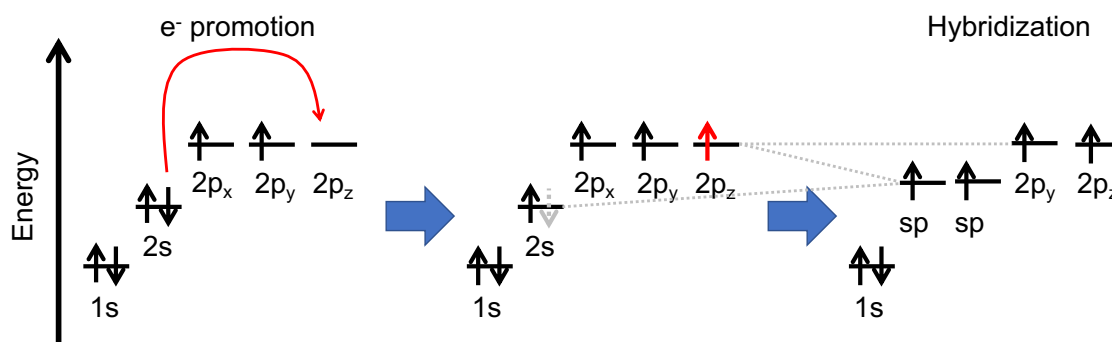
Fig. 1-5. Energy level of sp orbital
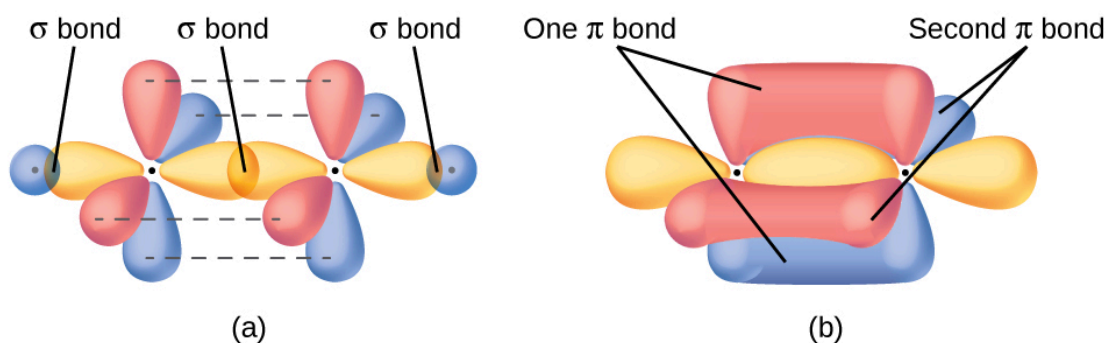
Fig. 1-6 Electronic orbital of acetylene (HC≡CH) [17]

By overlapping two 2p atomic orbitals, two molecular orbitals, called π bonding molecular orbital and π^* antibonding molecular orbital are created. π bonding molecular orbital and π^* antibonding molecular orbital have lower and higher energy compared to the 2p atomic orbital, respectively. Because every 2p orbital has one electron, the π orbital has two electrons and only the π bonding molecular orbital is occupied. If the molecule has a structure with alternating single and multiple bonds, such as buta-1,3-diene, (E)-hexa-1,3,5-triene, (3E,5E)-octa-1,3,5,7-tetraene, or conjugated polymers, the π electron extends and delocalizes along the molecular backbone. As the number of π electrons increases, more and more π bonding molecular orbitals and π^* antibonding molecular orbitals are created (Fig. 1-7). Among them, there are π bonding molecular orbitals with highest energy called highest occupied molecular orbital (HOMO), and π^* antibonding molecular orbitals with lowest energy called lowest unoccupied molecular orbital (LUMO). The energy difference between HOMO and LUMO is called band gap energy which induces semiconducting properties.
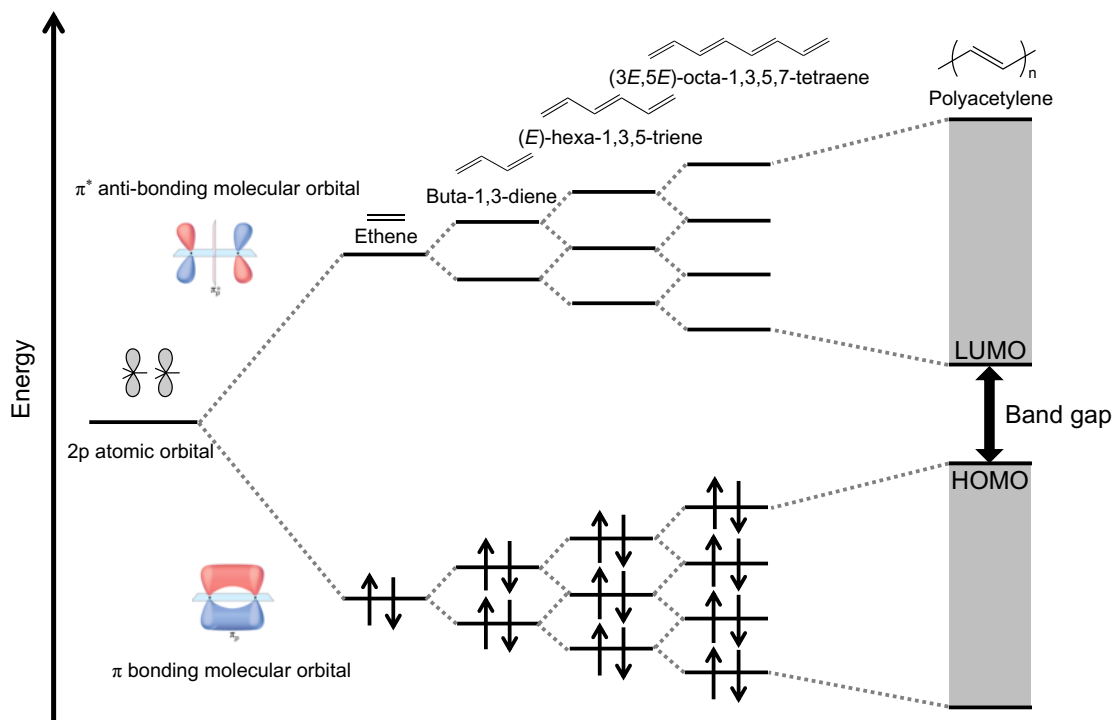
Fig. 1-7 Energy band gap of conjugated molecules [18]

1-1-3. Effective conjugation length

If the number of π electrons increases to infinity, it can be expected that the band gap energy goes to zero and the π conjugated compound will be a metal. However, the band gap energy of a π conjugated polymer will not be zero because bond alternations and twists of the main chain. In an ideal 1-D chain, all 2p electrons would form one π orbital and all bond lengths would be equal. However, a dimerized chain is stabilized because electrons are interacting with phonons. As a result, there are two minimum points of the electron potential energy. Therefore, the actual π-conjugated compounds reversibly take these two states. The bond lengths are not equal and the band gap energy will not be zero. This phenomenon is called "bond alternation" or "Peierls distortion". [19]

To overlap 2p orbitals to form a π orbital, the two 2p orbital should be parallel. Therefore, every monomer unit should be on the same plane. However, π conjugated compounds can interact with other chains and solute molecules in solid state and solution.

In addition, alkyl chains are incorporated as side chains to help dissolve the π-conjugated compounds in organic solvents. As a result, the molecular backbone is locally distorted and prevented from forming a π orbital. This is another reason why π conjugated length is limited. As an oligomer size increases, π conjugated system is expanded and absorption wavelength will be red-shifted. When the oligomer size increases more than a certain number of monomers, absorption wavelength will not be shifting further (saturated). This certain number of monomers is termed "effective conjugation length". Several oligomers have been investigated for their effective conjugation length. Their effective conjugation length are around 10 monomer units [20]. The maximum effective conjugation length that has been reported is 96 monomer units of polythiophene derivatives [21].

1-2. Polyfluorene

1-2-1. What is polyfluorene?

Polyfluorene (PF) is one of the ladder types of poly(p-phenylene) (PPP) derivatives (Fig. 1-8). PPP is known as blue light emitting polymer. PPP is easily twisted, resulting in emission with a hypochromic shift to the ultra violet (UV) region. To solve this problem, PF which has a structure with two phenylene rings connected by methylene bridge for keeping the backbone planar, was synthesized in 1989 [22-23]. As a result, PFs show good blue emission properties and have attracted much attention as a material for organic light emitting diodes.
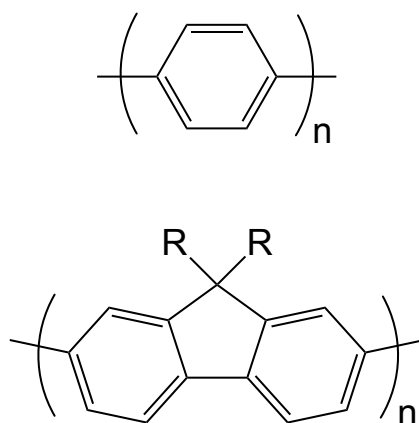
Fig. 1-8 Chemical structure of PPP and PF

1-2-2. Functionalization of polyfluorene

Methylene bridge, or 9-position carbon, has high acidity because fluorenyl anion is stabilized by resonance effect. Therefore, functional groups can be easily incorporated into the 9-position carbon as side chains to induce additional function without affecting the main chain planarity. Alkyl chains are often introduced to enhance solubility in organic solvents and control morphology [24]. Bis(3,6-dioxaheptyl) and ionic side chains such as imidazolium and bis(4-sulfonatobutyl) groups improved solubility against polar solvents and enhanced charge carrier mobility [25-28]. Bulky dendron side chains prevent the formation of aggregates [29]. Phenyl group is more difficult to be oxidized than alkyl chain and can increase photostability of polyfluorene [30-33].

1-2-3. Polyfluorene copolymers

Controlling the bandgap energy, morphology and carrier mobility of π-conjugated polymers is very important for OLED and OPV devices. Copolymerization is one of the good ways to control such properties. A lot of polyfluorene copolymers have been reported so far due to their ease of synthesis for improving the performance of OLED and OPV devices [34-47].

F8BT, TFB and PFB are typical copolymers that have been widely studied for OLED and OPV devices. F8BT shows unusually high electric transport property and good green emission property. TFB and PFB are good hole transport materials. F8BT and TFB or PFB are often blended because blended films show vertically segregated structures. Film morphology affects charge transport, charge recombination and photogeneration of charges. Therefore, the copolymers are suitable materials to study the relationship between those properties and the chain morphology [48-59].

Polyfluorene copolymers with thiophene derivatives are another typical example of PF copolymer. Several thiophene derivative copolymers have been synthesized to control band gap energy and used for OLED and OPV. Tuning of emission color from green to red region has been achieved using such copolymers [60-66].

1-2-4. β phase of polyfluorene

PF homopolymer has been used to study the effect of conformation and morphology on photophysical properties because it is known to have three phases termed α, β, γ phase which have different average torsional angles of main chain (φ) [67]. The α phase is amorphous and has the most twisted conformation (φ = 135°). It can be prepared by spin-coating from PF solution in organic solvents such as toluene and THF [68-69]. The γ phase is a crystalline phase with φ of 150° and is formed by thermal treatment [70]. Of the three phases, the β phase is attracting the most attention because its OLED devices show excellent performance [71-73]. The β phase has the most planar conformation (φ = 160°) and has been prepared by spin-coating from poor solvent, by addition of small amount of high boiling-point solvent into processing solvent, by thermal treatment and solvent vapor annealing [69, 74-78]. In the initial studies, the β phase was considered an aggregate of PFs which is observable only in solid films [79-80]. X-ray diffraction measurement revealed that the polymer chain is highly extended in the aggregate [81-82]. Several researchers studied the formation mechanism of β phase [83-85]. As a first step, the β phase conformation is formed in a PF single chain. However, single β phase chain can be easily disrupted by external forces such as heat and diffusion of surrounding molecules. In solid state, single β phase chain is stabilized by interchain interactions and acts as nucleus to promote the β phase formation of surrounding PF chains. While interchain interaction is needed to form β phase, polymer chain should move to change conformation. Some studies indicate that moderate interchain interaction is necessary to increase β phase content [86-88]. Molecular weight of PF also influences the β phase formation [89-91]. Higher molecular weight of PF can induce larger fraction of β phase conformation because of moderate interchain interaction. Alkyl side chain length is another parameter relevant for the β phase formation. Monkman group investigated β phase formation of PFs with different alkyl side chain lengths of 6 ~ 10 (PF6, PF7, PF8, PF9 and PF10) [92-93]. The ease of β phase formation depends on two factors. One is the dimer/aggregate formation efficiency which is lower for longer alkyl side chains. Another one is the Van der Waals bond energy available to overcome the steric repulsion to planarize main chain which is lower for shorter alkyl chain. To planarize backbone, a

tentative value of (15.6 ± 2.5) kJ mol^{-1} per monomer of the energy is required. PF9 and PF10 have long side chains which prevent forming β phase because of a low dimer/aggregate formation efficiency. PF6 and PF7 have short side chains and too low the Van der Waals bond energy to form the β phase. PF8 has the most balanced side chain length and preferentially form β phase.

Formation of the β phase leads to expansion of the π conjugation and affects the PF photophysical properties. β phase shows a new absorption peak at around 437 nm (Fig-1-9(a)). Excitation energy is completely transferred to the β phase segments from the amorphous phase when they coexist in the chain and when the latter is excited. Therefore, fluorescence peak is red shifted to around 440 nm and shows narrow and clear vibronic structure (Fig-1-9(b)). W. C. Tsoi et. al. synthesized several sizes of oligofluorene and investigated the effective conjugation length [94]. The effective conjugation lengths of the amorphous and β phases determined by comparing the first peak of fluorescence are 8 ± 1 and 30 ± 12 monomer units, respectively. Because of the expanded π conjugation length, the transition energy is reduced by about 0.13 eV, and hole mobility increases more than an order of magnitude [95-96]. PL quantum yield (PLQY) of β-phase was studied by several groups [69, 76, 97]. However, the reported PLQY values were obtained from differently treated films and ranged from 0.5 to 0.7, indicating that film morphology and associated interchain interactions affect the PLQY.
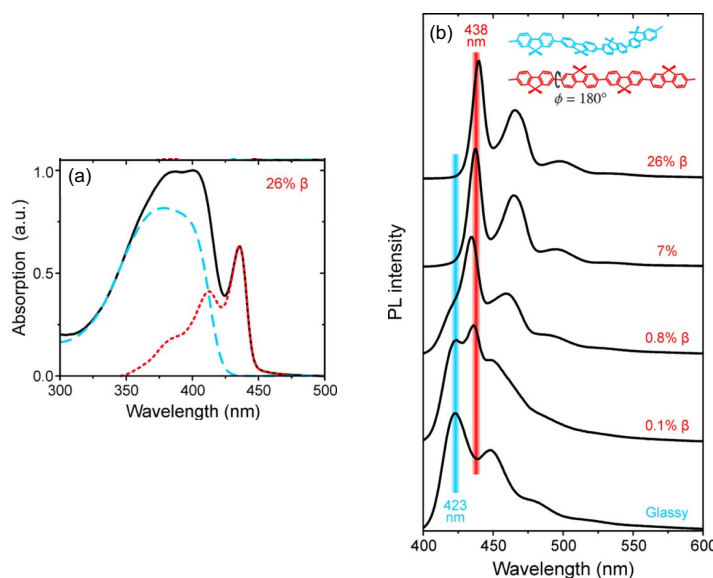
Fig. 1-9 (a) Absorption and (b) PL spectra of PFs including β-phase [69]

1-2-5. Green emission of polyfluorene

Although polyfluorenes are expected to be blue emitting materials, they often show unwanted green emission (Fig. 1-10) [98], called g-band. The g-band appears as a result of prolonged UV irradiation in air, thermal treatment, or extended operation in electroluminescent (EL) devices. The appearance of the g-band is always accompanied by a decrease of color purity and overall quantum efficiency. Therefore, the cause of the g-band has been widely studied for over 20 years with the aim to suppress this undesirable emission. Two different mechanisms, aggregation and oxidation of PF chains have been proposed as the potential cause of the g-band. However, it is not clear which of the two is the main cause of the g-band. The details of the cause of the g-band are discussed in Chapter II.
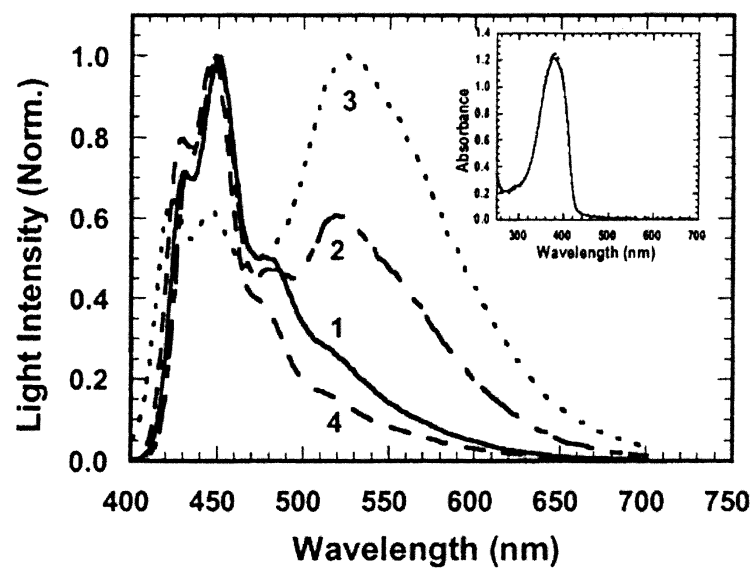
Fig. 1-10 Fluorescence spectra of PF, (a) pristine film, (b) annealed at 150 in air, and (c) at 200 in N_2. (4) PF film annealed at 200 in air and quenched in methanol-dry ice bath. [98]

1-3. Basic photophysical properties

1-3-1. Photophysical processes

Molecular electronic states, vibrational states and photophysical processes are described by Jablonski diagram as shown in Fig. 1-11. The lowest energy state is called "ground state (S_0)" and the higher energy states are called "excited states". There are two kinds of excited states, namely singlet (S_n) and triplet (T_n) states. They are characterized by total spin-momentum of the two unpaired electrons. Singlet excited state is composed of two electrons with a total spin momentum of zero. On the other hand, triplet excited state has two electrons with a total spin momentum equal to unity. In organic molecules, ground state (S_0) is singlet state because two electrons cannot have the same four electronic quantum numbers (Pauli exclusion principle). Absorption of a photon can promote electron from ground state (S_0) only to a singlet excited state (S_n) because the spin multiplicity of the initial and final states have to be same for a spin-allowed transition. After the transition to higher singlet excited state (S_n), fast non-radiative transition occurs to higher vibrational levels of a lower singlet excited state (S_{n-1}) which is of the same spin multiplicity. This process is called internal conversion (IC). After that, the excess vibrational energy can be transferred to the surrounding environment and lead to occupation of the lowest vibrational level of the S_{n-1} state by a process called vibrational relaxation (VR). By repeating IC and VR, the molecule will finally end up in the S_1 state at the lowest vibrational level. IC from S_1 to S_0 is much slower than that between higher excited states ($S_n \rightarrow S_{n-1}$) because the energy gap between S_1 and S_0 is much larger. Therefore, IC, radiative transition (emission) and intersystem crossing (ISC) can be competent processes. ISC is a non-radiative transition between two electronic states with different spin multiplicity. For example, a molecule can occupy T_1 with lowest vibrational energy by VR following ISC from S_1 to higher vibrational levels of T_1. Emission is a radiative process between two electronic states. When the spin multiplicities of the initial and final states are same, the process is called fluorescence. On the other hand, when the spin multiplicities are different, it is called phosphorescence. While fluorescence is a spin-allowed transition, phosphorescence is a spin-forbidden process. Therefore, fluorescence

occurs much faster than phosphorescence. Because the ground state is a singlet state, fluorescence and phosphorescence occur from singlet and triplet excited states, respectively. All radiative transitions, as well as ISC, generally occur from the lowest vibrational level of the lowest excited state (S_1 or T_1). This phenomenological observation is called Kasha's rule.
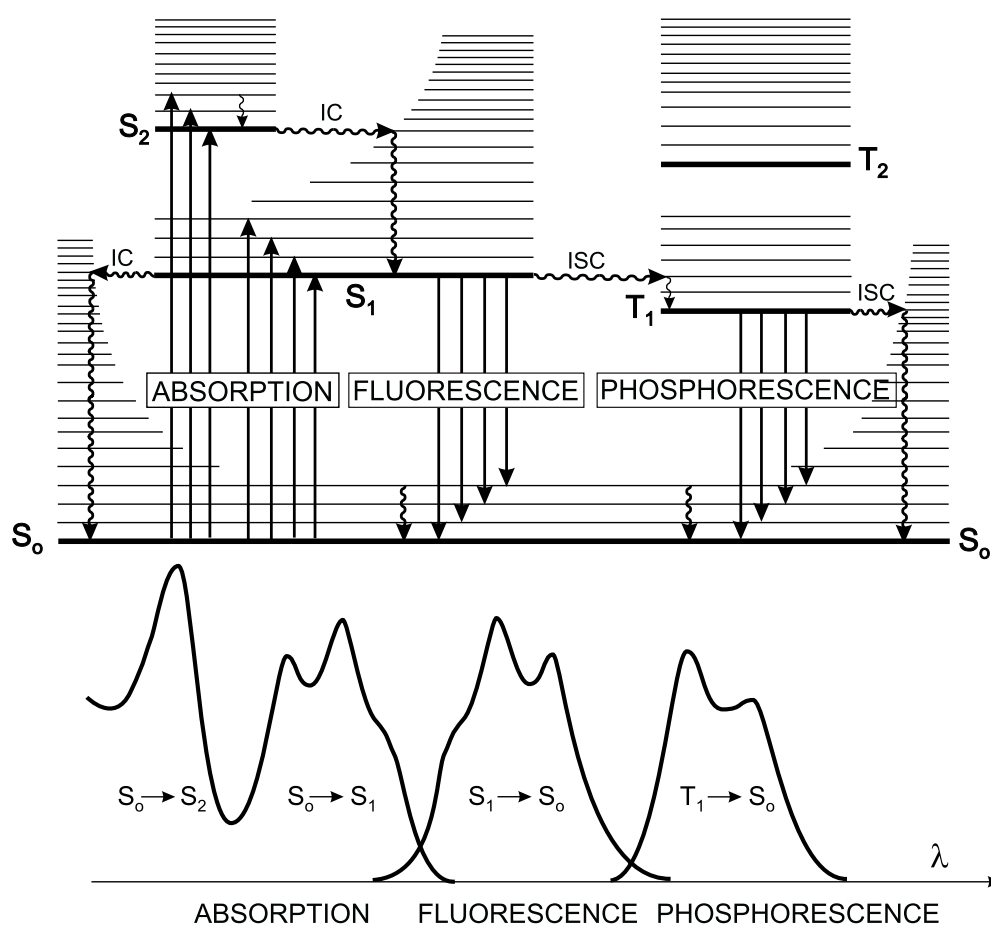
CHARACTERISTIC TIMES		
absorption	10^{-15} s	
vibrational relaxation	10^{-12}-10^{-10} s	
lifetime of the excited state S_1	10^{-10}-10^{-7} s	→ fluorescence
intersystem crossing	10^{-10}-10^{-8} s	
internal conversion	10^{-11}-10^{-9} s	
lifetime of the excited state T_1	10^{-6} -1 s	→ phosphorescence

Fig. 1-11 Jablonski diagram [99]

1-3-2. Molar extinction coefficient and absorption cross section

Absorption property of a molecule is characterized by its absorption spectrum which is a dependence of, e.g., absorbance on the wavelength of the incident light. The absorbance is described by Lambert Beer equation shown below.

$$A = \varepsilon c l \tag{1-1}$$

Where A is absorbance, the parameter ε is called molar extinction coefficient, c is the concentration of molecule and l is the distance that light passes through sample. c and l depend on experimental conditions. ε is a property of the material and corresponds to its ability to absorb a photon. ε is further related to the absorption cross section σ which represents the probability that a single molecule of the material absorbs a photon:

$$\sigma = \frac{2.303\,\varepsilon}{N_A} \tag{1-2}$$

where N_A is the Avogadro constant.

1-3-3. Emission quantum yield and lifetime

As mentioned above, radiative transition and nonradiative transition (IC and ISC) are competing processes. The probabilities of the radiative and nonradiative transitions are represented by radiative rate constant (k_r) and nonradiative rate constant (k_{nr}). These are important parameters to evaluate the emission property of a molecule. k_r and k_{nr} can be experimentally determined by measuring emission quantum yield Φ and lifetime τ. Emission quantum yield Φ and lifetime τ are described by k_r and k_{nr} as:

$$\Phi = \frac{k_r}{k_r + k_{nr}} \tag{1-3}$$

$$\tau = \frac{1}{k_r + k_{nr}} \qquad\qquad (1\text{-}4)$$

Φ is the ratio of the number of emitted photons to the number of absorbed photons. τ is the mean time that a molecule stays in the excited state. k_r is obtained as Φ/τ. Then, k_{nr} can be determined from $(1-\tau k_r)/\tau$.

1-4. Single molecule spectroscopy (SMS)

1-4-1. Basic principles of SMS [100]

Single molecule spectroscopy (SMS) is a technique to detect the fluorescence from single light-emitting entities, such as organic molecules, aggregates, nanoparticles or inorganic quantum dots, using fluorescence microscopy. The typical microscope configuration is shown in Fig. 1-12. Excitation light is mostly provided by a laser and excitation wavelength is selected to be absorbed by the sample. Excitation light is reflected by a dichroic mirror and focused on the sample through an objective lens. Fluorescence from the sample is passing through the dichroic mirror and a long pass filter and is detected by a photodetector. Dichroic mirror can reflect the excitation light (shorter wavelength) and pass the emission (longer wavelength). Long pass filter is used for cutting the reflected excitation light to decrease background scattering. It is well known that Rayleigh scattering intensity is proportional to excitation intensity and to the fourth power of wavelength. Shorter wavelength and higher intensity of excitation increase the background scattering and contribute to the difficulty of single molecule experiments. Therefore, optical filters, excitation wavelength and intensity should be selected and adjusted carefully.
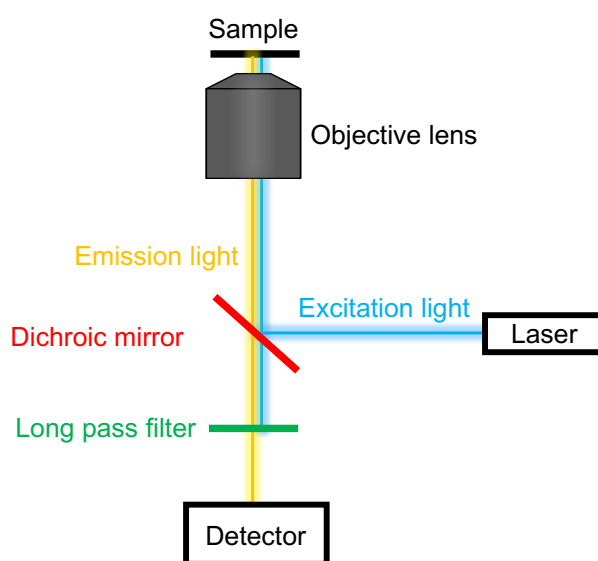
Fig. 1-12 Microscopic configuration

To measure fluorescence from a single molecule, there are two requirements: (1) make sure that fluorescence comes from only one molecule, (2) provide a signal-to-noise ratio (SNR) which is more than unity. In order to achieve the requirement (1), ultralow concentration of the sample is required. Generally, the concentration of sample for SMS is on the order of $10^{-9} \sim 10^{-10}$ mol/L. High contamination of the sample with impurities which can come from air, solvent, matrices or the chromophore sample itself can prevent single molecule measurements because it can cause scattering of the excitation light and sometimes the contaminants themselves show emission. Therefore, samples should be prepared from ultrapure reagents. Proper substrates such as glass or quartz are used depending on the excitation wavelength and have to be thoroughly cleaned by sonication with organic solvents and bases.

With respect to the requirement (2), several parameters should be considered such as excitation condition and photophysical properties of the chromophore. Baché *et al.* have proposed the following equation which shows a relationship between SNR and several parameters [101]:

$$\text{SNR} = \frac{D\emptyset_{\text{F}} \left(\frac{\sigma_p}{A}\right)\left(\frac{P_0}{h\nu}\right)}{\sqrt{\left(\frac{D\emptyset_{\text{F}}\sigma_p P_0 T}{Ah\nu}\right) + C_b P_0 T + N_d T}} \qquad (1\text{-}5)$$

where $\emptyset_{\text{F}}$ is the fluorescence quantum yield of the sample, σ_p is the absorption cross section, T is the detector counting interval (integration time or exposure time), A is the excitation light beam area, P_0 is the excitation power ($P_0/h\nu$ represents the number of incident photons per second), C_b is the background count rate per watt of excitation power and N_d is the dark count rate. D is the overall efficiency for detection of emitted photons which depends on instruments. According to equation (1-5), the higher $\emptyset_{\text{F}}$, σ_p, the more SNR increases. PDI, perylene and rhodamine are examples of organic molecules which have been used for SMS. They have high $\emptyset_{\text{F}}$ of more than 0.3 and ε on the order of 10^4 L mol^{-1} cm^{-1}. These values can be indicators of whether the molecule can be measured by

single molecule spectroscopy. The other important factors are excitation conditions such as P_0 and A. SNR proportionally increases with decreasing excitation area A. A can be controlled by the excitation mode. In confocal microscopy, only molecules in very small area (~ few hundreds of nm) are excited. On the other hand, A of wide-field microscopy is on the μm scale. From the eq. (1-5) it follows that SNR should improve as P_0 increases. However, this is not true in some situations. If P_0 is too high, the number of incident photons will be too large, and a photon will reach the molecule before it returns to the ground state. Therefore, the molecule cannot absorb the incident photon which means that the effective absorption cross section σ_p is reduced. This is the phenomenon of "optical saturation". The saturation intensity I_S and the reduced absorption cross section σ' are expressed in the following equations:

$$I_S = \frac{hv}{2\sigma\tau} \tag{1-6}$$

$$\sigma' = \frac{\sigma}{\left(1 + \dfrac{I}{I_S}\right)} \tag{1-7}$$

A calculated surface plot of fluorescence SNR vs. probing laser power and focal spot area for RG6 dye is shown in Fig. 1-13. Several parameters are experimentally determined. The plot shows that at first, SNR improves with increasing excitation power for the same value of A. When the excitation power increases up to near I_S, SNR starts decreasing due to optical saturation. In order to obtain good SNR, excitation conditions such as P_0 and A should be optimized according to photophysical properties of molecule of interest.
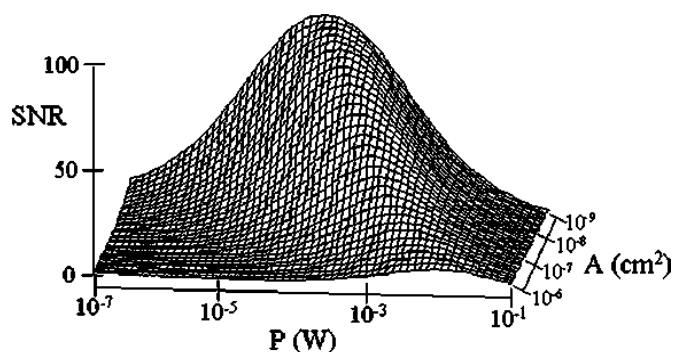
Fig. 1-13 Calculated surface plot of fluorescence SNR vs probing laser power and focal spot area [101]

1-4-2. Study of emission properties of single conjugated polymers

Generally, photophysical properties are measured in concentrated samples. Thin-film samples of the emissive conjugated polymers (called neat films) are usually prepared by spin coating from ~ 2 wt % solution. Alternately, conjugated polymer chains can be dispersed in a film of an optically inert polymer. These ensemble (bulk) samples produce results in which the values of physical observables are averaged over a large number of molecules. On the other hand, SMS can reveal the essential physical properties otherwise hidden by such ensemble averaging. As an example, fluorescence spectra of poly[2-methoxy-5-(2'-ethyl-hexyloxy)-p-phenylenevinylene] (MEH-PPV) on ensemble and single molecule level are shown in Fig. 1-14 [102]. MEH-PPV in polycarbonate shows broader fluorescence spectrum than that in toluene solution (Fig. 1-14A). Fig.1-14B is an example of two typical single molecule spectra of MEH-PPV peaked at 560 nm and 580 nm. They are narrower than the ensemble in polycarbonate and have almost the same width as in toluene solution. Some single polymer chains showed mixed spectrum composed of the 560 nm and 580 nm peaks, as shown in Fig. 1-14C. Fig.1-15 is a histogram of fluorescence peak wavelengths of single MEH-PPV and exhibits double peaked distribution with maxima at 560 nm and 580 nm. The two different fluorescence peaks are considered to come from different conformations of the polymer chain.

Conformation of single conjugated polymer can be determined by measuring polarization dependence. Single polymer chain has multiple light emitting sites because the conjugation length is limited. Absorption of each light emitting site depend on the polarization of excitation light. Therefore, chain conformation significantly affects the polarization dependence of absorption. To determine a single chain conformation, Monte Carlo simulation can be performed to obtain candidates of possible conformations and the corresponding absorption polarization anisotropy. The simulated results are then compared with experimentally measured anisotropy. The determined conformations of single MEH-PPV chains which show fluorescence peaks at 560 nm and 580 nm were found to be defect coil structure and defect cylinder structure, respectively (the inset of Fig.1-15). Defect coil has more extended structure than defect cylinder and less intrachain interactions. Collapsed defect cylinder conformation enhances intrachain interactions, causing increased intrachain energy transfer and inducing red shift of fluorescence. This conclusion is further supported by measurements of single conjugated polymers at low temperature. Theoretically, energy transfer efficiency depends on the spectral overlap between donor emission and acceptor absorption. Because the spectral shape becomes narrower as the temperature decreases, the spectral overlap decreases as well and energy transfer efficiency depends on the temperature. F. Schindler et al. measured fluorescence spectrum of a single oligomer and polymer chain of methyl-substituted poly(para-phenylene) (MeLPPP) at low temperature [103-104]. Undecamer (11 rings) and short MeLPPP chain (~ 62 rings) showed single narrow fluorescence peak at different wavelengths (Fig. 1-16a, b). On the other hand, long MeLPPP chain (~ 165 rings) showed 5 distinct fluorescence peaks (Fig. 1-16c). Some peaks are located at shorter wavelengths than the short MeLPPP. This indicates that the polymer chain has multiple light emitting sites and emission originates from the lowest energy site due to intrachain energy transfer at room temperature.

When chromophores are continuously excited by light irradiation or charge injection, they keep emitting photons but the intensity gradually goes down. In fact, at the single molecule level most chromophores do not show continuous emission. Fluorescence intensity is randomly changing between 'bright' and 'dark' states. This behavior, called

"blinking", is considered to occur due to intersystem crossing to a triplet state or due to transition to a long-lived radical ion dark state [105-107]. Conjugated polymers are not expected to show blinking because they contain multiple light emitting sites as mentioned above. Surprisingly, blinking was observed in single conjugated polymers when they were measured for the first time [108]. Several groups have made efforts to reveal the causes of polymer blinking, finding that conformation and intrachain energy transfer are important factors [109]. If a polymer chain takes compact conformation, excitation energy transfers to the light-emitting site with the lowest energy. Therefore, fluorescence comes from one or a small number of light-emitting sites. When such light-emitting site forms a triplet state or a radical ion state it will cause blinking. Such dark states on the lowest-energy light-emitting site can quench the remaining light-emitting sites so the polymer chain shows blinking in a similar way as a small molecule (Fig. 1-17, left panel). On the other hand, when polymer chain takes extended conformation, it does not show blinking because inefficient intrachain energy transfer allows emission from multiple light emitting sites simultaneously (Fig. 1-17, right panel).

Recently, SMS of conjugated polymers was performed in organic solvents using a special sample chamber (Fig.1-18), and the conformation was manipulated by switching the solvent quality during the measurement [110]. By switching the solvent from dimethyl sulfoxide (DMSO) as a poor solvent to *o*-dichlorobenzene (*o*-DCB) as a good solvent, fluorescence intensity drastically increased (Fig. 1-19). This result indicates that conformation can respond to solvent switching, leading to significant changes in fluorescence properties.
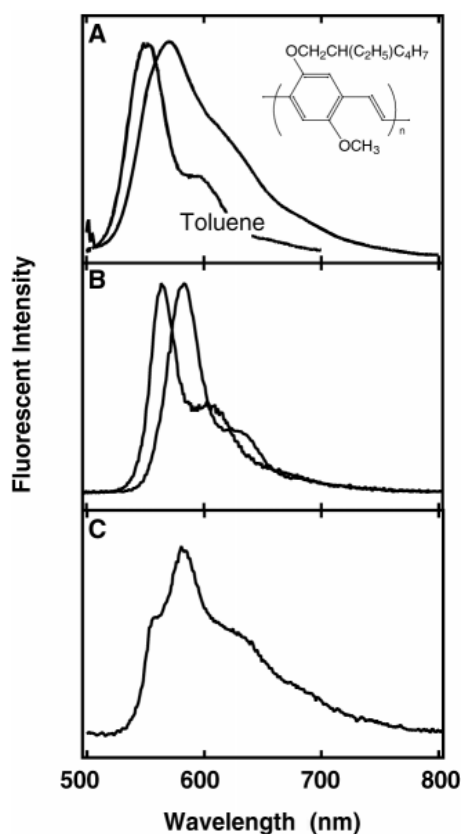
Fig. 1-14 (A)Fluorescent spectrum of ensemble MEH-PPV in toluene solution (left peak) and in a polycarbonate matrix at room temperature (right peak). (B) Typical fluorescence spectra of single MEH-PPV. (C) A fluorescence spectrum of MEH-PPV that show mixed feature of both a 560 nm peak and a 580 nm peak. [102]

Fig. 1-15 Histogram of fluorescence peak wavelength of single MEH-PPV [102]

25

Fig. 1-16 Fluorescence spectra of MeLPPP at low temperature, (a) undecamer, (b) short chain, (c) long chain [104]

Fig. 1-17 Blinking behavior of conjugated polymer with different conformations [109]

with lower solubility (~0.7 mg/ml) (*58*). Thus, the low–persistence length values suggest that any potential length effect might be overridden by the intrinsic flexibility of the chain when it is forced to collapse by its interaction with a poor solvent. Moreover, the low contribution of class II category observed in both solvents and for both polymer lengths investigated agrees with the interpretation of this material as a very flexible polymer that very rarely adopts exclusively rod-like structures.

Finally, it is important to note that there was a low but nonzero percentage of traces exhibiting class II behavior in *o*-DCB, which would not be expected when the chain is allowed to interact with a good solvent. We reason that this is due to chains containing a very small number of chromophores. Although most of the single chains we study can contain multiple chromophores, the shorter chains may have conjugation lengths that allow only one or two chromophores. This smaller number of chromophores in shorter chains can explain the higher fraction of classes II and III traces for sample **TES-P3HT-S** in *o*-DCB when compared to the same experiment for **TES-P3HT-L**. Conjugation lengths of dimensions similar to those of the whole chains that contain them have been estimated in previous bulk-dilution studies of P3HT (*50*). Furthermore, it has been previously shown that conjugation in single chains may not be broken even in partially bent conformations (*39*), which would be in agreement with this interpretation.

Real-time conformational switching of single-end–anchored P3HT chains

Single-end anchoring of single chains enables a new type of experiment in which different conformations of single chains can be actively induced while simultaneously measuring its PL output, simply by performing an exchange of solvents in real time. Because the polymer is anchored on the glass surface only at one end, it can reorganize its conformation in response to abrupt changes in solvation conditions. This rapid solvent-

Fig. 1-18 (A) Illustration of sample chamber for SMS in organic solvent, a conjugated polymer, different conformations of single chains, [110] intensity trace of single P3HT during real-time solvent switching [110]

1-5. Outline of the thesis

Many previous studies have already indicated that fluorescence properties of conjugated polymers significantly depend on the chain conformation and interchain interactions. However, understanding of the relationship between them is still far from complete because it is difficult to distinguish the effects of conformation from the intra- and interchain interactions. Polyfluorene can attain several types of conformation and show unique fluorescence properties. Therefore, polyfluorene is one of the best candidate materials to study the effects of polymer chain structure on fluorescence properties. Further, single-molecule spectroscopy is a powerful tool to investigate intrinsic nanoscale properties of emitting materials. Therefore, the purpose of this study is to use single-molecule spectroscopy to get more insight into how conformations and interchain interactions affect the fluorescence properties of polyfluorene, and conjugated polymers in general.

In chapter II, the appearance of the green emission band (g-band) in the spectra of blue-emitting polyfluorene is investigated on single chain level. Aggregate formation (both intrachain and interchain), as well as oxidation of polyfluorene have been proposed as the potential causes of the g-band. Numerous studies reported so far support alternatively one of the hypotheses and the true origin of the g-band is still subject of intense debate. In this chapter, in order to study how aggregate formation and oxidation affect the appearance and properties of the g-band, we measured fluorescence photophysical properties of single polyfluorene chains dispersed in several kinds of environment, including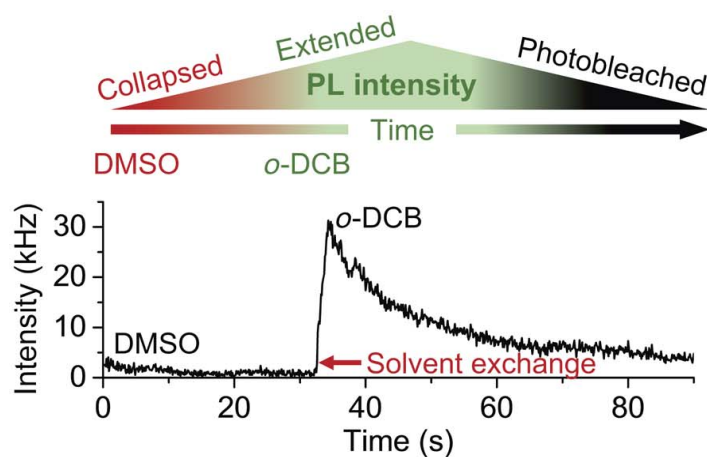 good- and poor-solvent inert polymer films and solutions. Although single polyfluorene chains preferentially showed the g-band in the poor-solvent rather than in the good-solvent solid matrices, only very small fraction of single chains showed the g-band in solution in ambient air. These results indicate that aggregate formation has a far greater effect on the appearance of the g-band than oxidation of the polyfluorene chains. In addition to single molecule study, lifetime and fluorescence quantum yield measurement were performed in bulk samples. The obtained small oscillator strength and two long-lifetime components of the g-band indicate that H-

aggregates and charge-transfer-like aggregates are responsible for the origin of the g-band.

In chapter III, to get further insight into the effects of conformation-related aggregation on fluorescence of polyfluorene, we combined a fluorescence microscope and an atomic force microscope (AFM) to mechanically manipulate the photophysical properties of polyfluorene nanoparticles (PFONPs). External force applied to a nanoparticle using the AFM tip causes the polymer chain to get packed more densely and induces strong interchain interaction. The resulting changes in fluorescence properties are monitored simultaneously with the applied force by measuring fluorescence intensity and spectra from the same nanoparticle using the fluorescence microscope. Absorption and PL spectra of PFONPs in water showed that both the glass- and β-phases coexist in the nanoparticles. Applying force of 1 μN induces a decrease of PL intensity without any spectral change, indicating that the force-enhanced interchain interaction promotes energy transfer as well as formation of quenching sites. When the force increased up to 5μN, the PL spectra changed from β-phase type emission to glass-phase type emission, and the overall PL intensity recovered to its initial value. These results indicate that excess force changed the ordered β-phase conformation to amorphous glass-phase, leading to increase the number of light emitting segment and causing an increase in PL intensity. This study showed that manipulation of conformation and interchain interactions in condensed state conjugated polymers is a great way to get insight into the role of each conformation and the corresponding interchain interaction.

In chapter IV, this concept is further extended and developed into mechanical manipulation of photophysical properties on true single-chain level. For that purpose, amino-terminated polyfluorene was synthesized and single chains were dispersed and chemically attached to a functionalized substrate by one end. The opposite end amino group reacts with a functionalized AFM tip which is used to mechanically stretch the single PFO chain. By simultaneously measuring fluorescence properties and force spectra, we investigated the conformation-photophysics relationship on single polyfluorene chains. Under photoirradiation, force curve of PFO chain in toluene showed a typical main peak related to the stretching of the main chain, and in addition one or several small peaks which were not observed without the excitation light. Such small force peaks were

attributed to excitonic coupling between PFO segments. From the force curves of such small peaks, excitonic coupling energy (J_{ex}) was estimated as 0.82 eV. This value was compared to theoretically obtained J_c and was found to be of the same order, indicating that exciton coupling energy between PFO segments was directly measured using the nanofishing technique. In addition, this result support the conclusion of Chapter II that intrachain interactions lead to formation of H-aggregates in PFO single chain. This result also shows the potential of nanofishing experiment to directly measure excitonic coupling energy in other conjugated systems. Simultaneously measured time change of fluorescence spectrum and the related force curve were also obtained, and though the data are lmited we have not observed correlation of excitonic force peak with the spectral change.

1-6. Reference

1. H. Mette, H. Pick, *Z. Phys.*, **1953**, *134*, 566.

2. M. Pope, H. P. Kallmann, P. Magnante, *J. Chem. Phys.*, **1963**, *38*, 2042-2043.

3. R.G. Kepler, *Phys. Rev.*, **1960**, *119*, 1226–1229.

4. H. Shirakawa, E. J. Louis, A. G. MacDiarmid, C. K. Chiang, A. J. Heeger, *J. Chem. Soc. Chem. Commun.*, **1977**, 578-580.

5. T. Ito, H. Shirakawa, S. Ikeda, *J. Polym. Sci. Pol. Chem.*, **1974**, *12*, 11-20.

6. C. K. Chiang, C. R. Fischer, Y. W. Park, A. J. Heeger, H. Shirakawa, E. J. Louis, S. C. Gau, A. G. MacDiarmid, *Phys. Rev. Lett.*, **1977**, *39*, 1098-1101.

7. C. K. Chiang, M. A. Druy, S. C. Gau, A. J. Heeger, E. J. Louis, A. G. MacDiarmid, Y. W. Park, H. Shirakawa, *J. Am. Chem. Soc.*, **1978**, *100*, 1013-1015.

8. H. Shirakawa, *Angew. Chem. Int. Ed.*, **2001**, *40*, 2574-2580.

9. A. G. MacDiarmid, *Angew. Chem. Int. Ed.*, **2001**, *40*, 2581-2590.

10. A. J. Heeger, Angew. Chem. Int. Ed., 2001, 40, 2591-2611.

11. C. W. Tang, S. A. VanSlyke, C. H. Chen, *J. Appl. Phys.*, **1989**. *65*, 3610-3616.

12. A. Tsumura, H. Koezuka, and T. Ando, *Appl. Phys. Lett.*, **1986**, *49*, 1210-1212.

13. H. Koezuka, A. Tsumura, and T. Ando, *Synth. Met.*, **1987**, *18*, 699-704.

14. C. W. Tang, *Appl. Phys. Lett.*, **1986**, *48*, 183-186.

15. https://www.industryresearch.biz/global-oled-display-materials-market-15083494, May, 2020.

16. S. Schols "Device Architecture and Materials for Organic Light Emitting Devices", 1st edition. Springer, Berlin, 2011.

17. https://cnx.org/contents/havxkyvS@12.2:Vd4OhCxi@7/Multiple-Bonds?minimal=true, May, 2020.

18. https://chem.libretexts.org/Bookshelves/Organic_Chemistry/Map%3A_Organic_Chemistry_(Wade)/02%3A_Structure_and_Properties_of_Organic_Molecules/2.02%3A_Molecular_Orbitals, May, 2020.

19. Z. G. Soos and G.W. Hayden, *Mol. Cryst. Liq. Cryst.*, **1988**, *160*, 421-432.

20. H. Meier, U. Stalmach and H. Kolshorn, *Acta polymer.*, **1997**, *48*, 379-384.

21. T. Izumi, S. Kobashi, K. Takimiya, Y. Aso and T. Otsubo, *J. Am. Chem. Soc.*, **2003**, *125*, 5286-5287.

22. M. Fukuda, K. Sawada and K. Yoshino, *Jpn. J. Appl. Phys.*, **1989**, *28*, L1433-L1435.

23. M. Fukuda, K. Sawada and K. Yoshino, *J. Polym. Sci. Part A: Polym. Chem.*, **1993**, *31*, L2465-L2471.

24. M. Knaapila, F. B. Dias, V. M. Garamus, L. Almásy, M. Torkkeli, K. Leppänen, F. Galbrecht, E. Preis, H. D. Burrows, U. Scherf and A. P. Monkman, *Macromocules*, **2007**, *40*, 9398-9405.

25. Q. Pei and Y. Yang, *J. Am. Chem. Soc.*, **1996**, *118*, 7416-7417.

26. B. Lin, L. Qiu, B. Qiu, Y. Peng and F. Yan, *Macromolecules*, **2011**, *44*, 9642-9649.

27. X. Zhu, Y. Xie, X. Li, X. Qiao, L. Wang and G. Tu, *J. Mater. Chem.*, **2012**, *22*, 15490-15494.

28. M. Suh, J. Bailey, S. W. Kim, K. Kim, D. J. Yun, Y. Jung, I. Hamilton, N. Chander, X. wang. D. D. C. Bradley, D. Y. Jeon and J. S. Kim, *ACS Appl. Mater. Interfaces*, **2015**, *7*, 26566-26571.

29. S. Setayesh, A. C. Grimsdale, T. Weil, V. Enkelmann, K. Müllen, F. Meghdadi, E. J. W. List and G. Leising, *J. Am. Chem. Soc.*, **2001**, *123*, 946-953.

30. L. Liu, S. Tang, M. Liu, Z. Xie, W. Zhang, P. Lu, M. Hanif and Y. Ma, *J. Phys. Chem. B*, **2006**, *110*, 13734-13740.

31. S. L. McFarlane, D. G. Piercey, L. S. Coumont, R. T. Tucker, M. D. Fleischauer, M. J. Brett and J. G. C. Veinot, *Macromolecules*, **2009**, *42*, 591-598.

32. L. Bai, B. Liu, Y. Han, M. Yu, J. Wang, X. Zhang, C. Ou, J. Lin, W. Zhu, L. Xie, C. Yin, J. Zhao, J. Wang, D. D. C. Bradley and W. Huang, *ACS Appl. Mater. Interfaces*, **2017**, *9*, 37856-37863.

33. M. N. Yu, H. Soleimaninejad, J. Y. Lin, Z. Y. Zuo, B. Liu, Y. F. Bo, L. B. Bai, Y. M. Han, T. A. Smith, M. Xu, X. P. Wu, D. E. Dunstan, R. D. Xia, L. H. Xie, D. D. C. Bradley and W. Huang, *J. Phys. Chem. Lett.*, **2018**, *9*, 364-372.

34. M. Leclerc, *J. Polym. Sci. Part A: Polym. Chem.*, **2001**, *39*, 2867-2873.

35. S. Günes, H. Neugebauer and N. S. Sariciftci, *Chem. Rev.*, **2007**, *107*, 1324-1338.

36. T. M. Clarke and J. R. Durrant, *Chem. Rev.* **2010**, *110*, 6736-6767.

37. W. L. Yu, J. Pei, W. Huang and A. J. Heeger, *Adv. Mater.*, **2000**, *12*, 828-831.

38. G. Klärner, M. H. Davey, W. D. Chen, J. C. Scott and R. D. Miller, *Adv. Mater.*, **1998**, *10*, 993-997.

39. X. Jiang, S. Liu, H. Ma and A. K. Y. Jen, *Appl. Phys. Lett.*, **2000**, *76*, 1813-1815.

40. S. Beauprè, M. Ranger and M. Leclerc, *Macromol. Rapid Commun.*, **2000**, *21*, 1013-1018.

41. M. T. Bernius, M. Inbasekaran, J. O'Brien and W. Wu, *Adv. Mater.*, **2000**, *12*, 1737-1750.

42. W. L. Yu, J. Pei, Y. Cao, W. Huang and A. J. Heeger, *Chem. Commun.*, **1999**, 1837-1838.

43. C. Ego, D. Marsitzky, S. Becker, J. Zhang, A. C. Grimsdale, K. Müllen, J. D. MacKenzie, C. Silva and R. H. Friend, *J. Am. Chem. Soc.*, **2003**, *125*, 437-443.

44. N. S. Cho, D. H. Hwang, B. J. Jung, E. Lim, J. Lee and H. K. Shim, *Macromolecules*, **2004**, *37*, 5265-5273.

45. B. Liu, W. L. Wu, Y. H. Lai and W. Huang, *Macromolecules*, **2002**, *35*, 4975-4982.

46. H. Zhou, L. Yang and W. You, *Macromolecules*, **2012**, *45*, 607-632.

47. H. N. Cho, J. K. Kim, D. Y. Kim and C. Y. Kim, *Macromolecules*, **1999**, *32*, 1476-1481.

48. M. Redecker, D. D. C. Bradley, M. Inbasekaran, W. W. Wu and E. P. Woo, *Adv. Mater.*, **1999**, *11*, 241-246.

49. S. H. Lee, D. Khim, Y. Xu, J. Kim, W. T. Park, D. Y. Kim and Y. Y. Noh, *Sci. Rep.*, **2015**, *5*, 10407.

50. Y. Vaynzof, D. Kabra, L. L. Chua and R. H. Friend, *Appl. Phys. Lett.*, **2011**, *98*, 113306.

51. A. C. Morteani, A. S. Dhoot, J. S. Kim, C. Silva, N. C. Greenham, C. Murphy, E. Moons, S. Ciná, J. H. Burroughes and R. H. Friend, *Adv. Mater.*, **2003**, *15*, 1708-1712.

52. J. J. M. Halls, A. C. Arias, J. D. MacKenzie, W. Wu, M. Inbasekaran, E. P. Woo and R. H. Friend, *Adv. Mater.*, **2000**, *12*, 498-502.

53. N. Corcoran, A. C. Arias, J. S. Kim, J. D. MacKenzie and R. H. Friend, *Appl. Phys. Lett.*, **2003**, *82*, 299-301.

54. A. J. A. B. Seeley and R. H. Friend and J. S. Kim, *J. Appl. Phys.*, **2004**, *96*, 7643-7649.

55. J. S. Kim, P. K. H. Ho, C. E. Murphy and R. H. Friend, *Macromolecules*, **2004**, *37*, 2861-2871.

56. H. J. Snaith, A. C. Arias, A. C. Morteani, C. Silva and R. H. Friend, *Nano Lett.*, **2002**, *2*, 1353-1357.

57. A. C. Arias, N. Corcoran, M. Banach, R. H. Friend and J. D. MacKenzie, *Appl. Phys. Lett.*, **2002**, *80*, 1695-1697.

58. C. L. Donley, J. Zaumseil, J. W. Andreasen, M. M. Nielsen, H. Sirringhaus, R. H. Friend and J. S. Kim, *J. Am. Chem. Soc.*, **2005**, *127*, 12890-12899.

59. B. R. Lee, W. Lee, T. L. Nguyen, J. S. Park, J. S. Kim, J. Y. Kim, H. Y. Woo and M. H. Song, *ACS Appl. Mater. Interfaces*, **2013**, *5*, 5690-5695.

60. W. Tang, L. Ke, L. Tan, T, Lin, T. Kietzke and Z. K. Chen, *Macromolecules*, **2007**, *40*, 6164-6171.

61. B. Liu, W. L. Yu, Y. H. Lai and W. Huang, *Macromolecules*, **2000**, *33*, 8945-8952.

62. E. Lim, B. J. Jung and H. K. Shim, *Macromolecules*, **2003**, *36*, 4288-4293.

63. S. Beaupré and M. Leclerc, *Adv. Funct. Mater.*, **2002**, *12*, 192-196.

64. A. D. Bouillud, I. Lévesque, Y. Tao and M. D'Iorio, *Chem. Mater.*, **2000**, *12*, 1931-1936.

65. M. Ranger and M. Leclerc, *Can. J. Chem.*, **1998**, *76*, 1571-1577.

66. M. Grell, M. Redecker, K. S. Whitehead, D. D. C. Bradley, *Liquid Crystal*, **1999**, *26*, 1403-1407.

67. W. C. Tsoi and D. G. Lidzey, *J. Phys.: Condens. Matter.*, **2008**, *20*, 125213.

68. H. Azuma, K. Asada, T. Kobayashi and H. Naito, *Thin Solid Films*, **2006**, *509*, 182-184.

69. A. Perevedentsev, N. Chander, J. S. Kim and D. D. C. Bradley, *J. Polym. Sci. Part B: Polym. Phys.*, **2016**, *54*, 1995-2006.

70. M. Arif, C. Volz and S. Guha, *Phys. Rev. Lett.*, **2006**, *96*, 025503.

71. J. Morgado and A. Alcácer, *Appl. Phys. Lett.*, **2007**, *90*, 201110.

72. M. Misaki, M. Chikamatsu, Y. Yoshida, R. Azumi, N. Tanigaki, K. Yase, S.

Nagamatsu and Y. Ueda, *Appl. Phys. Lett.*, **2008**, *93*, 023304.

73. D. Kasama, R. Takata, H. Kajii and Y. Ohmori, *Thin Solid Films*, **2009**, *518*, 559-562.

74. J. Peet, E. Brocker, Y. Xu, G. C. Bazan, *Adv. Mater.*, **2008**, *20*, 1882-1885.

75. J. Liang, L. Yu, S. Zhao, L. Ying, F. Liu, W. Yang, J. Peng and Y. Cao, *Nanotechnology*, **2016**, *27*, 284001.

76. Q. Zhang, L. Chi, G. Hai, Y. Fang, X. Li, R. Xia, W. Huang and E. Gu, *Molecules*, **2017**, *22*, 315.

77. M. J. Winokur, J. Slinker and D. L. Huber, *Phys. Rev. B*, **2003**, *67*, 184106.

78. H. Yang, K. Qu, H. Li, H. Cheng and J. Zhang, *Macromol. Chem. Phys.*, **2016**, *217*, 1579-1585.

79. D. D. C. Bradley, M Grell, X. Long, H. Mellor and A. Grice, M. Inbasekaran, and E. P. Woo, *Proc. SPIE*, **1997**, *3145*, 254.

80. M. Grell, D. D. C. Bradley, X. Long, T. Chamberlain, M. Inbasekaran, E. P. Woo and M. Soliman, *Acta polym.*, **1998**, *49*, 439-444.

81. M. Grell, D. D. C. Bradley, G. Ungar, J. Hill and K. S. Whitehead, *Macromolecules*, **1999**, *32*, 5810-5817.

82. A. J. Cadby, P. A. Lane, H. Mellor, S. J. Martin, M. Grell, C. Giebeler, D. D. C. Bradley, M. Wohlgenannt, C. An and Z. V. Vardeny, *Phys. Rev. B*, **2000**, *62*, 15604.

83. F. B. Dias, J. Morgado, A. L. Maçanita, F. P. da Costa, H. D. Burrows and A. P. Monkman, *Macromolecules*, **2006**, *39*, 5854-5864.

84. M. E. Caruso and M. Anni, *Phys. Rev. B*, **2007**, *76*, 054207.

85. M. Knaapila and A. P. Monkman, *Adv. Mater.*, **2013**, *25*, 1090-1108.

86. L. Huang, X. Huang, G. Sun, C. Gu, D. Lu and Y. Ma, *J. Phys. Chem. C*, **2012**, *116*, 7993-7999.

87. L. Huang, T. Li, B. Liu, L. Zhang, Z. Bai, X. Li, X. Huang and D. Lu, *Soft matter*, **2015**, *11*, 2627-2638.

88. B. Liu, T. Li, H. Zhang, T. Ma, J. Ren, B. Liu, B. Liu, J. Lin, M. Yu, L. Xie and D. Lu, *J. Phys. Chem. C*, **2018**, *122*, 14814-14826.

89. T. Shiraki, S. Shindome, F. Toshimitsu, T. Fujigaya and N. Nakashima, *Polym. Chem.*, **2015**, *6*, 5103-5109.

90. T. Li, B. Liu, H. Zhang, J. Ren, Z. Bai, X. Li, T. Ma and D. Lu, *Polymer*, **2016**, 299-306.

91. M. Nagai, J. Liu, W. Huang, M. Kikuchi, S. Kawaguchi and L. Xie, *J. Phys. Chem. C*, **2020**, *124*, 6304-6310.

92. D. W. Bright, F. B. Dias, F. Galbrecht, U. Scherf and A. P. Monkman, *Adv. Funct. Mater.*, **2009**, *19*, 67-73.

93. D. W. Bright, F. Galbrecht, U. Scherf and A. P. Monkman, *Macromolecules*, **2010**, *43*, 7860-7863.

94. W. C. Tsoi, A. Charas, A. J. Cadby, G. Khalil, A. M. Adawi, A. Iraqi, B. Hunt, J. Morgado and D. G. Lidzey, *Adv. Funct. Mater.*, **2008**, *18*, 600-606.

95. P. Prins, F. C. Grozema, B. S. Nehls, T. Farrell, U. Scherf and L. D. A. Siebbeles, *Phys. Rev. B*, **2006**, *74*, 113203.

96. Z. Bai, Y. Liu, T. Li, X. Li, B. Liu. B. Liu and D. Lu, *J. Phys. Chem. C*, **2016**, *120*, 27820-27828.

97. H. J. Eggimann, F. L. Le Roux and L. M Herz, *J. Phys. Chem. Lett.*, **2019**, *10*, 1729-1736.

98. G. Zheng, W. L. Yu, S. J. Chua and W. Huang, *Macromolecules*, **2002**, *35*, 6907-6914.

99. B. Valeur, Molecular Fluorescence Principles and Applications, Ed.; Wiley: Weinheim, Germany, 2005.

100.   W. E. Moerner and D. P. Fromm, *Rev. Sci. Instrum.*, **2003**, *74*, 3597-3619.

101. T. Basché, W. P. Ambrose and W. E. Moerner, *J. Opt. Soc. Am. B*, **1992**, *9*, 829-836.

102. J. Yu, D. Hu and P. F. Barbara, *Science*, **2000**, *289*, 1327-1330.

103. F. Schindler, J. Jacob, A. C. Grimsdale, U. Scherf, K. Müllen, J. M. Lupton, J. Feldmann, *Angew. Chem. Int. Ed.*, **2005**, *44*, 1520-1525.

104. J. Lupton, *Adv. Mater.*, **2010**, *22*, 1689-1721.

105. J. P. Hoogenboom, J. hernando, E. van Dijk, N. F. van Hulst and M. F. Garía-Parajó, *ChemPhysChem*, **2007**, *8*, 823-833.

106. M. Haase, C. G. Hübner, F. Nolde, K. Müllen and T. Basché, *Phys. Chem. Chem. Phys.*, **2011**, *13*, 1776-1785.

107. M. Mitsui, A. Unno and S. Azechi, *J. Phys. Chem. C*, **2016**, *120*, 15070-15081.

108. D. A. Vanden Bout, W. T. Yip, D. Hu, D. K. Fu, T. M. Swager and P. F. Barbara, *Science*, **1997**, *277*, 1074-1077.

109. Y. Ebihara and M. Vacha, *J. Phys. Chem. B*, **2008**, *112*, 12575-12578.

110. F. T. Carmona, S. Fronk, G. C. Bazan, I. D. W. Samuel and J. C. Penedo, *Sci. Adv.* **2018**, *4*, No. eaao5786.

Chapter II

## Intrachain Aggregates as the Origin of Green Emission in Polyfluorene

2-1. Introduction

2-1-1. The studies of aggregates as the cause of the g-band

In the initial studies, the cause of the g-band was considered to be aggregate or excimer emission because as the concentration of fluorene increased, the intensity of the g-band increased [1-2]. Additionally, this hypothesis was supported by numerous results showed that the g-band could be suppressed by copolymerization with anthracene, by blending of PF with different polymers and by introducing functional groups with high glass transition temperature (T_g) or bulky functional side chains [3-6].

2-1-2. The studies of oxidation as the cause of the g-band

In the meantime, oxidation of PFs as the cause of the g-band has been also proposed and studied. When PFs films were annealed at 200 °C in air and vacuum, only the sample annealed in air showed the g-band (Fig. 2-1) [7]. Therefore, it was concluded that the cause of the g-band was oxidation of a fluorene unit and formation of a keto-defect.
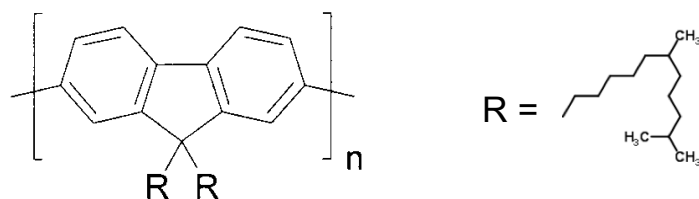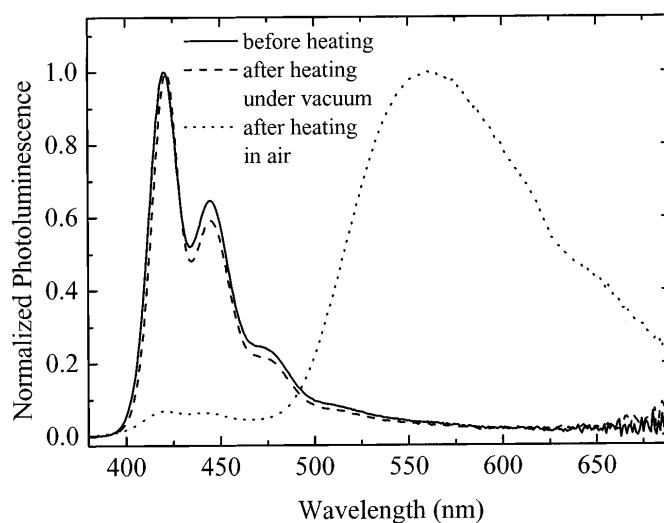
Poly(9.9-dialkylfluorene)

Fig. 2-1 Chemical structure of polyfluorene and photoluminescence spectra of polyfluorene neat film with and without annealing in air. [7]

In a copolymer of fluorene and fluorenone (species formed by oxidation of fluorene, Fig. 2-2) increasing fraction of the fluorenone caused direct increase of the intensity of the g-band [8-13]. This result directly supported the hypothesis of oxidation of fluorene monomers at the 9-position as the cause of the g-band. In addition, it was later found that the intensity of the g-band also increased by increasing the concentration of this copolymer in solution [12]. This observation indicated that a significant contribution to the g-band should originate from aggregates or excimers of fluorenone. Later, this hypothesis was disputed by a single molecule study which showed that the ratio of the blue-to-green emission intensity in individual polymer chains decreased when the fraction of fluorenone in the copolymer increased (Fig. 2-3) [13].
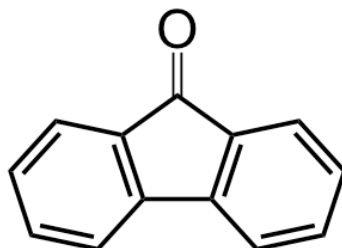
Fig. 2-2 Chemical structure of fluorenone
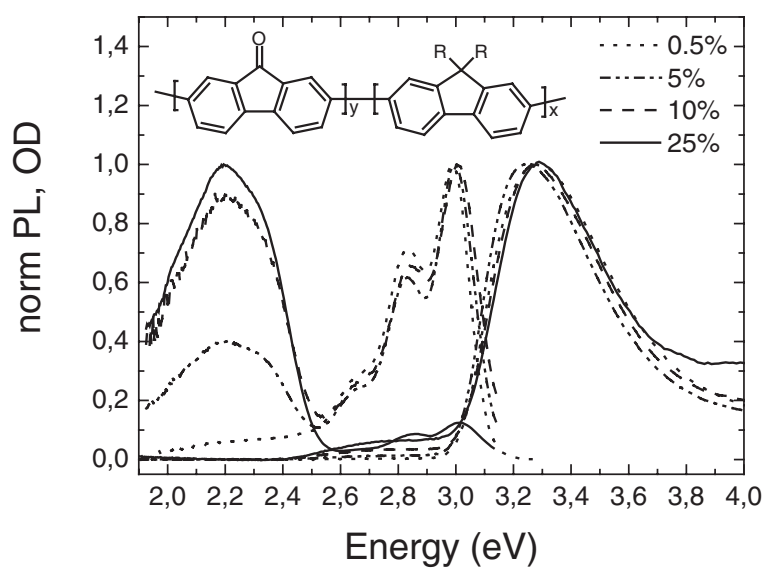
Fig. 2-3 Absorption and photoluminescence spectra of copolymer of fluorene and fluorenone with different ratio of fluorenone. [13]

2-1-3. Crosslinking of polyfluorene and g-band

The above results seem to undoubtably confirm the oxidation and fluorenone formation as the causes of the g-band. On the other hand, both soluble and insoluble parts were found in a PF film annealed at 200 °C in air, and it was shown that the intensity of the g-band in the insoluble part was stronger than that in the soluble part (Fig. 2-4) [14]. In IR spectra, the fluorenone C=O absorption of the insoluble part was weaker than that of the soluble part, whereas GPC showed that the insoluble part was formed by crosslinking between fluorenes. These facts point to an indirect relation between oxidation and the g-band.
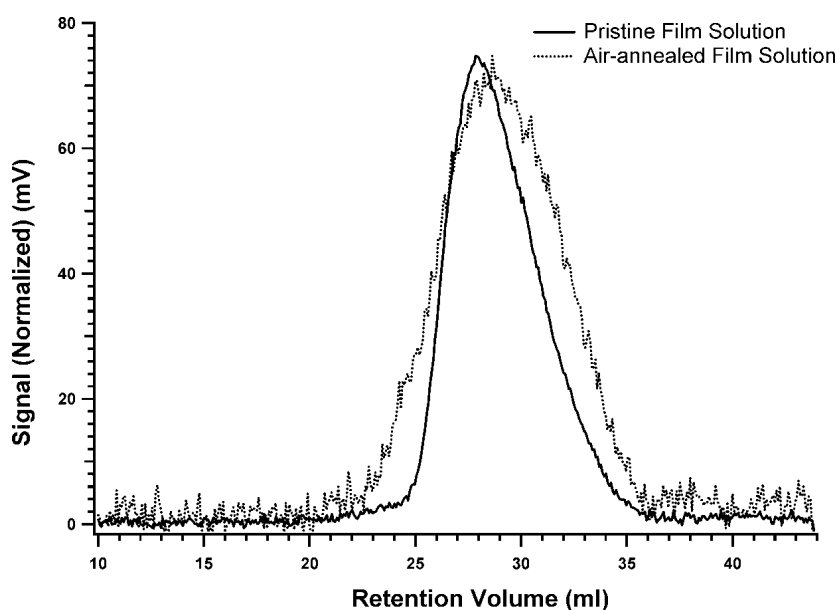
Fig. 2-4 GPC curve of soluble part of polyfluorene film with and without air-annealing. [14]

Later, fluorene trimers were degraded by UV irradiation in air and analyzed. Although oxidation was confirmed by IR spectra, MASS spectra showed that oxidized species other than fluorenone were mainly produced (Fig.2-5) [15]. Furthermore, results of measuring the relative amount of fluorenone and other oxidized species by IR spectra showed that there is no clear correlation between the amount of fluorenone and the intensity of the g-band [16]. All these results put the hypothesis of oxidation as the cause of the g-band into question. In related works, polyfluorenes with crosslinkable functional groups were synthesized and crosslinked by UV irradiation and thermal treatment, leading to the appearance of the g-band [17-20]. Therefore, crosslinking itself was suggested as an important factor for the existence of the g-band, although the mechanism responsible for its appearance during the crosslinking process has not been clarified.

Fig. 2-5 (a) Chemical structure of polyfluorene (PF8) and its monomers (F-Br and F-B), (b) IR spectra of PF8, F-Br and F-B. [15]

2-1-4. Recent studies of the g-band

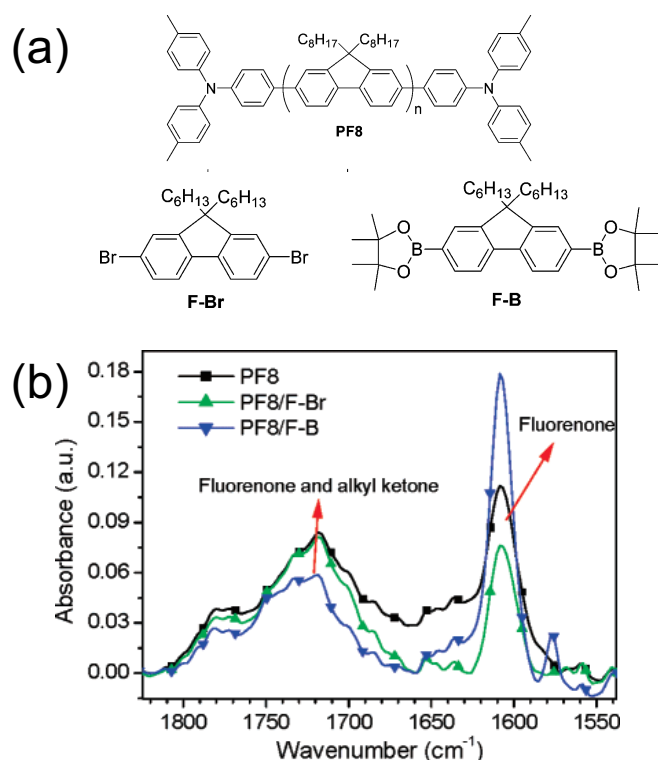Recently, several studies have continued contributing to the discussion of the g-band origin. Stability of the blue emission in PF was improved, e.g., by copolymerization with fluorinated phenylene units which caused an increase in the oxidation potential of the copolymer [21], by doping into wide-bandgap conducting [22] or inert matrices which were suggested to dilute trap states and the associated green emission [23], or by wrapping individual PF chains around single-walled carbon nanotubes [24]. Although suppression of the g-band emission in these studies was explained as a result of inhibited oxidation, most of the results could be equally well explained by suppressed formation of aggregates or excimers. Such mechanism was also confirmed by further exploring steric hindrance effects of bulky group sidechains [25-26].

2-1-5. Single molecule studies about the g-band

In most of the above studies, only averaged values of physical observables have been obtained in measurements of bulk polymeric samples. The technique of single molecule spectroscopy (SMS) has the advantage that it can measure fluorescence from individual molecules or polymer chains, and thus provide information on spatial and temporal heterogeneity with respect to different conditions and environments [27-32]. Besides that, it is possible to measure the dynamics of photophysical properties of single chains and deduce the character of excited states and optical transitions from the time-changing fluorescence spectra and intensity. PFs have been studied using the SMS technique before [33-36], and evidence was presented both for the presence [35] and absence [33] of the g-band as a result of oxidation. We have also previously carried out a PL and electroluminescence (EL) single-molecule study of a PF derivative, and found a variety of spectral shapes and presence of large and reversible spectral jumps that were inconsistent with the explanation of an oxidation-induced trap state [36].

2-1-6. Objective and strategies

All of the previous works mentioned above point to a conclusion that the origin of the g-band is still an open question, and that probably a few different mechanisms may be responsible to a different extent for its appearance. Motivated by this situation, we performed a single-molecule and ensemble study of the prototypical PF conjugated polymer, poly(9,9-di-n-octylfluorenyl-2,7-diyl) (PFO). As a strategy, we compare the fluorescence properties of single PFO chains in different environments. Polystyrene (PS) and poly(methyl methacrylate) (PMMA) are used as good and poor solvent matrices for PFO, respectively, to distinguish the effect of aggregation. PS film and an 8 wt% PS toluene solution are used to simulate environments with different oxygen permeability and diffusions. To directly compare the same PF chains in different environments, we measure single PF chains adsorbed on a substrate and immersed in poor solvent of hexane, then dried and re-immersed in good solvent of toluene. The conformational states of the toluene-prepared individual chains were checked by high-resolution atomic force microscopy (AFM). These single-molecule studies were subsequently complemented by ensemble measurements of bulk-concentration PF dispersed in PMMA films. Spectrally-resolved PL quantum efficiency, PL lifetimes and temperature-dependent absorption spectra provided the basic photophysical characteristics of the blue and green emission states. Together with the single-molecule results, the current study pointed to intra-chain H-type aggregates or charge-transfer states as the origin of the g-band emission under the conditions studied.

2-2. Experimental section

2-2-1. Materials

PFO used here was purchased from Aldrich (M_n 23566 g/mol, polydispersity index PDI 3.45). Polystyrene (PS, M_n 106751 g/mol, PDI 2.45) and poly(methyl methacrylate) (PMMA, M_n 100493 g/mol, PDI 1.72) used as matrices were purchased from Aldrich. All materials were used as received.

2-2-2. Sample preparation

Thin film for fluorescence microscopy measurements were prepared on quartz substrate by spin-coating at 3000 rpm for 30 s from 150 µL of 1 wt% matrix polymers solution in toluene containing PFO (at concentrations of 10^{-6} to 10^{-9} M and 10^{-12} M). Thin films of the concentration at $10^{-4} - 10^{-7}$ M were used for bulk samples and 10^{-10} M for single molecule experiment. The solution samples used for single molecule study were prepared by dropping 10µL PFO (10^{-11} M) in solution (of 8 wt% PS solution or toluene or cyclohexane) onto quartz substrate and then sandwiching with another substrate. Samples of PFO dispersed directly on substrate for single-chain fluorescence microscopy and AFM measurements were fabricated by spin-coating at 3000 rpm for 30 s from 150 µL of 10^{-9} M PFO toluene solution onto quartz or mica substrate. Thick solid films used for lifetime and quantum yield measurements were prepared by dropping 10 mL of 10 wt % PMMA in toluene solution containing PFO at different concentrations of 10^{-5} M – 10^{-7} M onto a Petri dish followed by drying for a week and peeling off, resulting in free-standing films with PFO concentrations of 10^{-4} and 10^{-6} M.

2-2-3. PL microscopy setup

Fluorescence from bulk thin films and the sample for single chains experiment was measured using an inverted microscope (IX 71, Olympus). The excitation was provided by a continuous wave laser (UV-FN-360, 100 mW, CNI) at 360 nm. Fluorescence from the sample was collected by an oil immersion objective lens (UplanFLN 100×, N.A. 1.3, Olympus). Reflected excitation light was cut by passing through a dichroic mirror (Dichro 375, Chroma) and a long-pass filter (LP 377, Edmund). The signal was detected by an electron-multiplying (EM) CCD camera (iXon, Andor Technology) with an exposure time of 30 ms. An imaging spectrograph (CLP- 50LD, Bunkou Keiki) was attached to CCD camera to measure fluorescence spectrum. For the measurement of bulk sample, the excitation power was $1-6$ W/cm^2 and EM gain was ranging between 0 and 1000. For the single-chain experiments, the excitation power was 6 W/cm^2 and EM gain was 1000.

2-2-4. Atomic force microscopy

Conformations of PFO single chains placed on mica substrate were directly measured using an AFM (Cypher, Asylum Research) in tapping mode. The cantilever was PPP-NCHAuD (Nanosensors).

2-2-5. Bulk sample characterization

PL quantum yield was measured using an absolute luminescence quantum yield measurement system (C9920-02G, Hamamatsu Photonics). PL lifetime was measured using a compact fluorescence spectrometer (Quantaurus-Tau C11367-24, Hamamatsu Photonics).

2-3. Results and Discussion

2-3-1. Fluorescence spectra of bulk PFO samples

Conformation and photophysical properties of light emitting polymers have been known to depend critically on the matrices in which they are dispersed [29, 34, 35]. In this study, we attempt to control the conformation of the polymer using appropriate matrices that differ in solubility and dielectric constants. We used PS as a good-solvent matrix and PMMA as a poor-solvent matrix and expect, accordingly, that the PFO chains would take more extended conformations in PS and more compact conformations in PMMA. To confirm this assumption, we measured fluorescence spectra of bulk PFO in PS and PMMA thin firms at different concentrations ranging from 10^{-4} to 10^{-7} M (Fig. 2-6). The fluorescence spectra show a dominant blue band, similar to the PL spectra in toluene solution (Fig. 2-15 shown in appendix). For the fluorescence spectra in PMMA (Fig. 2-6a), the intensity of the g-band between 500 and 600 nm of the 10^{-4} M concentration sample is stronger than that of the lower concentration samples. We further use the ratio of the intensity of green emission at 540 nm (approximately center of the g-band) and that of the blue emission peak I_{540nm} / I_{blue} as an indicator of the g-band intensity. The I_{blue} value is taken directly as the PL intensity maximum at the PL peak position, which itself slightly changes with concentration and therefore is not defined at a specific wavelength. The value of I_{540nm}/I_{blue} of PFO 10^{-4} M concentration in PMMA was 0.30. For concentrations lower than 10^{-5} M, the I_{540nm}/I_{blue} ratio drops to about 0.20 and does not depend on the concentration value. This result indicates the presence of both intra- and intermolecular interactions in the 10^{-4} M sample and only intramolecular interactions in the $10^{-5}-10^{-7}$ M samples. In PS, on the other hand, the I_{540nm}/I_{blue} ratio of the 10^{-4} M sample was 0.17 and that of the $10^{-5}-10^{-7}$ M samples was about 0.10. These overall smaller values of the I_{540nm}/I_{blue} ratio in PS indicate that PFO does take more extended conformations in PS that lead to a decrease in both types of interactions.
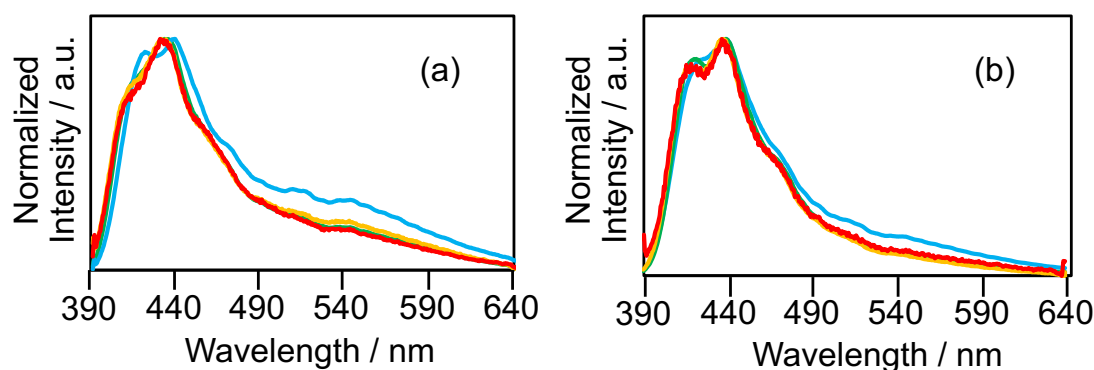
Fig. 2-6 PL spectra of PFO dispersed at different concentrations in solid thin-film polymer matrices of (a) PMMA and (b) PS. Excitation wavelength was 360 nm.

2-3-2. Fluorescence properties of single PFO chains in polymer films and in solutions

In this section, by comparing the photophysical properties of single PFO chains in good-solvent PS films to those in poor-solvent PMMA films, in solid PS to those in PS solution, and in poor solvent of hexane to those in good solvent of toluene, we examine the effect of aggregation as well as the effect of oxygen diffusion on the appearance of the g-band. To get insight on the conformation of single PFO chains in PS, we measured time change of PL intensity and the result is shown in Fig. 2-7a. The PL intensity is continuously decreasing due to photobleaching over the measurement interval of 50 s. It has been reported that the photobleaching and blinking behavior of single-conjugated polymer chains are dependent on the chain conformation [27, 40]. Polymer chain with extended conformation generally do not show blinking because the emission proceeds independently from multiple-conjugated segments, whereas chains with compact conformation typically undergo two- or multiple-state blinking because of efficient energy transfer to and emission from one or limited number of conjugated segments. The time trace in Figure 2-7a indicates that single PFO chains in PS take extended conformation, as expected for a good-solvent matrix. PL spectra of individual PFO chains show both blue and green emission spectral bands, as seen in Figure 2-7b. The spectra

were fitted with a sum of Gaussian functions, and a histogram of the 0−0 emission peak wavelengths is shown in Figure 2-7c. The single PFO chains emit mostly blue emission and the fraction of molecules exhibiting the g-band ($R_{g\text{-band}}$) was 0.27 (that is, 27% of PFO molecules showed the green emission). The distribution of the green emission peaks is broader than that of the blue emission. The blue emission bands are narrower with a vibronic structure (spectra 1 and 2 in Figure 2-7b) and are attributed to π-π* transitions [41]. We note that the spectral shapes of the blue-band spectra 1 and 2 in Figure 2-7b are different. Although the spectrum 2 resembles typical glassy state of PFO, the spectrum 1 indicates a minute contribution of a well-defined extended β-phase conformational state [42]. The green emission bands are generally broader and 38% of them (6 out of 16) also show a vibronic structure (spectrum 4 in Figure 2-7b). In the histogram in Figure 2-7c, the vibronic structure spectra are plotted in red color and are located around 500 nm, whereas the remaining structureless bands (such as spectrum 3 in Figure 2-7b) plotted in white color are more red-shifted and are located between 500 and 550 nm. The two different spectral types and spectral locations of the g-bands point to a possibility that more than one light-emitting species contribute to the emission in the area of the g-band. Finally, an example of time evolution of the emission spectra is shown in Figure 2d as a two-dimensional (2D) spectral plot. Of the 16 molecules that show green emission, 88% (14 molecules) undergo reversible and complete spectral changes between blue and green emission as shown in Fig. 2-7d. For the remaining two molecules, the spectral change is irreversible, i.e., although the spectrum shifted from blue to green, the reverse from green to blue has not happened during the measurement interval.
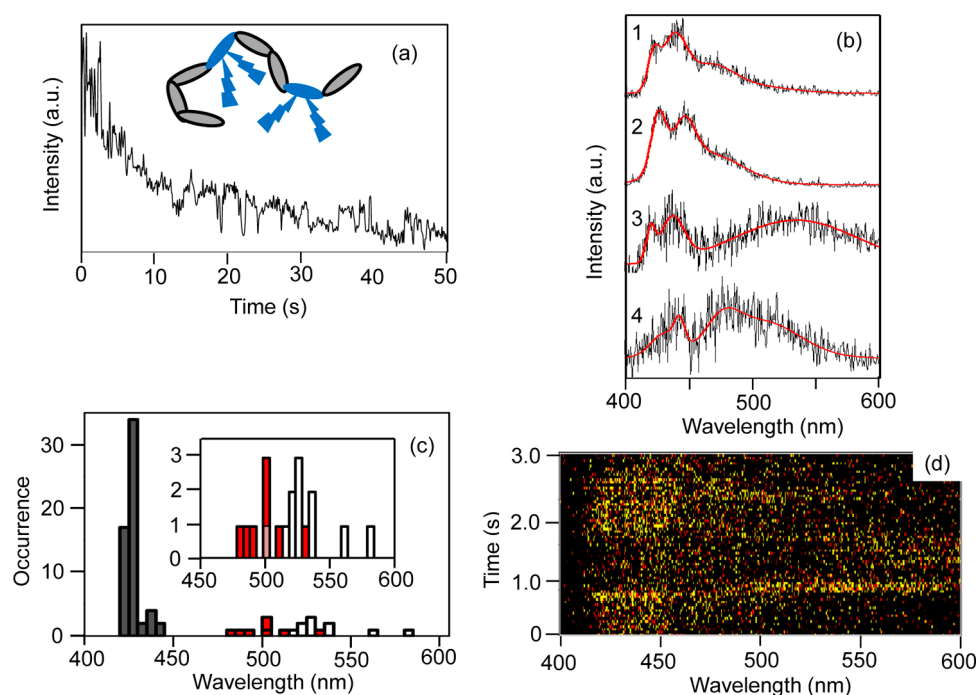
Fig. 2-7 PL properties of single PFO molecules in PS. (a) Time trace of PL intensity. (b) Representative PL spectra. (c) Histogram of $0-0$ peak wavelengths of PL spectra, separated into blue emission (gray bars), vibronic green emission (red bars), and structureless green emission (white bars); the inset shows detail of the g-band distribution. (d) Two-dimensional (2D) plot of a time change of a PL spectrum from one PFO chain.

In the poor-solvent matrix of PMMA, we can expect that PFO chains take more compact conformations. This is confirmed by measuring the PL intensity traces, which show blinking behavior, such as the one in Fig. 2-8a. The blinking is a result of efficient funneling of energy absorbed over the whole chain into one or a few conjugated segments, which function as energy emitters. This concept, introduced in the early works of the Barbara group [27], can explain the blinking as a reversible photochemical reaction occurring on these low-energy acceptors. The efficient funneling is a consequence of the compact chain conformation and the resulting close proximity of nearby conjugated segments. PL spectra of single PFO chains show again both blue and green emission bands, as seen in Fig. 2-8b. A histogram of $0-0$ emission peak wavelengths (Fig. 2-8c)

indicated that 58% of the PFO molecules showed the green emission band ($R_{\text{g-band}} = 0.58$), about twice a fraction compared to that in PS. This observation suggests that the appearance of the g-band is related to the chain conformation and possibly to intrachain aggregation. The blue emission bands (spectra 1 and 2 in Fig. 2-8b) have vibronic structure similar to that in PS, with the spectrum 1 indicating a presence of a small amount of β phase conformation [42]. Of the 35 molecules emitting in the green spectral rejoin, 43 % (15 molecules) show a vibronic structure (spectrum 3 in Fig. 2-8b). Similar to the PS matrix, most of these molecules are located around 500 nm (plotted in red in the histogram in Fig. 2-8c). The remaining molecules showing a structureless g-band (spectrum 4 in Fig. 2-8b) are spread between 500 and 600 nm. The results of time changes of PL spectra are similar to those in PS. Both stable blue emission and reversible green emission were observed. Of the 35 molecules showing the g-band, 80% (28 molecules) exhibit reversible blue−green−blue spectral changes, 11% (4 molecules) irreversible blue-green changes, and 9 % (3 molecules) show stable green emission.
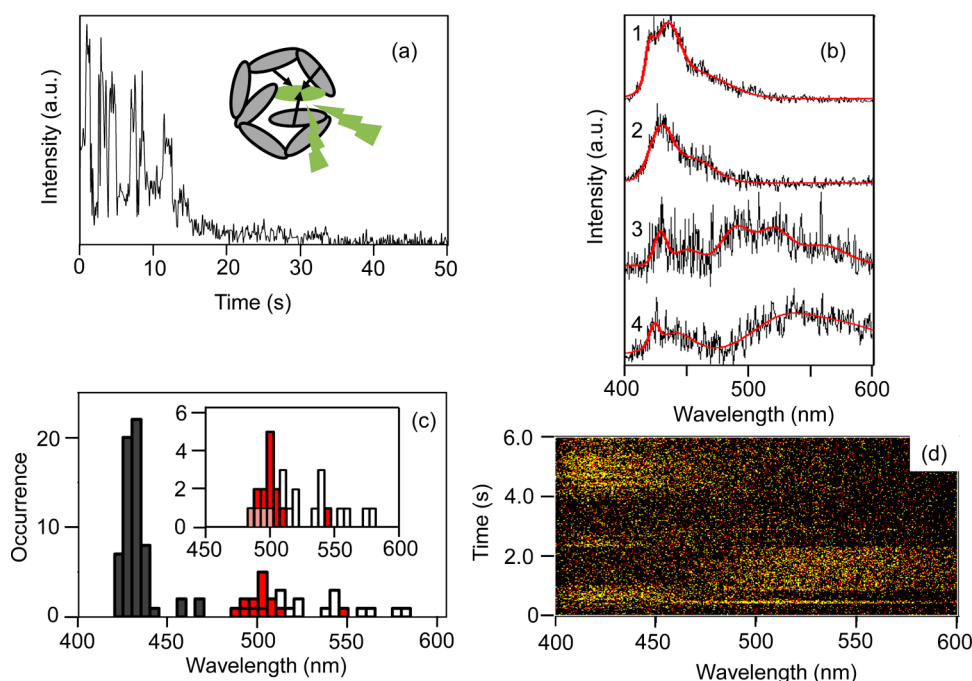
Fig. 2-8 PL properties of single PFO molecules in PMMA. (a) Time trace of PL intensity. (b) Representative PL spectra. (c) Histogram of 0−0 peak wavelengths of PL spectra, separated into blue emission (gray bars), vibronic green emission (red bars), and structureless green emission (white bars); the inset shows detail of the g-band distribution. (d) Two-dimensional (2D) plot of a time change of a PL spectrum from one PFO chain.

Because the good-solvent PS matrix provides environment for extended conformations resulting in lower fraction of g- band emission, it is also a suitable choice for the investigation of the effect of oxygen diffusion and of oxidation on the appearance of the g-band. For that purpose, we compare the above photophysical properties of PFO in solid PS film to those obtained in 8 wt % toluene solution of PS. All experiments are carried out under ambient conditions, under which the PS toluene solution is much more permeable to diffusing oxygen. In the solution, single PFO chains (immobilized by adsorption on the quartz surface) show both blue and green emission bands. However, the blue emission is prevalent as only 6% (three molecules, $R_{\text{g-band}} = 0.06$) of PFO are located in the green emission region (see histogram in Fig. 2-9a). Similar to the solid films, the

blue emission bands have vibronic structure (Fig. 2-9b, top and middle). All of the green emission is broad and structureless (Fig. 2-9b, bottom) and shows reversible spectral changes, as seen in the example in Fig. 2-9c. The insensitivity of the g-band to the increased presence of oxygen indicates that in this system photo-oxidation does not affect the g-band appearance and that conformational freedom of the PFO chains allowed by the good-solvent solution environment has a more prominent effect by further minimizing intra- molecular interactions and the possible aggregation effects.
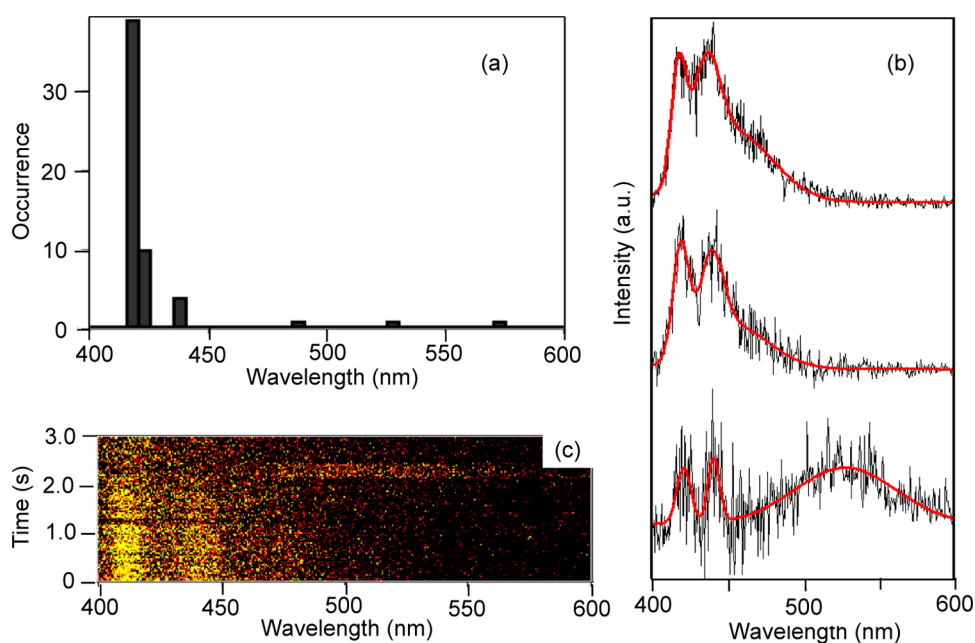

Fig. 2-9 PL properties of single PFO molecules adsorbed on quartz surface and immersed in 8 wt % toluene solution of PS. (a) Histogram of 0−0 peak wavelength of PL spectra. (b) Typical PL spectra of blue emission (top and middle) and of g-band (bottom). (c) Two-dimensional (2D) plot of a time change of a PL spectrum from one PFO chain.

As indicated by the above observations, conformation of isolated PFO chains is the dominant factor related to the appearance of the g-band. In the following, we attempted to directly observe photophysical changes caused by the change of conformation by measuring PL spectra of single PFO chains adsorbed on a quartz substrate. The same single chains were first immersed in cyclohexane (poor solvent for PFO), then dried, and reimmersed in toluene (good solvent). As for the solid matrices, we expect compact conformation in the poor solvent and extended conformation in the good solvent and examine the possible effect of the different conformations on the fraction $R_{\text{g-band}}$ of the green emission. The results are shown in Fig. 2-10. In cyclohexane, the blue emission has vibronic structure and the majority (96% or 22 molecules) of the green emission was in the form of structureless broad spectra (Fig. 2-10a, inset). In this solvent, $R_{\text{g-band}}$ was 0.44. In terms of time changes of PL spectra, 9% (2 molecules) of the g-band changes were reversible, 78% (21 molecules) were irreversible, and 13% (3 molecules) showed stable green emission. On the other hand, when the solvent was changed to toluene, $R_{\text{g-band}}$ dramatically decreased to 0.13, i.e., 87% of the single PFO chains showed stable blue vibrationally resolved emission (Fig. 2-10b, inset). Although we have not succeeded in real-time monitoring of the conformational changes on the same single chain, the above observations obtained on the same statistical ensemble of single PFO chains provide a strong support for the chain conformation and the related intrachain interactions as the main causes of the g-band.
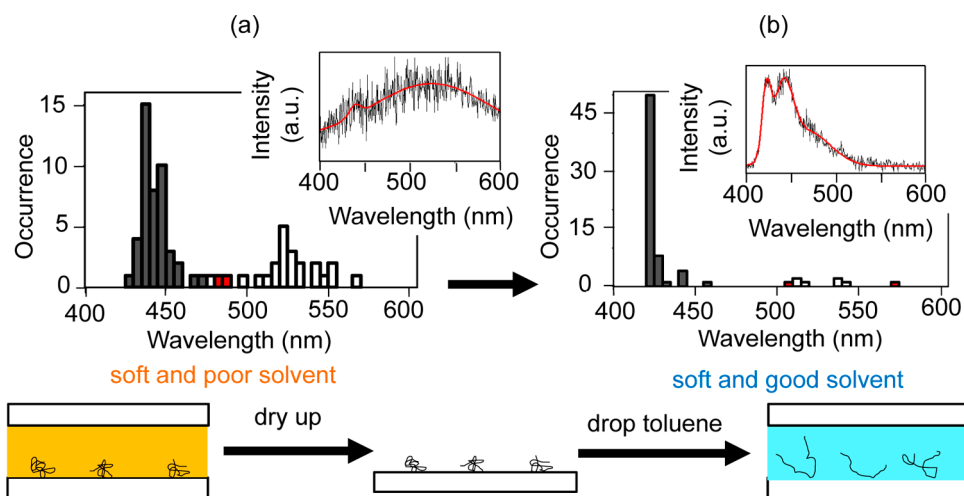
Fig. 2-10 PL properties of single PFO molecules adsorbed on quartz surface and immersed in cyclohexane (a) and toluene (b). (a) Histogram of 0− 0 peak wavelengths of PL spectra in cyclohexane, separated into blue emission (gray bars), vibronic green emission (red bars), and structureless green emission (white bars); inset: typical PL spectrum in cyclohexane. (b) Histogram of 0−0 peak wavelength of PL spectra in toluene, separated into blue emission (gray bars), vibronic green emission (red bars), and structureless green emission (white bars); inset: typical PL spectrum in toluene.

2-3-3. Conformation of PFO measured directly by atomic force microscopy

To confirm the expected extended conformation of single PFO chains in good-solvent toluene solution, high-resolution AFM measurements were performed. For that purpose, PFO was dispersed on a mica substrate by spin-coating from toluene solution. Additionally, we measured PL spectra of single PFO chains on quartz substrate, prepared by the same process of spin coating from toluene solution, to correlate the conformation and PL properties.

The PL spectra consist mainly of vibrationally resolved blue bands (Fig. 2-11a), similar to the PFO chains immersed in toluene. In a similar way, the histogram of 0−0 emission peak wavelengths resembles that of the PFO immersed in toluene, with the $R_{g\text{-band}}$ of 0.23. These observations confirm that the PFO photophysical properties do not differ dramatically between chains adsorbed on surface in toluene solution and chains spin-coated from toluene solution, with the latter process fixing the conformation by fast solvent evaporation. In the AFM images, we observed extended structures with well-resolved sections of the PF main chain (such as those shown in Fig. 2-11c,d) and occasionally compact particle-like structures (such as the one in Fig. 2-11b). Of the more than 20 structures measured, 6 could be unambiguously assigned to single PF chains based on their dimensions and of these 5 corresponded to the extended conformations. We used a simple estimation to confirm that chains corresponding to average molecular weight of the PFO used in these experiments would have fully extended length of approx. 50 nm. Taking into account the polydispersity index of the PFO used, the images in Fig. 2-11c,d conceivably reflect the conformations of single PFO chains and confirm the extended conformational forms prevalent in good solvent. These measurements also provide a direct correlation between the conformation and the PL spectral characteristics of the single PFO chains.
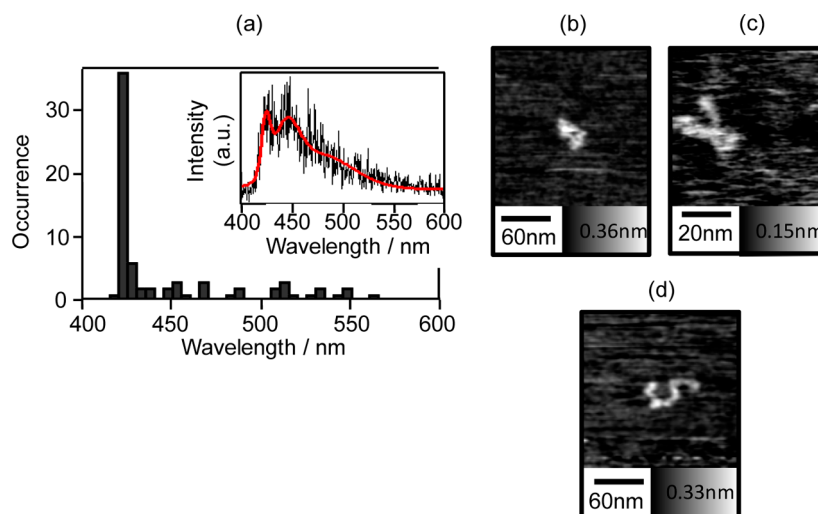
Fig. 2-11 (a) Histogram of 0−0 peak wavelength of PL spectra of PFO spin-coated from toluene on quartz substrate; inset: PL spectrum. (b−d) Typical AFM images of PFO single chains spin-coated from toluene on mica substrate.

2-3-4. Spectrally resolved radiative and nonradiative rate constants of PFO on ensemble level

The above experiments indicated that single-chain conformation and the resulting intramolecular interactions rather than the presence of oxygen play a dominant role in the formation of the g-band. The intrachain interactions result in formation of aggregates between different parts of the chain, which give rise to the red- shifted emission spectra. The possible aggregate states include excimers, J- or H-aggregates, or charge-transfer (CT) complexes, but it is unclear which of these contribute to the g-band emission. To get insight into the character of the aggregates, we measured spectrally resolved PL lifetime and PLQY and obtained oscillator strengths f for the blue and green region optical transitions.

Fig. 2-12a−c shows examples of PL decay curves of PFO dispersed in free-standing PMMA film at the concentration of 10^{-6} M detected at three different wavelengths, corresponding to blue emission band (420 nm), vibrationally resolved green emission (501 nm), and structureless green emission (555 nm). Overall, the decays were recorded

with the detection ranging from 390 to 650 nm with an interval of 3 nm. At each detection wavelength, the decays were fitted with a sum of exponential decay functions and three main components were identified as 0.34, 1.4, and 5.1 ns. Further, these lifetime components together with their weights were used to calculate the integrated intensity emitted at each wavelength within each lifetime component (see appendix and Fig. 2-16 for details). The spectral dependences of these integrated intensities are plotted for each component in Fig. 2-12d−f. The shortest lifetime component of 0.34 ns shows a sharp spectral peak located in the blue region, whereas the 1.4 and 5.1 ns components are broad and correspond to the g-band region. The spectrum of the 1.4 ns component is narrower and has a peak around 500 nm, whereas the spectrum of the 5.1 ns component is broad with two peaks at 520 and 575 nm. The integrated areas of the lifetime spectra of each component correspond to the number of emitted photons, and these are directly related to the PLQY of the three corresponding optical transitions. The ratio $S_{0.34ns}/ S_{1.4ns}/S_{5.1ns}$ of the integrated spectral areas of the three components was calculated as 39.7:1.5:1. The $S_{0.34ns}$ area is relatively much larger than the $S_{1.4ns}$ and $S_{5.1ns}$ areas, which implies that the PLQY of the blue component is also much larger than that of the g-band. We further measured an overall PLQY of the same PFO sample, excited at 360 nm. The resulting value of 0.31 was separated into three components using the above ratio (39.7:1.5:1) to obtain PLQY of each component $\Phi_{0.34ns}$, $\Phi_{1.4ns}$, and $\Phi_{5.1ns}$ as 0.29, 0.011, and 0.008, respectively. However, in addition to the possibility of direct population of the g-band emitting states by absorption, energy transfer from the blue band states also contributes to the g-band population, thus underestimating the PLQY of the green components. To obtain the corrected value of Φ'_{green}, we measured the PLQY excited in a region where the blue-emitting species do not absorb and the energy-transfer contribution can be neglected. For this purpose, absorption spectra of PFO dispersed at the concentrations of 10^{-4} and 10^{-6} M in free- standing PMMA film are shown in Fig. 2-13. For the higher concentration sample, a new absorption shoulder appears between 450 and 500 nm, corresponding to the absorption of the aggregates species. Using the excitation wavelength of 470 nm for lifetime measurement, we obtained two decay components of 1.6 and 5.5 ns, well corresponding to the above g-band values obtained under the 360 nm

excitation. Further, using the excitation wavelength of 465 nm to measure directly the PLQY of the green emission, we obtained the corrected value Φ'_{green} of 0.036. Using the ratio (39.7):1.5:1 obtained above, this value can be separated into corrected components $\Phi'_{1.4ns}$ and $\Phi'_{5.1ns}$ as 0.021 and 0.014, respectively. The PLQY values of Φ_{blue}, $\Phi'_{1.4ns}$, and $\Phi'_{5.1ns}$ together with the lifetimes are summarized in Table 2-1. The measured lifetime and PLQY values can be used to calculate radiative k_r and nonradiative k_{nr} rate constants, as shown in the appendix. Further, the radiative rate k_r is related to oscillator strength f of the optical transition (Appendix, eq 2-1, 2-2). The calculated values k_r, k_{nr}, and f of the individual transitions are also summarized in Table 2-1. The values of k_r and f of the two g-band components are 2 orders of magnitude smaller than those of the blue component. Of the possible candidates of aggregates mentioned above, the fact that the oscillator strength of the g-band transitions is much smaller than that of the blue emission excludes the possibility of J-aggregates, which are known for strongly allowed red-shifted transitions with large oscillator strength. Of the remaining, CT complexes have small overlap of highest occupied molecular orbital and lowest unoccupied molecular orbital, leading to small oscillator strength. In H-aggregates, the red-shifted transition is forbidden, resulting in small oscillator strength as well. In the following, we try to further narrow the possibilities by measuring the g-band emission at different excitation wavelengths.

Table 2-1. Photophysical Properties of Blue-Emitting Component and of g-Band, Obtained from PLQY and Lifetime Measurements on PFO Dispersed in PMMA Matrix at Ensemble Concentration

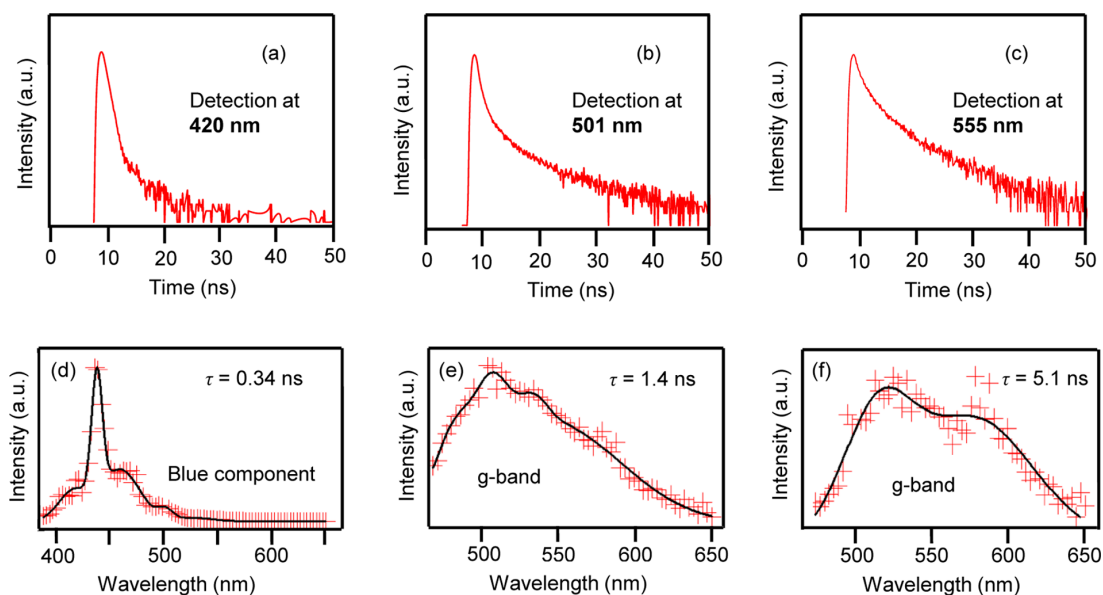|	PLQY	τ/ns	k_r/s^{-1}	k_{nr}/s^{-1}	f
blue component	0.29	0.34	8.4×10^8	2.1×10^9	1.28
g-band	0.022	1.4	1.5×10^7	6.7×10^8	0.024
	0.014	5.1	3.0×10^6	2.0×10^8	0.0056

Fig. 2-12 PL decay curves of PFO dispersed in PMMA at the concentration of PFO 10^{-6} M, with detection wavelength set to (a) 420 nm, (b) 501 nm, and (c) 555 nm. Spectrally resolved components of PL lifetime of PFO: (d) 0.34 ns, (e) 1.4 ns, and (f) 5.1 ns.
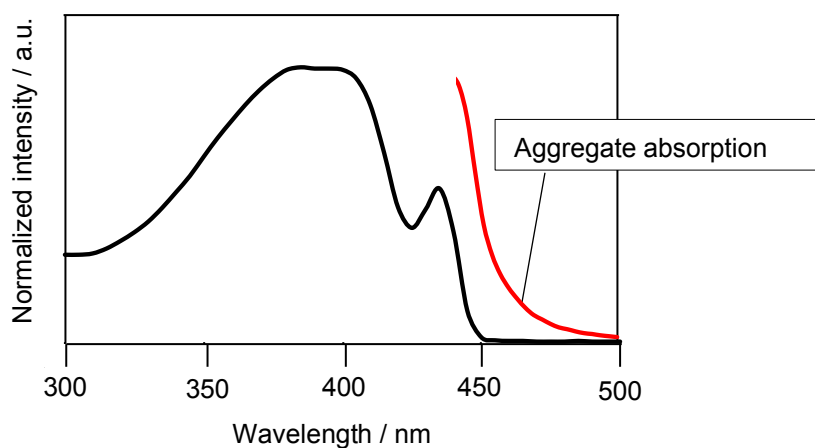

Fig. 2-13 Absorption spectra of PFO dispersed at the concentration of 10^{-4} M (red) and 10^{-6} M (black) in free-standing PMMA film

2-3-5. Excitation wavelength dependence of the g-band spectra

The difference between an excimer and a ground-state aggregate lies in the energy of their ground states. Excimers cannot be directly excited in the region of the ground- state aggregate absorption. If excimers contributed significantly to the g-band, a shift of the excitation wavelength from 360 to 476 nm (which is within the aggregate absorption shoulder, Fig. 2-13) would cause a large change of the g-band spectrum. We note that the spectrum in Fig. 2-13 also shows a new peak around 440 nm, which reflects the formation of the well-ordered β-phase [42]. However, because the two excitation wavelengths used here are outside of the β-phase absorption region, we assume that this phase would not affect the result of the current experiment. The measurement was done on PFO dispersed at the concentration of 10^{-4} M in a PMMA film that was subsequently annealed at 200 ^{o}C for 2h in N_2 to increase the absorption shoulder originating from the aggregate states, PL spectra of the g-band obtained with different excitation wavelengths are shown in Fig. 2-14a. In the 490-540 nm region, the emission intensity excited at 360 nm is stronger than that excited at 476 nm due to a tail of the strong blue emission. However, in the 540-640 nm region, both spectra are almost same. In Fig. 2-14b, we further plotted a difference spectrum obtained by subtracting the 476 nm excited spectrum from the 360 nm excited one. The difference spectrum should represent the blue emission tail, and when overlaid with the spectrum of the short-lifetime component (Fig. 2-12a) there is a very good match between the spectra. This observation confirms that the short-wavelength difference in the spectra in Fig. 2-14a is due to the blue emission tail and that there is no significant difference in the g-band spectrum between the 360 nm and the 476 nm excitation wavelength. This leads to a conclusion that excimers excited via monomer like states at 360 nm do not significantly contribute to the g-band emission. On the other hand, this result does not exclude the possibility of population of excimer-like states via the ground-state (H) aggregates, as proposed previously [39].
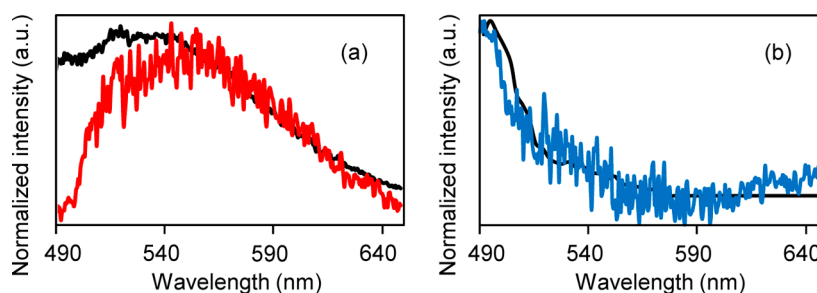
Fig. 2-14 (a) PL spectra of the g-band region measured with excitation wavelengths of 360 nm (black line) and 476 nm (red line). (b) Difference spectrum obtained by subtracting the 476 nm excited spectrum from the 360 nm excited one (blue line) and spectrally resolved 0.34 ns component of PL lifetime (black line).

2-3-6. Assignment of the g-band

The above results leave H-aggregates and CT complexes as the main potential candidates of g-band emission in PFO. Recently, the appearance and properties of J- and H-aggregates in conjugated polymers have been studied theoretically [43] and experimentally [44]. It was found that the red-shifted PL spectra of H-aggregates are broader than those of monomers and that they retain their vibronic structure [43]. In our single-chain study, we found two types of the g-band spectra, one with a vibronic structure located around 500 nm and the other structureless and distributed between 500 and 600 nm. Spectrally, these two types also correspond to two different lifetime components, 1.4 ns transition located around 500 nm and 5.1 ns transition located between 520 and 575 nm. It is thus conceivable to assign the shorter-wavelength vibrationally resolved spectra to H-aggregate emission and the longer-wavelength structureless spectra to either the emission from CT states or the emission from excimers populated via the H-aggregates. Both the H-aggregates and the CT complexes result from short-range (angstrom order) intrachain interactions in PFO molecules of compact chain conformations. Such

63

conformations can show dynamical behavior, and this has been observed in the form of spectral jumps on the level of single chains (Fig. 2-7d, 2-8d, and 2-9c). Even small conformational changes can lead to reversible formation of H-aggregates or CT complexes, which then work as energy traps for light excitations absorbed by the blue spectral forms. The blue emission spectra in Fig. 2-7b and 2-8b correspond to conformations without such energy traps. The spectral jumps then reflect conformational changes upon which a trap is formed, and depending on the efficiency of the energy transfer, such trap is partly or fully populated, resulting in combined blue and green or purely green emission spectra (Fig. 2-7b and 2-8b). In principle, conformational changes could also explain spectral jumps that would result from changing energy-transfer efficiency to a permanent trap, such as a fluorenone unit. However, a change from purely blue emission spectrum to purely green emission would require a conformational change that would cause energy-transfer efficiency to change from 0% or very low values to 100%. It has been shown previously that energy transfer in conjugated polymers proceeds most efficiently between chains (or different parts of the same chain) in a face-to-face configuration and less effectively along the main chain [45]. Therefore, for energy transfer efficiency to change from 0 to 100 %, the interchain distance has to change by much more than the Förster radius, which itself is on the order of several nanometers. Such large conformational changes of polymer chains in a solid matrix are much less likely than the angstrom-level changes required for the formation of aggregates, and the spectral dynamics observed for single PFO chains supports the molecular aggregate origin of the g-band emission. We note that about 10−20% of the molecules in the PS and PMMA matrices exhibited irreversible spectral changes from blue to green parts of the spectra. The apparent irreversibility could be a result of a limited observation time but could also reflect formation of the oxidized species that would form permanent energy traps in such chains.

2-4. Conclusion

Despite the extensive research efforts over the past two decades, the origin of green emission in polyfluorenes remains a controversial topic. Here, we attempted to contribute to the discussion on its origin by systematic single-molecule study complemented by ensemble photophysical characterization. As mentioned before, the origin of the green band is likely a combination of different mechanisms that include oxidation as well as aggregation. The results obtained here indicate that for the systems studied (PFO dispersed at low concentrations in different quality matrices or solvents), the dominant mechanisms behind the appearance of the green band are different forms of aggregation, including H-aggregation and possibly charge transfer or excimer formation. Though we do not exclude a contribution from oxidized species, these would constitute only a minor part of the green region photoluminescence.

2-5. Appendix

Basic photophysical properties of PFO in toluene

We measured absorption and photoluminescence (PL) spectra, PL quantum yield (PLQY) and PL lifetime of PFO in toluene in order to obtain the basic photophysical characterization of PFO. Absorption and PL spectra are shown Fig. 1. Absorption spectrum has single peak at 384 nm, and a molar extinction coefficient ε was 1.84×10^6 L mol⁻¹cm⁻¹. The PL spectrum has vibronic structure and 0-0 peak at 417 nm.
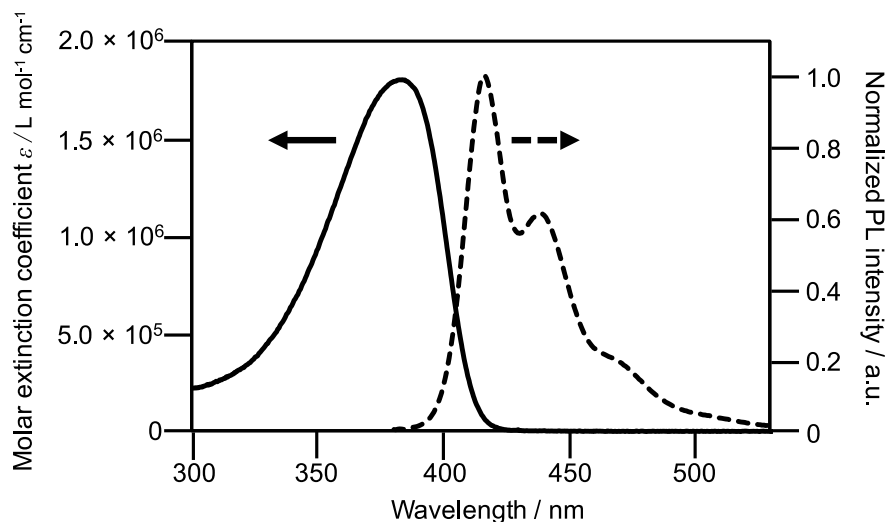

Fig. 2-15 Absorption (solid line) and PL (dashed line) spectra of PFO in toluene. The PL spectra were excited at 360 nm.

PLQY and lifetime are 0.88 and 0.47 ns, respectively. Lifetime τ and PLQY Φ are described in equations (2-1) and (2-2) using radiative rate constant k_r and nonradiative rate constant k_{nr} as

$$\tau = \frac{1}{k_r + k_{nr}} \tag{2-1}$$

$$\Phi = \frac{k_r}{k_r + k_{nr}} \tag{2-2}$$

Using the equations (1) and (2), and the measured values of τ and Φ we can obtain k_r and k_{nr}. The radiative rate k_r is related to oscillator strength f of an optical transition as in equation (3).

$$k_r \approx v_0 \times f \qquad (2\text{-}3)$$

where v_0 is wave number of the 0-0 fluorescence peak. PLQY, lifetime τ, k_r, k_{nr} and f are summarized in Table 2-2.

Table 2-2 Photophysical properties of PFO in toluene

	PLQY	τ / ns	k_r / s^{-1}	k_{nr} / s^{-1}	f
PFO in toluene	0.88	0.47	1.9×10^9	2.6×10^8	2.7

Table S1. Photophysical properties of PFO in toluene

Construction of spectral dependence of individual lifetime components

Construction of the spectral dependences of individual lifetime components of PL decay is shown symbolically in the Fig. 2-16. The PL decays were recorded with 3 nm increments within the detection range from 390 nm to 650 nm. At each detection wavelength the decays were fitted with a sum of three exponential decay functions and the three main components τ_i were identified as 0.34 ns, 1.4 ns and 5.1 ns. Further, these lifetime components together with their weights A_i obtained from the fitting were used to calculate the integrated intensity emitted at each wavelength within each lifetime comp
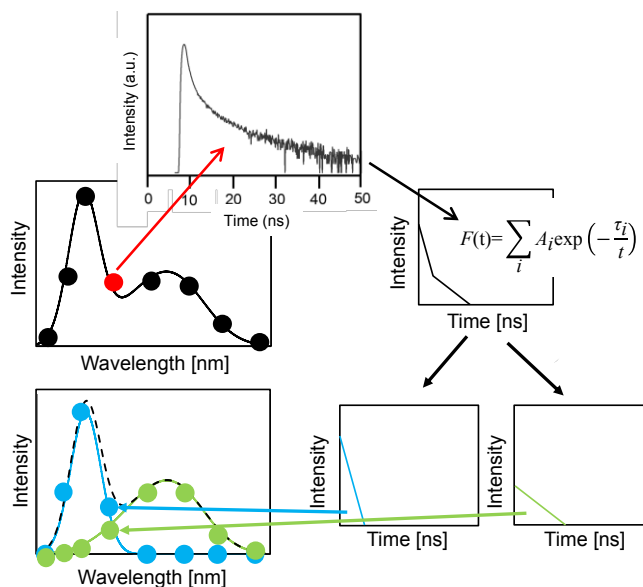
comp

Fig. 2-16 Schematic illustration of the construction of spectral dependence of lifetime components

2-6. References

1. D. L. Horrocks and W. G. Brown, *Chem. Phys. Lett.* **1970**, *5*, 117-119.

2. I. Prieto, J. Teetsov, M. A. Fox, D. A. Vanden Bout and A. J. Bard, *J. Phys. Chem. A* **2001**, *105*, 520-523.

3. G. Klaner, M. H. Davey, W. D. Chen, J. C. Scott and R. D. Miller, *Adv. Mater.* **1998**, *10*, 993-997.

4. M. Kreyenschmidt, G. Klaerner, T. Fuhrer, J. Ashenhurst, S. Karg, W. D. Chen, V. Y. Lee and R. D. Miller, *Macromolecules*, **1998**, *31*, 1099-1103.

5. S. Setayesh, A. C. Grimsdale, T. Weil, V. Enkelmann, K. Mullen, F. Meghdadi, E. J. W. List and G. Leising, *J. Am. Chem. Soc.* **2001**, *123*, 946-953.

6. A. P. Kulkarni and S. A. Jenekhe, *Macromolecules*, **2003**, *36*, 5285-5296.

7. M. Gaal, E. J. W. List and U. Scherf, *Macromolecules*, **2003**, *36*, 4236-4237.

8. L. Romaner, A. Pogantsch, P. S. Freitas, U. Scherf, M .Gaal, E. Zojer, E. J. W. List, *Adv. Funct. Mater.* **2003**, *13*, 597-601.

9. X. H. Yang, F. Jaiser, D. Neher, P. V. Lawson, J. L. Bredas, E. Zojer, R. Guntner, P. S. Freitas, M. Forster, U. Scherf, *Adv. Funct. Mater.* **2004**, *14*, 1097-1104.

10. B. He, J. Li, Z. Bo and Y. Huang, *Polymer Journal*, **2007**, *39*, 1345-1350.

11. B. Kobin, F. Bianchi, S. Halm, J. Leistner, S. Blumstengel, F. Henneberger and S. Hecht, *Adv. Funct. Mater.* **2014**, *24*, 7717-7727.

12. M. Sims, D. D. C. Bradley, M. Ariu, M. Koeberg, A. Asimakis, M. Grell and D. G. Lidsey, *Adv. Funct. Mater.* **2004**, *14*, 765-781.

13. K. Becker, J. M. Lupton, J. Feldmann, B. S. Nehls, F. Galbrecht, D. Gao and U. Scherf, *Adv. Funct. Mater.* **2006**, *16*, 364-370.

14. W. Zhao, T. Cao and J. M. White, *Adv. Funct. Mater.* **2004**, *14*, 783-790.

15. L. Liu, S. Tang, M. Liu, Z. Xie, W. Zhang, P. Lu, M. Hanif and Y. Ma, *J. Phys. Chem. B* **2006**, *110*, 13734-13740.

16. L. Liu, P. Lu, Z. Xie, H. Wang, S. Tang, Z. Wang, W. Zhang and Y. Ma, *J. Phys. Chem. B* **2007**, *111*, 10639-10644.

17. G. Klarner, J. I. Lee, V. Y. Lee, E. Chan, J. P. Chen, A. Nelson, D. Markiewicz, R. Siemens, J. C. Scott and R. D. Miller, *Chem. Mater.* **1999**, *11*, 1800-1805.

18. G. Wu, C. Yang, B. Fan, B. Zhang, X. Chen and Y. Li, *Journal of Applied Polymer Science*, **2006**, *100*, 2336-2342.

19. R. Grisorio, G. P. Suranna, P. Mastrorilli and C. F. Nobile, *Adv. Funct. Mater.* **2007**, *17*, 538-548.

20. S. P. Mucur, R. Kacar, C. Meric and S. Koyuncu, *Organic Electronics*, **2017**, *50*, 55-62.

21. A. Calzolari, B. Vercelli, A. Ruini, T. Virgili and M. Pasini, *J. Phys. Chem. C* **2013**, *117*, 26760-26767.

22. Y. Chen, X. You, X. Zhang, X. Zhang, B. Liu, W. Lai and W. Huang, *J. Appl. Polym. Sci.* **2017**, *134*, 44950-44956.

23. E. Khodabakhshi, J. J. Michels, and P. W. M. Blom, *AIP ADVANCES*, **2017**, *7*, 075209.

24. K. A. Luck, H. N. Arnold, T. A. Shastry, T. J. Marks and M .C. Hersam, *J. Phys. Chem. Lett.* **2016**, *7*, 4223-4229.

25. B. Liu, J. Lin, Z. Lei, M. Sun, L. Xie, W. Xue, C. Yin, X. Zhang and W. Huang, *Macromol. Chem. Phys.* **2015**, *216*, 1043-1054.

26. L. Bai, B. Liu, Y. Han, M. Yu, J. Wang, X. Zhang, C. Ou, J. Lin, W. Zhu, L. Xie, C. Yin, J. Zhao, J. Wang, D. D. C. Bradley and W. Huang, *ACS Appl. Mater. Interfaces*, **2017**, *9*, 37856-37863.

27. P. F. Barbara, A. J. Gesquiere, S. J. Park and Y. J. Lee, *Acc. Chem. Res.* **2005**, *38*, 602-610.

28. D. Woll, E. Braeken, A. Deres, F. C. Schryver, H. Uji-I and J. Hofkens, *Chem. Soc. Rev.* **2009**, 38, 313-328.

29. F. Kulzer, T. Xia, M. Orrit, *Angew. Chem. Int. Ed.* **2010**, *49*, 854-866.

30. M. Vacha and S. Habuchi, *NPG Asia Mater.* **2010**, *2*, 134-142.

31. J. M. Lupton, *Adv. Mater.* **2010**, *22*, 1689-1721.

32. K. Paeng and L. J. Kaufman, *Chem. Soc. Rev.* **2014**, *43*, 977-989.

33. H. P. Lu, *Chem. Soc. Rev.* **2014**, *43*, 1118-1143.

34. Z. Hu, B. Shao, G. T. Geberth, D. A. Vanden Bout, *Chem. Sci.* **2018**, *9*, 1101-1111.

35. S. S. Sartori, S. De Feyter, J. Hofkens, M. Van der Auweraer, F. De Schryver, K. Brunner, J. W. Hofstraat, *Macromolecules*, **2003**, *36*, 500-507.

36. Y. H. Kim and D. A. Vanden Bout, *Appl. Phys. A*, **2009**, *95*, 241-247.

37. E. Da Como, N. J. Borys, P. Strohriegl, M. J. Walter, and J. M. Lupton, *J. Am Chem. Soc.* **2011**, *133*, 3690-3692.

38. T. Adachi, J. Vogelsang and J. M. Lupton, *J. Phys. Chem. Lett.* **2014**, *5*, 573-577.

39. Y. Honmou, S. Hirata, H. Komiyama, J. Hiyoshi, S. Kawauchi, T. Iyoda and M. Vacha, *Nature Commun.* **2014**, *5*, 4666-4673.

40. H. Lin, S. R. Tabaei, D. Thomsson, O. Mirzov, P.- O. Larsson, I. G. Scheblykin, *J. Am. Chem. Soc.* **2008**, *130*, 7042-7051.

41. A. Monkman, C. Rothe, S. King, F. Dias, *Adv. Polym. Sci.* **2008**, *212*, 187-225.

42. A. Perevedentsev, N. Chander, J. S. Kim, D. D. C. Bradley, *J. Polym. Sci. B: Polym. Phys.* **2016**, *54*, 1995-2006.

43. H. Yamagata, F. C. Spano, *J. Chem. Phys.* **2012**, *136*, No. 184901.

44. T. Eder, T. Stangl, M. Gmelch, K. Remmerssen, D. Laux, S. Höger, J. M. Lupton, J. Vogelsang, *Nat. Commun.* **2017**, *8*, No. 1641.

45. E. Hennebicq, G. Pourtois, G. D. Scholes, L. M. Herz, D. M. Russell, C. Silva, S. Setayesh, A. C. Grimsdale, K. Müllen, J.-L. Bredas, *J. Am. Chem. Soc.* **2005**, *127*, 4744-4762.

Chapter III

Mechanically Induced changes of PL properties in Single PFO nanoparticles

3-1. Introduction

3-1-1. The features of π conjugated polymer nanoparticles (CPNPs)

π conjugated polymer nanoparticles (CPNPs) [1,2] have been studied extensively, with potential applications envisioned in solar cells [3], organic light emitting diodes [4-7], memory devices [8] and bioimaging [9]. In these applications, CPNPs can be viewed as environmentally friendly and non-toxic alternatives to colloidal quantum dots (QD). A crucial advantage is that CPNPs and their devices can be fabricated using water-based processes because they are formed by reprecipitation or miniemulsion aqueous methods, as compared to organic solvent processing of small-molecules or polymeric organic semiconductors. Apart from homopolymer CPNPs, more complex multicomponent "particle devices" containing charge transporting and light-emitting elements have been conceptually proposed [10]. In photovoltaic devices, such multicomponent donor-acceptor CPNPs showed higher short current density and fill factor than bulk-film heterojunction blend of the same materials [11]. Still, CPNPs devices usually show lower efficiency than bulk films and there is room for performance improvement. In the applications as fluorescence probes for bioimaging, the advantages of CPNPs are good fluorescence properties, photostability, nontoxicity and water dispersibility [12,13]. Energy transfer in multicomponent CPNP fluorescent probes has been used to engineer narrow-band and bright emitting particles for in vivo imaging [14,15]. Further, unlike single organic dye molecules or single QDs, single CPNP do not show the phenomenon of fluorescence intermittency, or blinking [16,17]. All these properties make CPNPs an attractive new class of materials for sensors and bioimaging applications.

As mentioned above, the phenomenon of energy transfer can be used to effectively engineer the CPNP properties. In blended donor-acceptor polymer nanoparticles, e.g., incorporation of only a few % of the acceptor polymer causes complete transfer of energy from the donor to the acceptor and fluorescence from the acceptor only [18]. This is an example of evidence that polymer chains in CPNPs are more densely packed than in films, and different from the solvated state in solutions. At the same time, the efficient interchain energy transfer leads to decrease of emission quantum yield because energy is also

trapped on quenching sites [19]. Therefore, aggregation states including conformations and chain packing that are related to energy transfer are key factors in fluorescence properties of CPNPs. From a different point, combination of polyfluorene derivatives with Pt-octaethylporphine (PtOEP) in CPNPs can make use of efficient energy transfer to and phosphorescence from the PtOEP to effectively detect oxygen via the phosphorescence quenching [20]. These examples show that fundamental knowledge on the relationship between fluorescence properties, energy transfer, chain packing and conformation is essential for further development of CPNPs.

3-1-2. Controlling the photophysical properties of π conjugated polymers by external force

One important physical parameter that has been largely overlooked is the effect of external (hydrostatic) pressure, which causes mechanical modulation of the sample and in turn affects the fluorescence properties via changes in chain packing, interchain interactions or conformation. Studies on hydrostatic pressure effect on conjugated polymers films of the poly(p-phenylene vinylene) family reported fluorescence red shift and intensity decrease with increasing pressure due to planarization of chain and increase of aggregation [21-22]. Applying pressure on nanometer scales can, on the other hand, lead to qualitatively different results. We showed previously that MEH-PPV nanoparticles undergo blue shift of fluorescence spectra and intensity increase upon localized application of force using a tip of an atomic force microscope (AFM). The small size of the tip causes disruption of the chain conformation accompanied by decrease of conjugation length [23]. CPNPs often show such unexpected features and many of their properties still remain unexplained. Similar method of fluorescence microscopic monitoring of nanoscale mechanical changes induced by AFM tip has been used to study pressure-related effects in single dye molecules [24] and QDs [25], or mechanofluorochromism of single organic nanocrystals [26].

3-1-3. Strategy and purpose

Next to poly(phenylene vinylene) based compounds, polyfluorenes (PF) represent important class of conjugated polymers and have been widely studied both for academic purpose and for potential applications. In particular, poly(9,9-dioctylfluorene) (PFO) shows blue emission with high efficiency both in fluorescence and electroluminescence, good charge mobility and thermal stability. It exists in two main conformational states, disordered glassy phase and well-defined planar β-phase [27,28]. Nanoparticles (NP) can be prepared from PFO by reprecipitation method similar to other conjugated polymers, and can have β-phase induced by post-treatment with organic solvents [29]. Other ways to control the amount of β-phase in the NPs include, e.g., side-chain engineering [30,31].

Here, we study the relationship between photophysical properties and chain packing including chain conformation on the level of single polyfluorene nanoparticles. We measured fluorescence spectra and intensity of different sizes of NPs and simultaneously applied local external pressure using an AFM tip to modify and control the PFO chain packing inside the NPs. We find strong effects of both inhibition and enhancement of fluorescence intensity depending on the extent of external pressure. These intensity changes are accompanied by various degrees of spectral changes that reflect the conformational modifications of PFO chains, as well as by changes in fluorescence polarization anisotropy. Apart from providing fundamental knowledge on the relationship between photophysical and structural properties of the PFO nanostructures, these results also provide important feedback for potential application in which PFO NPs would be used as emitters in flexible optoelectronic devices.

3-2. Experimental section

3-2-1. Sample Preparation

Poly(9,9-di-n-octylfluorene) (PFO) was purchased from Aldrich (Mn 23566 g/ mol, polydispersity index PDI 3.45). PFO nanoparticle (PFONPs) were prepared by the reprecipitation method [8, 15]. First, 1.25×10^{-6} M of PFO in THF solution was prepared and 1mL of this solution poured into 4 mL of pure water. Then it was sonicated for 20 min to disperse more uniformly. Next, it was heated at 80 °C to evaporate THF and form particle. This suspension was filtered by a 0.45μm filter to remove large particle. This nanoparticle solution poured onto cleaned quartz substrate and left standing for 1 min to let nanoparticles adsorb on the substrate. After that, it was spin coated at 3000 rpm for 30 s and sample was dried in vacuum for 1 h before the experiments.

3-2-2. Combined confocal and atomic force microscopic setup

The confocal and AFM measurements were carried out using a home-built setup (Fig. 3-1) that combines an inverted fluorescence microscope (IX 73, Olympus) with an AFM head (MFP-3D-SA, Asylum Research). The AFM cantilever used was AC200TS (Olympus). The applied force measurements were in the range of 100 nN to 5 μN. The accuracy of the AFM force measurements is associated with an error in the determination of the cantilever spring constant, which itself is on the order of 10%. The sample was excited with a 375 nm laser (LDH-D-C375, Pico Quant). Fluorescence from the sample was collected by an oil immersion objective lens (UplanFLN 100×, N.A. 1.3, Olympus) and passed through a dichroic mirror (Dichro 375, Chroma) and a long-pass filter (LP 377, Edmund). The objective lens was mounted on a three-axis piezo stage (PS3L60-030U, NC3311, Nanocontrol) to accurately align its center position with respect to the AFM tip. The fluorescence signal was detected by an avalanche photodiode detector (SPCM-AQR-14-S, SEIKO EG&G) in the confocal mode or by an electron-multiplying charge- coupled device (EMCCD) camera (iXon, Andor Technology) equipped with an imaging spectrograph (CLP-50LD, Bunkou Keiki) to measure fluorescence spectra from

individual NPs. The integration time and gain of EMCCD were 0.1 s and 300, respectively. The absorption (excitation) and fluorescence polarization anisotropy were measured by placing a linear polarizer in either the excitation or detection path.
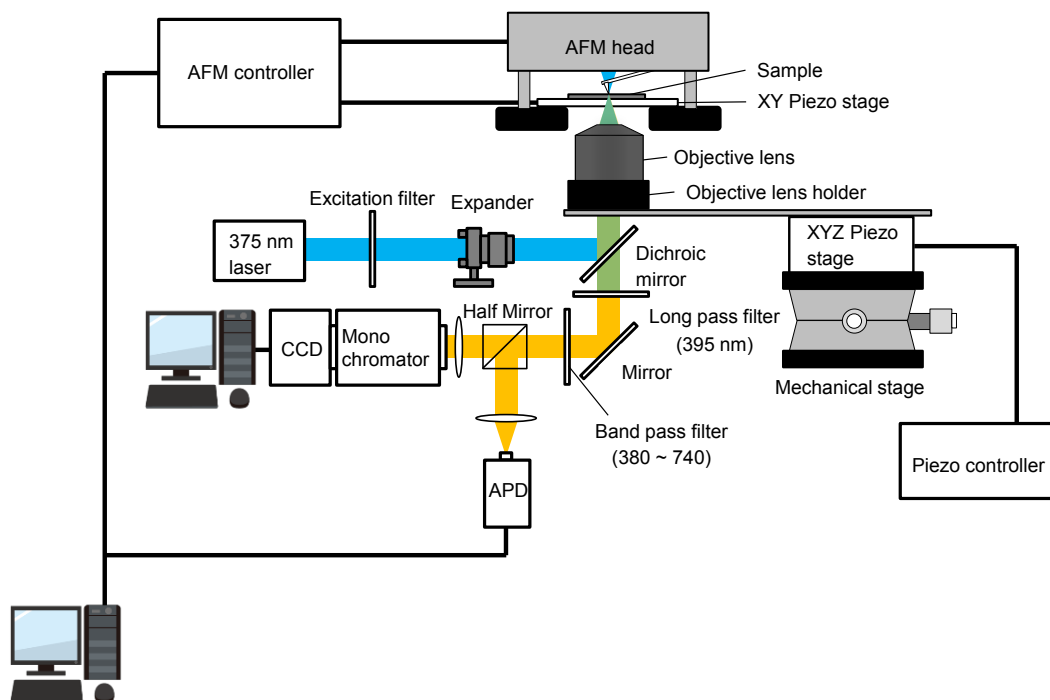
Fig. 3-1 Experimental setup combining AFM and confocal microscope

3-2-3. TEM characterization

Transmission electron microscope images were taken with a Hitachi H7650 microscope with an accelerating voltage of 100 kV.

3-3. Results and Discussion

3-3-1. Characterization of the Nanoparticles.

The NPs were prepared by a reprecipitation method. The NP height measured by AFM was, on average, 27 nm with a large height distribution (Fig. 3-2a). TEM showed that most of the NPs have a symmetrical round shape (Fig. 3-2a, inset) with an average diameter of 53 nm. To estimate the number of PFO chains in one NP, we compared the average fluorescence intensity from single chains dispersed in a matrix with the fluorescence intensity of NPs under same experimental conditions. Assuming comparable fluorescence quantum efficiencies in both systems, the number of PFO chains is on the order of 100 or more. This number might be larger because the emission is often quenched in condensed phase such as the solid NPs. The absorption spectrum of a water dispersion of PFO NPs (Fig. 3-2b) is identical to that of the PFO solution, with the exception of an additional peak at 429 nm that is due to the presence of well-ordered β phase conformation. The red shift of the absorption is caused by the extended conjugation length in this conformation. The fluorescence spectrum of the PFONP dispersion (Fig. 3-2b) is also red-shifted from the PFO solution and shows the characteristic narrow-band vibronic progression of the β-phase.

Apart from the β-phase features, the fluorescence spectrum of the as-prepared PFO NPs does not show any signatures of the glassy phase or the green emission band that are typical for some preparation of PFO nanostructures. The β phase was formed during a preparation step that involved heating of the reprecipitated PFO to 80 °C to remove the remaining solvent.

To analyze in more detail the presence of the β-phase in individual NPs, we measured the fluorescence polarization anisotropy from a statistical sample of single PFO NPs and analyzed the data in terms of the polarization modulation depth, M_F, defined as $M_F = (I_{max} - I_{min})/(I_{max} + I_{min})$. Here I_{max} and I_{min} represent the fluorescence intensity maxima and minima, respectively, obtained while continuously rotating an analyzer placed in front of the detector. A distribution of M obtained on 35 PFO NPs (shown in the histogram Fig. 3-2c) implies a certain degree of orientation of the rigid β phase segments inside the NPs.

To reconstruct such an orientation, we performed numerical simulations, as detailed in the appendix. The simulations indicate that a minimum of three β phase segments are required to reproduce the experimental results. Fig. 3-2d shows an example of the spatial arrangement of such three segments. A statistical sample of random spatial orientations of this fixed segment combination well reproduces the modulation depth histogram, as also shown in Fig. 3-2c. A typical PFONP can thus be imagined as, on average, a 20−30 nm large nanostructure containing (at least) three straight β phase segments, with the remaining volume of the NP filled with glass-phase PFO. Efficient energy transfer from the glass phase to the β phase causes emission from the latter only, resulting in the pure β phase fluorescence spectra in Fig. 3-2b. The glass phase itself is distributed more randomly within the particle. This has been confirmed by absorption (excitation) polarization anisotropy measured on a statistical sample of single PFONPs and analyzed in terms of polarization modulation depth, M_A, defined similarly as $M_A = (I_{max} − I_{min})/(I_{max} + I_{min})$. The results are shown in a histogram in Fig. 3-6a in appendix. We note that the shapes of the histograms of the emission (Fig. 3-2c) and excitation (Fig. 3-6a) polarizations look similar. However, we observe large differences in the fractions of NPs with a modulation depth of 0.4 or lower. This fraction is 0.34 for the emission polarization and 0.64 for the excitation polarization, indicating the more oriented nature of the emitting β phase segments compared with the absorbing glass-phase chains. The more random orientation of the glass-phase segments is also seen in the results of the simulated polarization anisotropy (shown in Fig. 3-6b). The experimental histogram is best reproduced with three segments oriented more-or-less evenly in 3D space, confirming the random nature of the glass phase within the NPs. We note, however, that the orientation is not completely random, as we have not observed any particles with zero modulation depth.
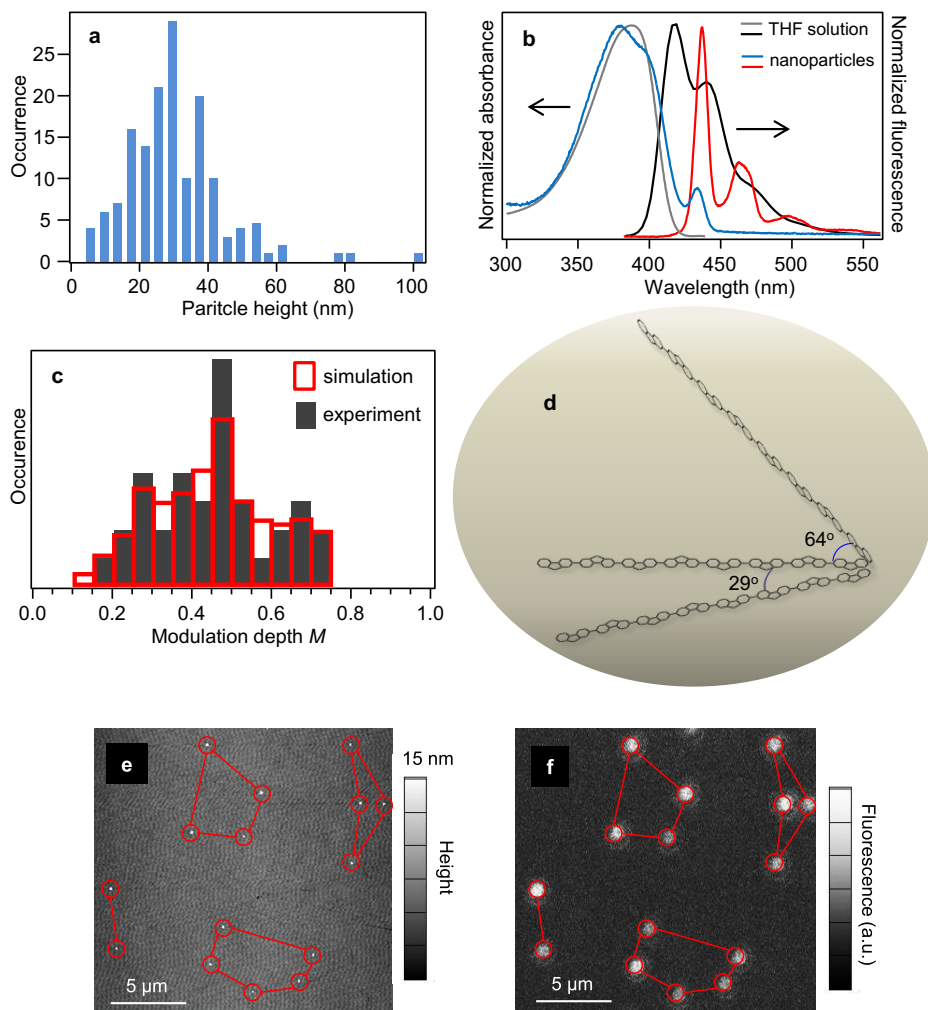
Fig. 3-2. Characterization and imaging of the PFO nanoparticles. (a) Distribution of the particle height measured by AFM. Inset: TEM image. (b) Absorption and fluorescence spectra of PFO in THF solution and of the water dispersion of PFO nanoparticles. (c) Measured (filled gray bars, 35 nanoparticles) and simulated (open red bars, 50 000 data points) modulation depth distributions of fluorescence polarization traces. (d) Example of the spatial arrangement of three β-phase segments that best reproduce the measured modulation depth distribution in panel c. (e) AFM and (f) confocal fluorescence microscopic images of individual PFO nanoparticles dispersed on quartz substrate.

3-3-2. Mechanically Induced fluorescence quenching.

To perform the simultaneous AFM and confocal microscopy, identical PFONPs have to be localized in both microscopic modes. This requires precise alignment of the position of the center of the objective lens with the cantilever tip of the AFM, which is placed on top of the inverted fluorescence microscope. Fig. 3-3e,f shows the simultaneously measured AFM and fluorescence images. All of the features present in the fluorescence image are clearly identified at the same positions in the AFM image. These experiments are carried out in a nitrogen atmosphere to prevent oxidation and photobleaching.

After zooming in on a single NP, we carried out simultaneous fluorescence intensity and force curve monitoring. Fig. 3-3a shows a time trace of the fluorescence before, during, and after the application of a force of 1 μN. The fluorescence intensity dropped to 48% as a result of the applied force and recovered completely after the retraction of the AFM tip. This effect is completely reproducible on the same particle; that is, the repeated application of a 1 μN force in the same spot causes quenching, and the fluorescence intensity recovers after each retraction of the AFM tip.

Fluorescence spectra monitored at the same time (Fig. 3-3b, all spectra normalized) show β-phase characteristic features in all three phases without any significant line shape change. This result indicates that applying a force of 1 μN does not affect the β phase conformation present in the NP. This observation is confirmed by monitoring the polarization modulation depth, M_F, before and during the application of the force. As seen in Fig. 3-3c, despite the fluorescence intensity drop, the M_F value of 0.34 ± 0.02 remains unchanged during the experiment, confirming that not only do the β-phase segments themselves remain intact but also their orientation in the NP does not change. The error of the M_F value is mainly due to the signal noise and was estimated from curve fitting and error propagation. The significant decrease in the fluorescence with the applied force therefore has to originate from the glass- phase PFO chains. We assume that the force of 1 μN leads to more dense chain packing of the soft amorphous PFO chains, resulting in strong interchain interaction. Such an interaction between polymer chains can cause an increase in the energy transfer as well as the promotion of aggregates that may function as quenching sites. The fluorescence intensity of PFONPs decreases due to the increased

population of the quenching site and the increased energy transfer.

To exclude other quenching effects, such as AFM tip induced quenching or changes in the refractive index due to the presence of the AFM tip, we carried out the same experiments using dye-doped polymer beads of comparable sizes. An example of force and fluorescence intensity curves is shown in Fig. 3-7 in appendix. As seen in the figure, the fluorescence beads do not show any fluorescence intensity changes with an applied force of 1 μN. Also, in principle, the decrease in the emission intensity can be due to the change in the shape of the NP during deformation and resulting changes in the collection efficiency of the optics. However, in the case of the PFONPs, the height is, on average, 27 nm, so the change in the geometry of even a completely crashed NP would be on this order, which is negligible in optical terms. We note that the above behavior (described in Fig. 3-3) was observed in ∼70% of NPs studied. The remaining 30% showed a spectral change and a further increase in fluorescence intensity after AFM tip retraction (Fig. 3-8). Such results will be discussed later.

Whereas the fluorescence intensity drop by the applied force is a common observation in all studied NPs, the extent of the quenching varies from particle to particle.

To quantify the extent, we calculated the quenching ratio R_q as $R_q = (I_0 - I_f)/I_0$, where I_0 is the fluorescence intensity before and If is the intensity during application of the force. The ratio R_q is plotted against the particle size (height) in Fig. 3-9 in appendix. There is a large spread of R_q values from 0.1 to almost 1 but no clear correlation between the particle size and the extent of quenching (as observed before [23]), even though larger particles (>50 nm) tend to be quenched less.
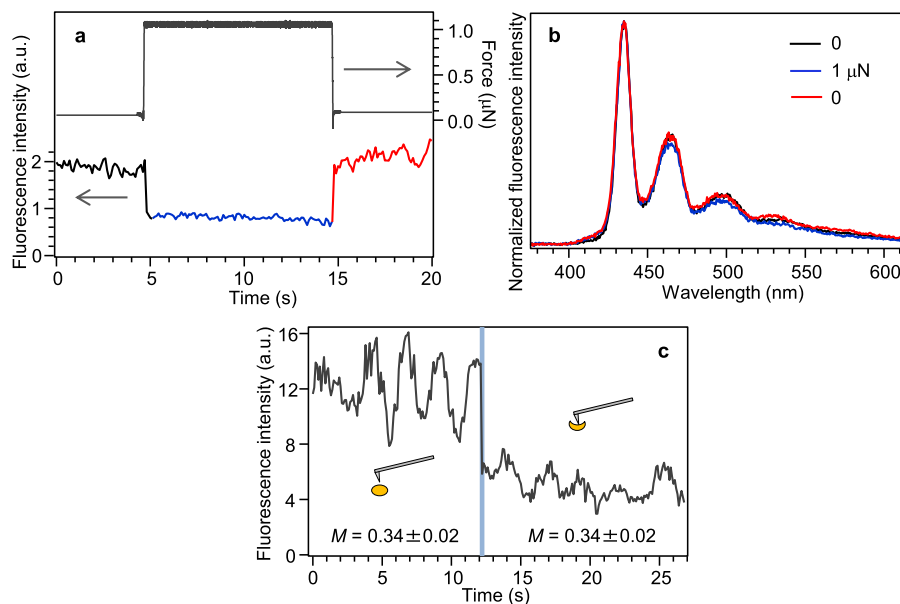
Fig. 3-3. Modification of fluorescence intensity. (a) Force curve (top) and simultaneously measured fluorescence intensity (bottom) from a single PFO nanoparticle. (b) Fluorescence spectra taken during the force curve measurement in panel a. The color code corresponds to the fluorescence intensity trace. (c) Polarization modulation of fluorescence from a single PFO NP before (left) and during (right) the application of a force of 1 μN. The curve was measured by continuously rotating an analyzer placed in front of the CCD detector.

3-3-3. Mechanically Induced Conformation Change.

To get more insight into the mechanism of the fluorescence intensity changes, we next looked at the effect of the magnitude of the applied force by gradually increasing the force in the order of 100 nN, 500 nN, 1.0 μN, and 5.0 μN. As shown in Fig. 3-4a, for forces between 100 nN and 1.0 μN, the fluorescence intensity decreased in the same way as previously described, presumably due to the generation of quenching sites and energy transfer to them. Interestingly, the quenching already happens with the lowest force of 100 nN and does not change when the force is increased to 1 μN. It appears that the

structural changes in the NP happened during the initial contact with the AFM tip and are not affected by a further increase of the force up to 1 μN. The most likely reason for this lack of change is the nature of the initial contact of the tip with the surface. This contact is probably a hard impact due to the attractive forces at the end of the attractive region of the tip approach. This initial "crash" of the tip onto the particle causes the quenching-related changes, and the further nominal increase in the force only compensates for the contact cantilever bending. However, when the applied force increased to 5.0 μN, the fluorescence intensity increased even above the initial precontact value. Thus, surprisingly, the qualitative change in the fluorescence properties depends on the magnitude of the applied force. The increase in the fluorescence intensity during the application of a 5 μN force was observed in 86% of the NPs studied, and the extent of the increase was, on average, 1.4. The remaining 14% showed only a decrease, as observed with lower applied forces. We note that there is not a permanent change to the particle shape (height) as a result of the applied force, as seen in Fig. 3-10 in appendix.

Fluorescence spectra taken during the sequence of increasing applied force are shown in Fig. 3-4b. In particular, the applied force of 5 μN causes breaking of the β-phase conformation and generation of the glass phase. The fraction of the glass phase further increases after retraction of the tip from the NP. The difference fluorescence spectrum obtained by subtracting the spectrum taken before applying the force from the one taken after retracting the tip (shown in Fig. 3-11) corresponds to the glass form of PFO. The spectral decomposition shows that whereas before applying the force, the spectrum was purely that of β-phase, after the tip retraction, the glass phase contributed 68% and the β-phase contributed 32% of the emission intensity.

Monitoring of the polarization modulation depth, M_F, before and during the application of the force (Fig. 3-4c) shows that the 5 μN force causes a complete depolarization of the emission, which accompanies the breakup of the β-phase. For other NPs, the modulation does not completely vanish but significantly decreases (Fig. 3-12 in appendix). In general, differences in the modulation depth values of the glass phase between the excitation and emission polarization measurements may be caused by the fact that due to efficient energy transfer the absorbing and emitting segments are different and thus the excitation and

emission polarization measurements probe different segments. All of the above experimental evidence can be summarized into a picture in which the strong AFM force physically disrupts the straight β phase segments and breaks them into multiple randomly oriented glass-phase segments, each emitting independently. We assume that the increase in the fluorescence intensity by the 5 μN applied force is caused by such an increase in the number of light-emitting segments. To estimate the actual increase in the number of segments, we use the results of an investigation of the conjugate length of the glass phase and the β phase PFO [32]. It has been shown that whereas glass-phase conjugated segments typically contain 8 ± 1 fluorene monomer units, the β phase conjugation extends to 30 ± 12 fluorene units. Therefore, a simple estimate shows that a breakup of a β phase segment can generate about four glass-phase segments. The number increase alone would not necessarily lead to a fluorescence intensity increase because of possible differences in fluorescence quantum yield (PLQY) between the two conformations. The PLQY of the β phase PFO remains an open question. There have been conflicting reports on a PLQY decrease with increasing β phase fraction [33] and on a PLQY increase with increasing β phase fraction [34] as well as reports indicating that the PLQY increase peaks for a certain β phase fraction and decreases with a further β phase content increase [35-36]. In all cases that show at least a partial PLQY positive trend, the increase is from ~0.5 to 0.7 [34-36]. A temperature dependence study of the PLQY of different PFO morphologies also indicates that at room temperature the glassy and β phase PLQYs are comparable [37]. These contradictory results do not enable us to discuss quantitatively the fluorescence intensity increase upon breaking the β phase segments but make the quantitative explanation plausible.

In addition, our results on applying a force of 1.0 μN range can contribute to the PLQY discussion. We have shown (in Fig. 3-3a) that for the same content of the β-phase, the fluorescence intensity (and, consequently, the PLQY) can decrease by as much as 90% depending on the conformation or chain packing of the remaining glassy phase. Thus, apart from the β-phase content, the actual morphology of the whole PFO sample is a crucial parameter for the overall PLQY.
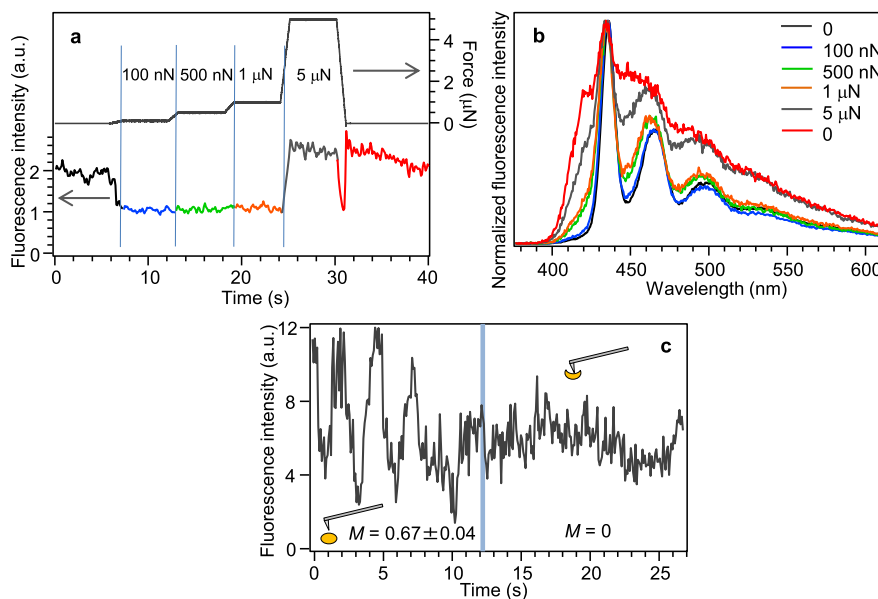
Fig. 3-4. Conformation change. (a) Force curve (top) and simultaneously measured fluorescence intensity (bottom) from a single PFO nanoparticle for different values of the applied force. (b) Fluorescence spectra taken during the force curve measurement in panel a. The color code corresponds to the fluorescence intensity trace. (c) Polarization modulation of fluorescence from a single PFO NP before (left) and during (right) the application of a force of 5 µM. The curve was measured by continuously rotating an analyzer placed in front of the CCD detector.

3-3-3. Mechanically Assisted Photodegradation.

All of the above experiments were conducted in a nitrogen atmosphere. It is, however, instructive to examine the effect of air under the same experimental conditions. The following results were obtained under ambient conditions. Fig. 3-5a compares the photo-degradation of a single PFONP caused by continuous illumination in air for the cases with and without an applied force of 1 µN. Without applying external force, the fluorescence intensity decreases to ~72% over the measurement interval of 30 s. The force of 1 µN causes a sudden drop in the intensity to 34%, which is partly recovered after the retraction of the tip. Still, the recovered intensity level is only at 58% of the original fluorescence

intensity value. There is even a much stronger effect of the applied force on the fluorescence spectra. As shown in Fig. 3-5b, without applying the force, the NP emission stays fully β-phase-like without any line shape change, showing only an intensity decrease (as also evident from the normalized spectra in Fig. 3-13 of appendix). The application of the 1 μN force causes the almost complete disappearance of the β phase emission, and after retracting the tip, the spectrum is purely that of a glass phase with a strong contribution of the green band around 550 nm (best seen in the normalized spectra in Fig. 3-14 of appendix). Interestingly, in terms of the absolute intensity, the contribution of the green band is the same before and after applying the force; in other words, the β phase was not transformed into the green band as a result of the degradation.

We have previously shown that in a nitrogen atmosphere the force of 1 μN does not destroy the β phase segments but only changes the chain packing of the glass phase. We may speculate that the mechanical disturbance and reorientation of the β phase surrounding chains (and possibly part of the β phase segments themselves) facilitate the diffusion of oxygen toward the β phase segments and cause the degradation. If the degradation happened randomly on any monomer unit within the β phase segment, then it would lead to the breakup of the conjugation and the appearance of a glass-like conformation. Still, the product of such mechanically assisted photodegradation (presumably fluorenone species) is not causing an increase in the green band emission. This could be consistent with the idea that the green emission is caused by interchain excimers formed by the fluorenone units, and such excimers would not be formed on the straight β-phase segments [38].
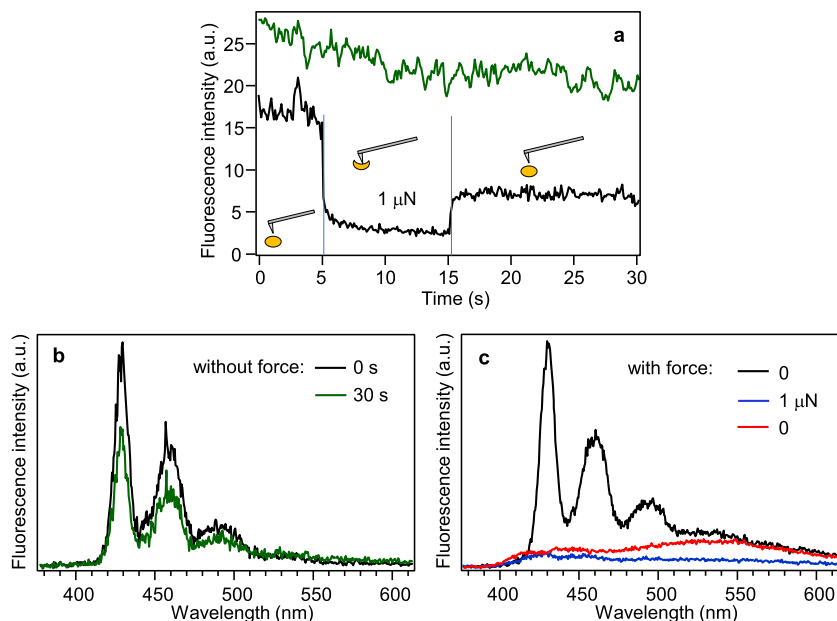
Fig. 3-5. Mechanically assisted photodegradation. (a) Fluorescence intensity traces from two single PFO nanoparticles in air without (top trace) and with (bottom trace) an applied force of 1 μN. (b) Fluorescence spectra from the single nanoparticle measured without an applied force at the start (0 s, black) and end (30 s, green) of the measurement interval. (c) Fluorescence spectra from a single nanoparticle before (black), during (blue), and after (red) applying a force of 1 μN.

3-3-4. Comparison of the PFO NP Properties with a Neat PFO Film.

For the comparison with bulk neat films of PFO, we first measured AFM force curves on individual NPs and on different locations of a spin-coated and annealed film. The force curves were analyzed using the Derjaguin−Muller−Toporov(DMT) theory, as previously described [23]. An average Young's modulus was 9.6 GPa for the PFONPs and 29.2 GPa for the PFO film, respectively. The more than three-fold decrease in the Young's modulus for the NPs reflects changes in the physical properties (such as the glass-transition temperature) caused by the confinement of the PFO chains in the nanostructures.

Pressing the film with the AFM tip with a 5 μN force results in local deformation, as seen in the AFM topology image in Fig. 3-15 of appendix. A fluorescence image of the same area of the film shows decreased fluorescence intensity from the deformed locations. However, contrary to the results obtained with the same force on individual NPs, there is almost no change in the fluorescence spectra from the deformed areas. Both the original film and the pressed locations show pure β-phase emission (Fig. 3-15). This result points to the unique possibility of the mechanical manipulation of the spectroscopic properties of polymer NPs.

3-4. Conclusion

We have explored the effect of nanoscale mechanical pressure on the photophysical properties of PF NPs. Depending on the environment and on the magnitude of the applied force, the nanomechanical manipulation can result in both fluorescence quenching and enhancement, in a spectrally monitored conformational change and in accelerated photodegradation. The results will not only be important for the fundamental photophysics of conjugated polymers but also will provide feedback for potential applications of polymer NPs in flexible optoelectronic devices and could point toward the use of such NPs for light-monitored pressure sensors.

3-5. Appendix

Numerical simulation of β-phase segment orientation inside the PFONPs

β-phase is an ordered and straight conformation segment and is often observed in bulk films after annealing by thermal treatment or solvent vapor. Therefore, it is an interesting question how is β-phase incorporated and oriented in PFO NPs. To reveal this, we measured modulation depth of fluorescence polarization traces on individual PFO NPs without applying force. Although β-phase is three-dimensionally oriented in the PFO NPs, this orientation can be observed only projected into the two dimensions of the sample plane because PFO NPs are much smaller than diffraction limit of light and the emitting components cannot be distinguished. Therefore, we performed numerical simulation of polarization modulation depth to reveal the angles between individual β-phase segments within 1 NP. The projected angle in the sample plane will be changed by 3-dimensional orientation change (rotation). It can increase or decrease depending on the direction of rotation. In the numerical simulation, we started with two β-phase segments but found out that a minimum of three β-phase segments are required to reproduce the results. The angle between molecules 1 and 2 (θ), the angle between molecules 1 and 3 (φ), the angle between a common plane formed by molecules 1 and 2 and molecule 3 (χ) were decided and rotated around x and y axis in random steps. For each step modulation depth MF was calculated as $(I_{max} - I_{min})/(I_{max} + I_{min})$. This process was repeated for 10000 steps and a histogram of MF was constructed. The combination of the angles (θ, φ, χ) which resulted in best reproduced experimental histogram of M was (29º, 9º, 63º). The relatively small values of the angles θ and φ cause a degree of orientation of the β-phase segments in the PFO NPs.

The numerical simulations of the absorption (excitation) polarization anisotropy were carried out in a similar way, using three effective glass-phase segments to reproduce the distribution of the absorption modulation depth MA. The results shown in Fig. S1 confirm the random nature of the glass phase, with the angles (θ, φ, χ) of (106º , 72º, 26º).
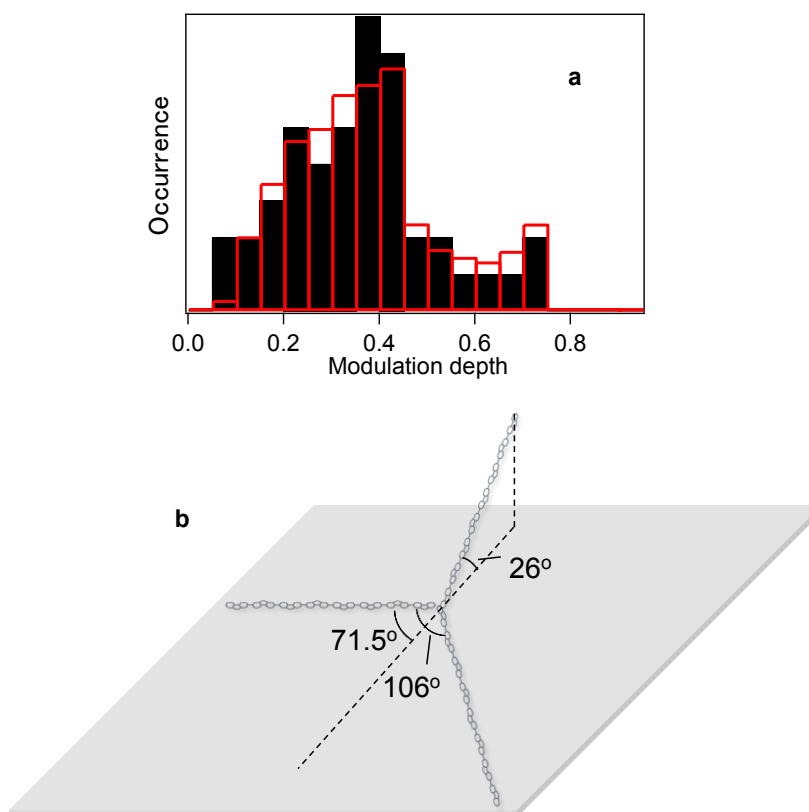
Fig. 3-6 a) Measured (full black bars, 45 NPs) and simulated (open red bars, 50,000 data points) modulation depth of absorption (excitation) polarization traces; b) An example of spatial arrangement of three glass-phase segments that represent the overall measured modulation depth distribution in a).
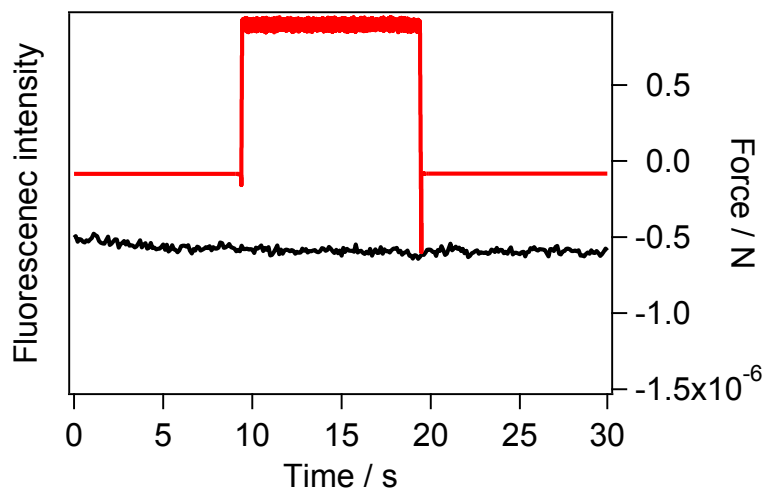
Fig. 3-7. Force curve (red) and simultaneously measured fluorescence intensity (black) from a single fluorescent bead Envy Green.
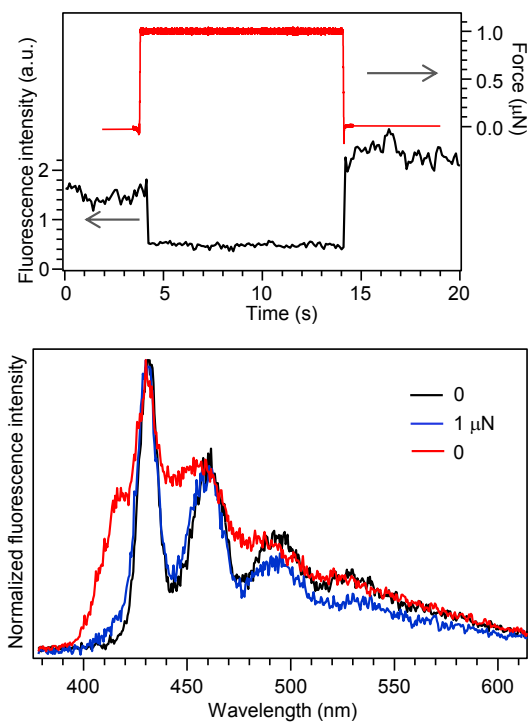

Fig. 3-8. Top: Force curve (red) and simultaneously measured fluorescence intensity (black) from a single PFO nanoparticle; Bottom: Fluorescence spectra taken before (black), during (blue) and after (red) applying the force.
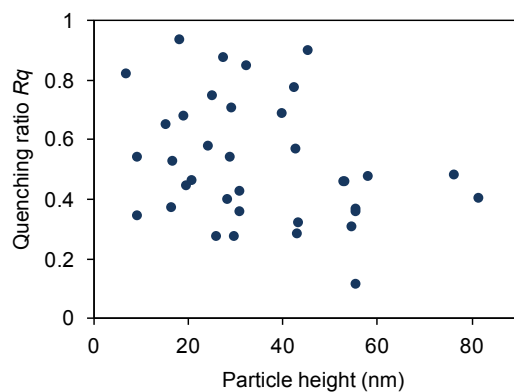
Fig. 3-9. Quenching ratio *Rq* as a function of the nanoparticle height measured by AFM.
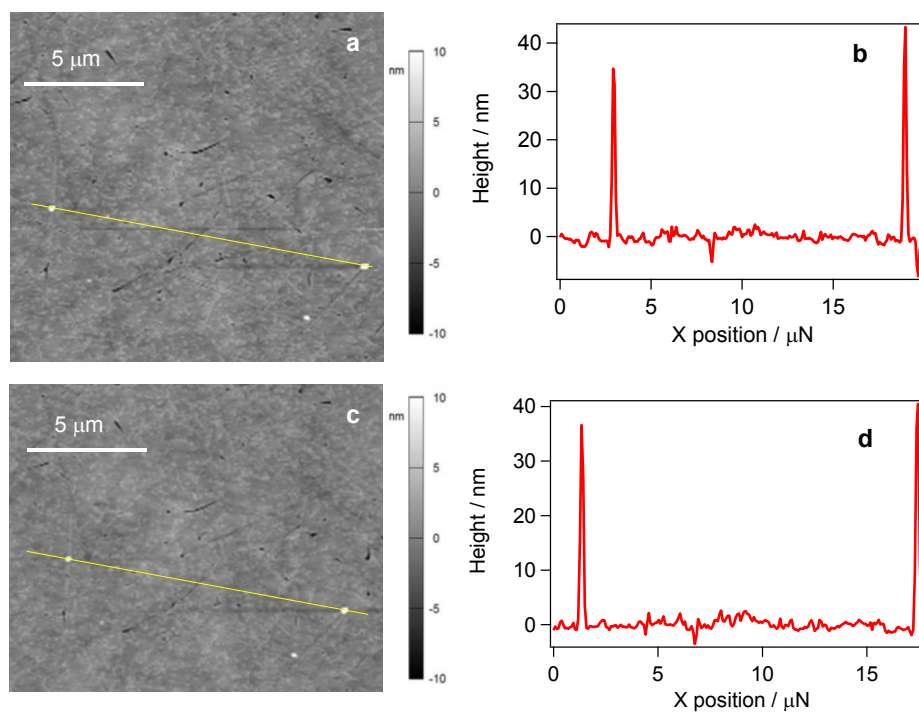
Fig. 3-10. AFM images (a, c) of 3 NPs before (a) and after (b) applying the force of 5 mN. The profiles of the top two NPs are shown in b) before and in d) after applying the force.
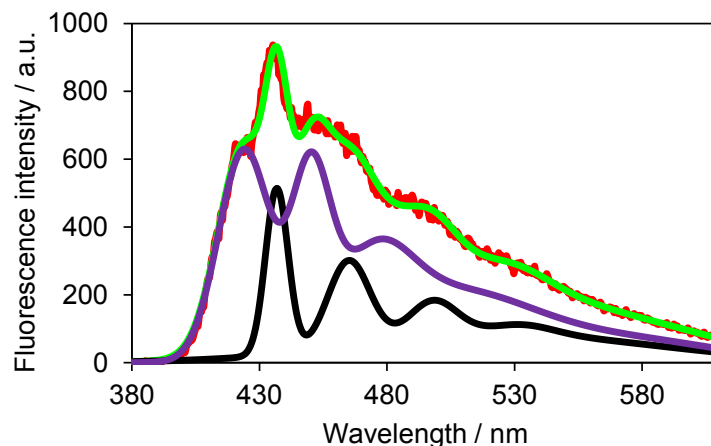
Fig. 3-11. Red: Fluorescence spectrum of a single PFO NP measured after applying the force of 5μN; Black: Multiple-Gaussian fit of a spectrum before applying the force; Purple: Multiple Gaussian fit of a difference spectrum obtained by subtracting the spectrum before applying the force from the one after applying the force. Green: Sum of the black and purple curves.
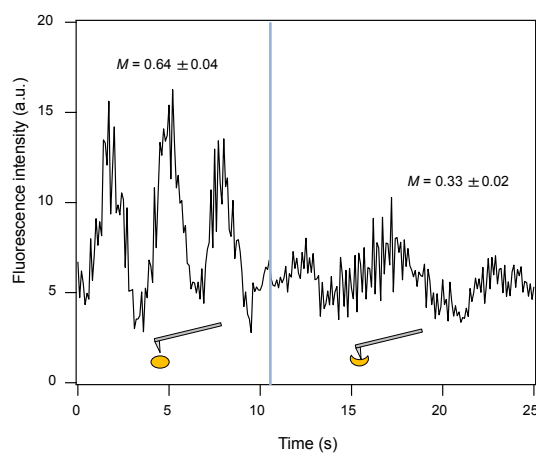
Fig. 3-12. Polarization modulation of fluorescence from a single PFO NP before (left) and during (right) application of a force of 5 mM. The curve was measured by continuously rotating an analyzer placed in front of the CCD detector.
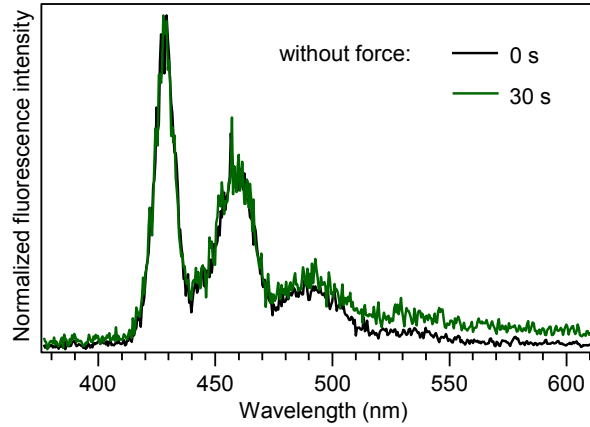
Fig. 3-13. Fluorescence spectra from a single PFO NP measured in air without an applied force at the start (0 s, black) and end (30 s, green) of the measurement interval, normalized at the 0-0 band.
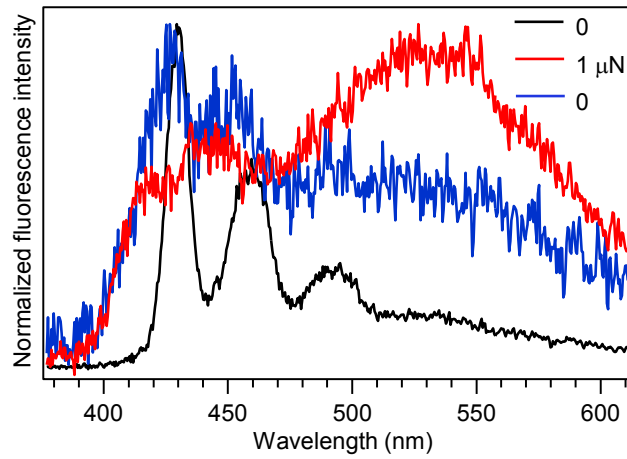

Fig. 3-14. Fluorescence spectra from a single PFO NP before (black), during (blue) and after (red) applying a force of 1 mN. The spectra are normalized at their respective maxima.
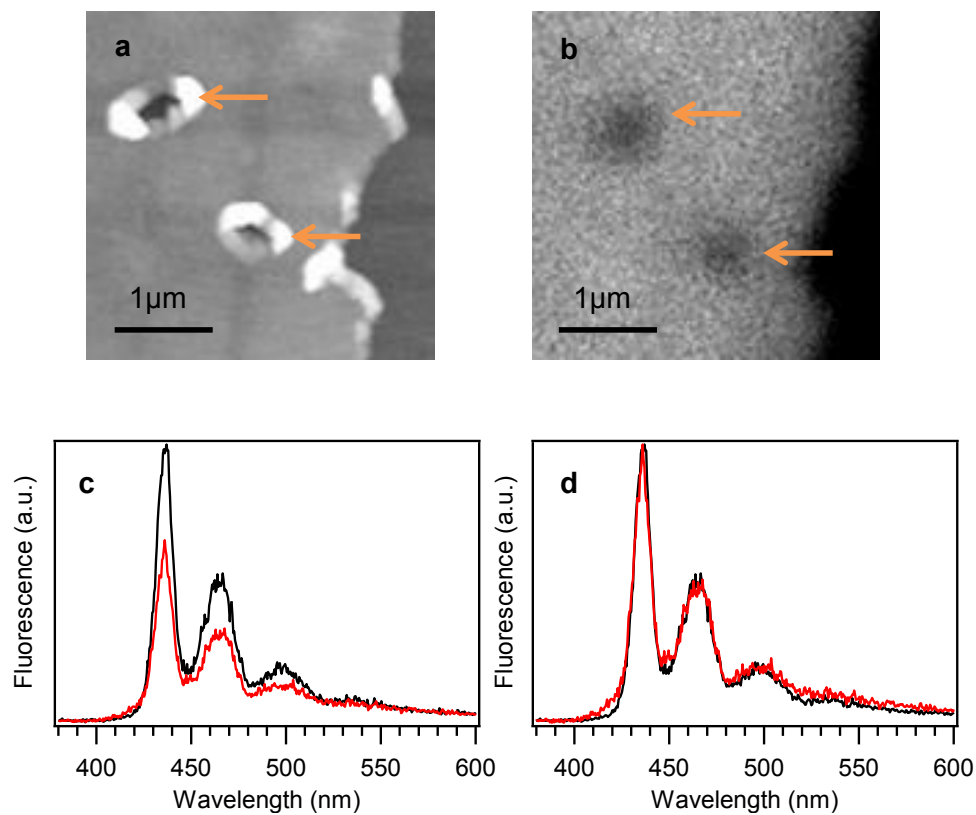
Fig. 3-15. a) AFM and b) fluorescence images of a bulk film of PFO spin-coated on a substrate. The arrows indicate locations that were mechanically pressed by the AFM tip with a force of 5 mN; c) Fluorescence spectra from an intact part of the film (black) and from the pressed part (red); d) Same spectra as in c) normalized at the 0-0 band

3-6. Reference

1. J. Pecher and S. Mecking, *Chem. Rev.* **2010**, *110*, 6260−6279.

2. D. Tuncel and H. V. Demir, *Nanoscale*, **2010**, *2*, 484−494.

3. T. Kietzke, D. Neher, K. Landfester, R. Montenegro, R. Guentner and U. Scherf, *Nat. Mater.* **2003**, *2*, 408−412.

4. T. Piok, S. Gamerith, C. Gadermaier, H. Plank, F. P. Wenzl, S. Patil, R. Montenegro, T. Kietzke, D. Neher, U. Scherf, K. Landfester and E. J. W. List, *Adv. Mater.* **2003**, *15*, 800−804.

5. G. Mauthner, K. Landfester, A. Koeck, H. Brueckl, M. Kast, C. Stepper and E. J. W. List, *Org. Electron.* **2008**, *9*, 164−170.

6. C. F. Huebner, R. D. Roeder and S. H. Foulger, *Adv. Funct. Mater.* **2009**, *19*, 3604−3609.

7. J. Y. Lin, J. Wong, L. H. Xie, X. C. Dong, H. Y. Yang and W. Huang, *Macromol. Rapid Commun.* **2014**, *35*, 895−900.

8. C. C. Shih, Y. C. Chiu, W. Y. Lee, J. Y. Chen and W. C. Chen, *Adv. Funct. Mater.* **2015**, *25*, 1511−1519.

9. C. Wu and D. T. Chiu, *Angew. Chem., Int. Ed.* **2013**, *52*, 3086−3109.

10. C. F. Huebner, J. B. Carroll, D. D. Evanoff, Y. Ying, B. J. Stevenson, J. R. Lawrence, J. M. Houchins, A. L. Foguth, J. Sperry and S. H. Foulger, *J. Mater. Chem.* **2008**, *18*, 4942− 4948.

11. N. A. D. Yamamoto, M. E. Payne, M. Koehler, A. Facchetti, L. S. Roman and A. C. Arias, *Sol. Energy Mater. Sol. Cells* **2015**, *141*, 171−177.

12. J. Liu, K. Li and B. Liu, *Adv. Sci.* **2015**, *2*, 1500008.

13. J. Wang, F. Lv, L. Liu, Y. Ma, S. Wang, *Coord. Chem. Rev.* **2018**, *354*, 135−154.

14. Y. Rong, C. Wu, J. Yu, X. Zhang, F. Ye, M. Zeigler, M. E. Gallina, I. C. Wu, Y. Zhang, Y. H. Chan, W. Sun, K. Uvdal and D. T. Chiu, *ACS Nano* **2013**, *7*, 376− 384.

15. C. S. Ke, C. C. Fang, J. Y. Yan, P. J. Tseng, J. R. Pyle, C. P. Chen, S. Y. Lin, J. Chen, X. Zhang and Y. H. Chan, *ACS Nano* **2017**, *11*, 3166−3177.

16. C. Wu, B. Bull, C. Szymanski, K. Christensen, J. McNeill, *ACS Nano* **2008**, *2*,

2415−2423.

17. C. Wu, T. Schneider, M. Zeigler, J. Yu, P. G. Schiro, D. R. Burnham, J. D. McNeill and D. T. Chiu, *J. Am. Chem. Soc*. **2010**, *132*, 15410−15417.

18. C. Wu, H. Peng, Y. Jiang and J. McNeill, *J. Phys. Chem. B* **2006**, *110*, 14148−14154.

19. Y. J. Ko, E. Mendez and J. H. Moon, *Macromolecules* **2011**, *44*, 5527−5530.

20. C. Wu, B. Bull, K. Christensen and J. McNeill, *Angew. Chem., Int. Ed.* **2009**, *48*, 2741−2745.

21. S. Webster and D. N. Batchelder, *Polymer* **1996**, *37*, 4961−4968.

22. R. K. Tikhoplav and B. C. Hess, *Synth. Met.* **1999**, *101*, 236−237.

23. H. Kobayashi, S. Hirata and M. Vacha, *J. Phys. Chem. Lett.* **2013**, *4*, 2591−2596.

24. S. Stöttinger, G. Hinze, G. Diezemann, I. Oesterling, K. Müllen and T. Basché, *Nat. Nanotechnol.* **2014**, *9*, 182−186.

25. T. Fischer, S. Stöttinger, G. Hinze, A. Bottin, N. Hu and T. Basché, *Nano Lett.* **2017**, *17*, 1559−1563.

26. M. Louis, C. Piñero García, A. Brosseau, C. Allain and R. Metivier, *J. Phys. Chem. Lett.* **2019**, *10*, 4758−4762.

27. D. D. C. Bradley, M. Grell, X. Long, H. Mellor, A. W. Grice, M. Inbasekaran and E. P. Woo, *Proc. SPIE* **1997**, *3145*, 254−259.

28. M. Grell, D. D. C. Bradley, G. Ungar, J. Hill and K. S. Whitehead, *Macromolecules* **1999**, *32*, 5810−5817.

29. C. Wu and J. McNeill, *Langmuir* **2008**, *24*, 5855−5861.

30. J. M. Behrendt, Y. Wang, H. Willcock, L. Wall, M. C. McCairn, R. K. O'Reilly and M. L. Turner, *Polym. Chem.* **2013**, *4*, 1333−1336.

31. B. Liu, T. Li, H. Zhang, T. Ma, J. Ren, B. Liu, B. Liu, J. Lin, M. Yu, L. Xie and D. Lu, *J. Phys. Chem. C* **2018**, *122*, 14814−14826.

32. W. C. Tsoi, A. Charas, A. J. Cadby, G. Khalil, A. M. Adawi, A. Iraqi, B. Hunt, J. Morgado and D. G. Lidzey, *Adv. Funct. Mater.* **2008**, *18*, 600−606.

33. A. K. Bansal, A. Ruseckas, P. E. Shaw and I. D. W. Samuel, *J. Phys. Chem. C* **2010**, *114*, 17864−17867.

34. H. J. Eggimann, F. L. Le Roux and L. M. Herz, *J. Phys. Chem. Lett.* **2019**, *10*,

1729−1736.

35. A. Perevedentsev, N. Chander, J. S. Kim and D. D. C. Bradley, *J. Polym. Sci., Part B: Polym. Phys.* **2016**, *54*, 1995−2006.

36. Q. Zhang, L. Chi, G. Hai, Y. Fang, X. Li, R. Xia, W. Huang and E. Gu, *Molecules* **2017**, *22*, 315.

37. M. Ariu, D. G. Lidzey, M. Sims, A. J. Cadby, P. A. Lane and D. D. C. Bradley, *J. Phys.: Condens. Matter* **2002**, *14*, 9975−9986.

38. M. Sims, D. D. C. Bradley, M. Ariu, M. Koeberg, A. Asimakis, M. Grell and D. G. Lidzey, *Adv. Funct. Mater.* **2004**, *14*, 765−781.

Chapter IV

Simultaneous nanofishing and SMS study of single π conjugated polymers: Towards the direct control of conformation and fluorescence properties

4-1. Introduction

4-1-1. Conformation and photophysical properties of π conjugated polymers

As mentioned in Chapter I, conformation and interchain interactions can affect the photophysical properties of π conjugated polymers. Conformation of π conjugated polymers can be controlled by modifying crystal structure of a bulk neat film or by dispersing the π conjugated polymer in a liquid crystal [1-2]. In addition, intrachain interactions, such as hydrogen-bonding and non-bonding interactions, can restrict freedom of conformation. It has been reported that strategically designed π-conjugated polymers can have a large potential barrier to the twist of its backbone due to intrachain interactions, resulting in improved charge carrier mobility [3-4]. Compared to a twisted conformation, planar conformation not only has a longer effective conjugation length, but can also be stacked tightly, leading to the improved charge carrier mobility. Such results indicate that conformation is one of the most important factors in photoelectric properties, but at the same time that it is difficult to distinguish the effects of conformation and interchain interactions on those properties.

4-1-2. Controlling conformation of single π conjugated polymers

Because single molecule study can avoid the effect of interchain interaction, conformation and fluorescence properties of single π conjugated polymers have been studied extensively, revealing that polymer conformation is highly sensitive to the surrounding environment. For the single molecule studies, samples are generally fabricated by spin-coating from a solution containing ultralow concentration of the π conjugated polymer and 1 ~ 2 wt % of a matrix polymer. As shown in chapter II, conformations significantly depend on the polymer matrices. In addition, the solvent used to disperse the π conjugated polymer and dissolve the matrix also affects the polymer conformation [5]. For example, in MEH-PPV samples prepared from toluene solution the

chains are highly folded (Fig. 4-1 (b)) and energy transfer occurs to the lowest energy site, leading to pronounced blinking (Fig. 4-1 (a)). On the other hand, in MEH-PPV samples prepared from chloroform solution the chains are extended and do not show the blinking behavior (Fig. 4-1 (c,d)).
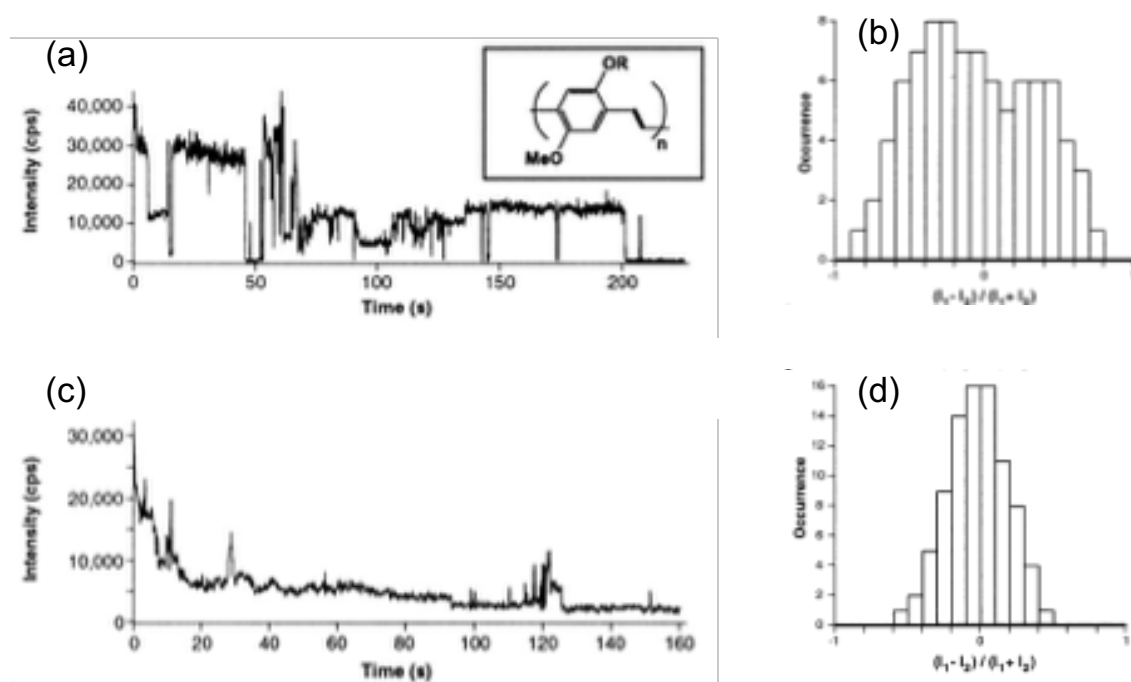

Fig. 4-1 Fluorescence time trace of MEH-PPV prepared from toluene(a), and CHCl$_3$(c), Polarization dependence of MEH-PPV prepared from toluene(b), and CHCl$_3$(d) [5].

Several studies showed that conformation can be controlled also by chemical structure. Polystyrene can be incorporated into polythiophene as a large-size side chain to suppress intrachain interactions. As a result, the polymer main chain takes on an expanded conformation in polystyrene compared to a polythiophene without the large side chains [6]. Although regioregular P3HT takes highly ordered conformation, regiorandom P3HT adopts a wide variety of conformations (Fig. 4-2) [7-8].
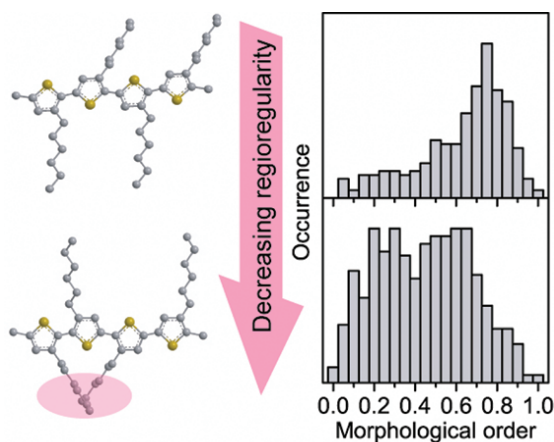
Fig. 4-2 Difference between polarization dependence of regioregular P3HT (above) and regiorandom P3HT (below) [7].

On the other hand, it is difficult to obtain information on the dynamics of conformation changes by single molecule studies in polymer matrix because the matrix itself restricts freedom of conformation. Several research groups succeeded in performing solution-based SMS of π conjugated polymers and reported dynamic changes of conformation and related fluorescence properties. In solution, polymer chains physically adsorb on a substrate or diffuse freely (Fig. 4-3 (a)). Although diffusing polymer chains show no blinking, adsorbed chains show blinking and fast photobleaching (Fig. 4-3 (b,c)). This result indicates that the degree of conformation freedom is capable of affecting the photophysical properties [9].
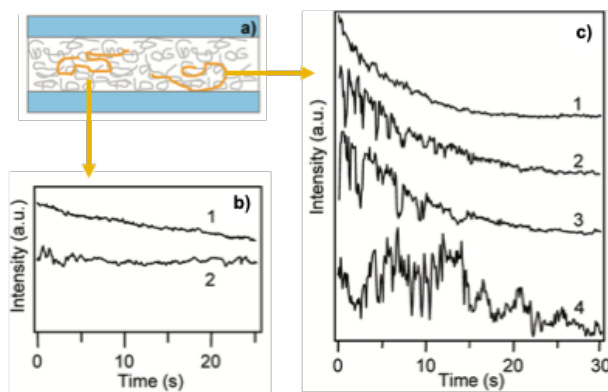
Fig. 4-3 Schematics of freely diffusing and adsorbed polymer chains (orange) in solution (a), fluorescence time trace of diffusing (b) and adsorbed polymer chain (c). [9]

In order to suppress diffusion of the polymer chain, one end of the π conjugated polymer chain can be functionalized and anchored to a substrate. Wide variety of blinking and photobleaching behavior were observed and suppressed by addition of oxygen scavenger in such samples [10]. Other studies show that expanded and compact conformations can be reversibly changed by switching between good and poor solvent [11]. Annealing a polymer film is known to induce polymer chain motion and improve film morphology. Solvent vapor annealing (SVA) is an effective way to anneal polymer films because it is easy to perform and does not promote undesirable chemical reactions such as oxidation.

In polyfluorenes, the formation mechanism of β-phase in polyfluorene has not fully understood. Our group measured fluorescence from single PFO chains with different molecular weight during the SVA process [12]. PFO single chains showed fluorescence switching between glass phase and β-phase (Fig. 4-4) and large distribution of coherence lengths of the exciton. In addition, low molecular weight chains show much faster β-phase formation. These results are important for understanding the process of β-phase conformation in PF films. The above mentioned experiments in solution focus on dynamics of conformation and related fluorescence properties and show that conformation is indirectly controlled by external forces such as solvent vapor or solvent quality.
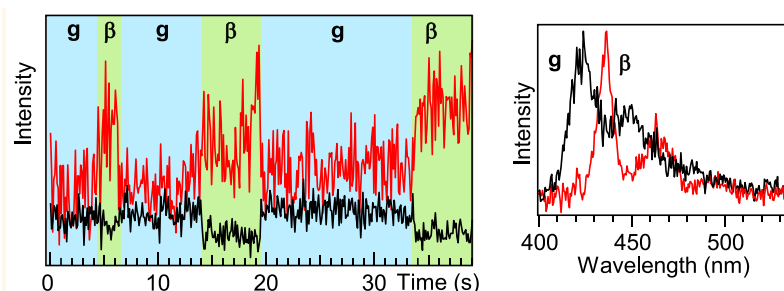
Fig. 4-4 Left panel: an example of fluorescence time trace of single PFO chain, the emission from glass phase (black) and β-phase (red) are separated by dichroic mirror. Right panel: fluorescence spectra of glass and β-phase. [12]

4-1-3. Strategy and purpose

Given the limitations of all the above approaches, the ultimate way of controlling conformation of a π conjugated polymer is to directly manipulate the polymer chain. We propose one such ultimate way to control the conformation of π conjugated polymers, a combination of the SMS technique with a so called nanofishing. Nanofishing is a technique in which a single polymer chain whose ends are chemically connected to a substrate and an AFM cantilever, respectively, is mechanically stretched. Statistical mechanical properties of single polymer chains are obtained by measuring force-extension curves [13]. Therefore, the nanofishing technique can directly control the chain conformation.

One aspect of folded conformation of π conjugated polymers is the possible presence of intrachain interactions between different conjugated segments. Upon light irradiation, the interaction can take the form of excitonic coupling which is responsible for the appearance of ground-state (H- or J-) aggregates as well as excimers. In 1930s, excitonic coupling was first observed by Scheibe et al. and Jelly as an unusual phenomenon of bathochromic shift of absorption spectrum of pseudo isocyanine (PIC) dyes in solution [14-16]. The features of the new spectral band are its narrow shape, very high absorption coefficient and strong fluorescence. On the other hand, other PIC dyes aggregates showed

hypsochromically shifted absorption and weak or no fluorescence [17]. These aggregates were later termed as J-aggregate (J originating from Jelly) and H-aggregate (H originating from hypsochromic), respectively. Kasha and coworkers proposed excitonic coupling theory which explains the spectral shift of aggregates as transition dipole interaction using point dipole approximation in 1960s [18-19]. This theory showed relation between geometrical arrangement of molecules and spectral blue and red shift. Recent studies have developed this theory and described experimentally obtained spectral shift of various organic chromophores [20-25]. However, excitonic coupling energy has never been directly measured. A recent theoretical study of force-extension curves of two PDI molecules connected by an alkyl spacer and illuminated by light in resonance with the PDI absorption [26] showed that the exciton coupling energy between the two PDIs is strong enough to be measurable as force by AFM using the nanofishing technique. This study showed that combining SMS and nanofishing technique is not only a great way to control conformation but also probably the only way to directly measure exciton coupling energy and reveal electronic states of chromophores.

Polyfluorenes have been widely studied in various fields, from synthesis to optoelectrical properties, and many end-capped polyfluorenes have been synthesized [27-33]. Also, as mentioned previously, polyfluorenes are known to take unique conformations, such as glass phase or β-phase. Further, we have shown in chapter II that exciton coupling is one of the possible causes of the appearance of the g-band in PFs. Therefore, polyfluorene is one of the suitable materials for experiments combining SMS and nanofishing. The purpose of this study is to simultaneously measure fluorescence and force-extension curves from single PFO chains and clarify the relationship between conformation and fluorescence properties and the exciton coupling energy.

As a strategy, amino-terminated PFO is synthesized by chain-growth polymerization [31-34]. According to previous research, amino-terminated PFO can be synthesized by reduction of nitro-terminated PFO [35]. To perform nanofishing experiment, the surface of quartz substrate and AFM tip is functionalized by epoxy group which react with amine group. By simultaneously measuring force curve and fluorescence of PFO chains, we can investigate conformational change such deformation of excitonic coupling detected as

force peak and reveal correlation between conformational change and fluorescence properties (Fig. 4-5).
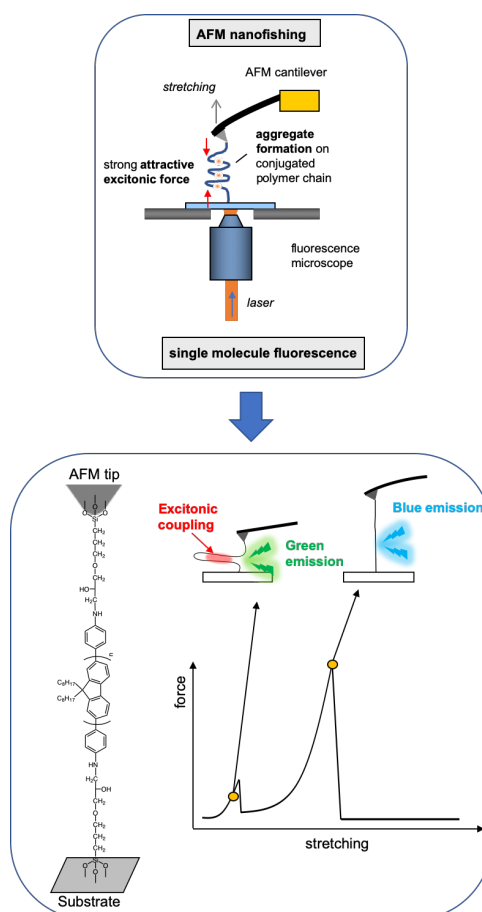

Fig. 4-5 Upper panel: Schematic illustration of experiment combining nanofishing and single molecules spectroscopy. Lower panel: Illustration of nanofishing of amino-terminated PFO chain (left). Expected experimental data showing that excitonic coupling is measured as force peak during nanofishing and schematic diagram of conformational and emission color change of polymer chain during nanofishing (right).

4-2. Experimental section

4-2-1. Synthesis of 2-(7-bromo-9,9-dioctyl-9H-fluoren-2-yl)-4,4,5,5-tetra-methyl-1,3,2-dioxaborolane
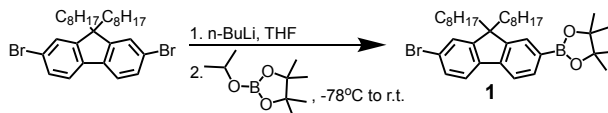
Under N_2 atmosphere, 2,7-dibromo-9,9-dioctyl-9H-fluorene (2.02 g, 3.7 mmol) was dissolved in 20 mL THF and cooled to -78 °C. BuLi (2.4 mL, 6.0 mmol) was added dropwise to the solution and stirred for 1 hour. Then, 2-isopropoxy-4,4,5,5-tetramethyl-1,3,2-dioxaborolane (0.8 mL, 3.9 mmol) was added dropwise, the reaction mixture was heated to room temperature and kept for 24 hours. Subsequently, the organic layer was washed with saturated NH_4Cl aqueous solution and dried with $MgSO_4$. The solvent was evaporated and the crude product was purified by column chromatography using a mixed solvent of hexane/CH_2Cl_2 (v/v = 4/1). 0.90 g colorless oil (**1**) was obtained as the product with yield of 41 %.

^{1}H-NMR (CDCl$_3$, 300 MHz): 7.43-7.81 (m, 6H), 1.85-2.02 (m, 4H), 1.39 (s, 12H), 0.94-1.28 (m, 20H), 0.82 (t, J = 6.8 Hz, 6H), 0.49-0.62 (m, 4H). MS: m/z 594.50 (calc. 595.495).

4-2-2. Synthesis of nitro-terminated PFO (NO₂-PFO-NO₂)
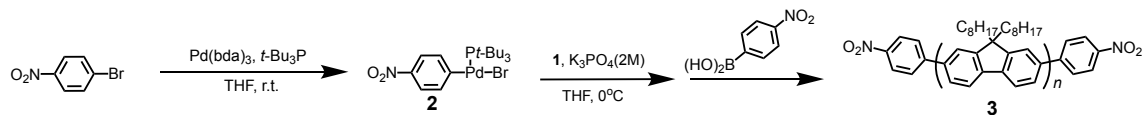
Pd(dba)₂ (10 mg, 0.01 mmol), tert-Bu₃P (26 mg, 0.06 mmol) and 1-bromo-4-nitrobenzene (18 mg, 0.045 mmol) were dissolved in THF. The solution was stirred for 2 h in N₂ and used as an initiator (**2**). In another flask, **1** (0.28 g, 0.47 mmol) was dissolved in THF (5.4 mL) and 2 M aqueous solution of K₃PO₄ (0.5 mL) in N₂. Initiator solution was added to this mixture at 0 ᵒC to initiate polymerization. After 1 h, 4-nitrophenylboronic acid (82.4 mg, 0.49 mmol) was added to the reaction mixture for end capping. The product was extracted 3 times with CH₂Cl₂. Extracted organic layers were combined, washed with brine and dried with Na₂SO₄. Na₂SO₄ was removed by filtration and the filtrate was evaporated under reduced pressure. The residue was dissolved in a minimum amount of THF and added dropwise to methanol with stirring. The precipitate was collected by filtration (0.1 g, yield: 36 %). The product (**3**) was further purified by HPLC (0.05 g, yield: 18 %).

^{1}H-NMR (CDCl₃, 400 MHz): 0.81 (m, 10H), 1.14 (m, 20H), 2.12 (br, 4H), 7.68-7.70 (m, 4H), 7.83-7.85 (d, 2H). GPC: M_n = 27650, M_w / M_n = 1.61.

4-2-3. Synthesis of amino-terminated PFO (NH$_2$-PFO-NH$_2$)
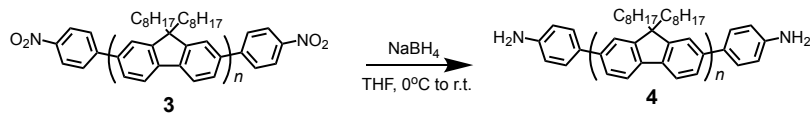
Compound **3** (20 mg, 0.7 μmol) was dissolved in THF and cooled to 0 °C. Excessive amount of NaBH$_4$ was added to this solution. Then, the reaction mixture was heated to room temperature and stirred for 6 h. After filtration, organic layer was extracted with CH$_2$Cl$_2$ and dried with Na$_2$SO$_4$. The organic solvent was removed under reduced pressure and the residue was purified by the reprecipitation method with CH$_2$Cl$_2$/methanol (15 mg, yield: 75 %).

4-2-4. Functionalization of quartz substrate

First, quartz substrate was sonicated two times in ethanol for 20 min and transferred into alkaline solution (NH$_4$OH/H$_2$O$_2$/H$_2$O, 1:1:5 v/v) for 1 h. To obtain -OH rich surface, quartz substrate was soaked in piranha solution (H$_2$SO$_4$/H$_2$O$_2$, 7:3 v/v) for 30 minutes. The piranha solution was then completely removed by rinsing with water. To functionalize the surface with epoxy groups, the cleaned quartz substrate was incubated overnight in 3-glycidyloxypropyltrimethoxysilane (TCI) and thoroughly rinsed with ethanol and toluene.

4-2-5. Immobilization of NH$_2$-PFO-NH$_2$ on a quartz substrate

10^{-6} ~ 10^{-8} M of amino terminated PFO (NH$_2$-PFO-NH$_2$) in THF solution was dropped onto the functionalized substrate. After THF was completely dried, the substrate was rinsed with toluene to remove the unreacted polymer chains and dried with N$_2$ gas.

4-2-6. Functionalization of AFM cantilever

AFM cantilever was functionalized in almost the same way as the quartz substrate. First, the cantilever was immersed in ethanol for 1h and transferred into alkaline solution ($NH_4OH/H_2O_2/H_2O$, 1:1:5 v/v) for 1 h. Then, the cantilever was soaked in piranha solution (H_2SO_4/H_2O_2, 7:3 v/v) for 30 minutes and thoroughly rinsed with water. Finally, the cleaned cantilever was incubated overnight in 3-Glycidyloxypropyltrimethoxysilane (TCI) and thoroughly rinsed with ethanol and toluene.

4-2-7. Combined confocal and atomic force microscopic setup

The single molecule and AFM measurements were carried out using a home-built setup that combines an inverted fluorescence microscope (IX 73, Olympus) with an AFM head (MFP-3D-SA, Asylum Research). The AFM cantilever used was HQ:CSC38/Al BS (MikroMasch). Nanofishing experiments were performed in toluene. The sample was excited with a 375 nm laser (LDH-D-C375, Pico Quant). Fluorescence from the sample was collected by an oil immersion objective lens (UplanFLN 100×, N.A. 1.3, Olympus) and passed through a dichroic mirror (Dichro 375, Chroma) and a long-pass filter (LP 377, Edmund). The objective lens was mounted on a three-axis piezo stage (PS3L60-030U, NC3311, Nanocontrol) to accurately align its center position with respect to the AFM tip. The fluorescence signal was detected by an electron-multiplying charge-coupled device (EMCCD) camera (iXon, Andor Technology) equipped with an imaging spectrograph (CLP-50LD, Bunkou Keiki) to measure fluorescence spectra. The integration time and gain of EMCCD were 0.2 s and 300, respectively.

4-2-8. Theoretical calculation of excitonic coupling between two PFO segments

Excitonic coupling J is calculated following the same way as reported recently for simulation of nanofishing of two PDI molecules [26]. The coupling is composed of long-range Coulombic interaction and of short range interaction related to overlap of molecular orbitals of two molecules. In this study, only Coulombic interaction is calculated as the interaction between atomic transition charges (ATCs). ATCs for p-th atom in the k-th excited state was expressed as

$$q_p^k = \sqrt{2} \sum_b^{N_{AO,p}} \sum_c^{N_{AO}} \sum_j^{unocc} \sum_i^{occ} A_{ij} C_i^{pb} C_j^c S_{bc} \tag{4-1}$$

where i is the index of occupied molecular orbital (MO), j is the index of virtual unoccupied MOs, b and c are indexes of atomic orbital basis function, N_{AO} is the total number of atomic orbitals, $N_{AO,p}$ is the total number of atomic orbitals of p-th atom, A_{ij} is the CI coefficient, C_i^{pb} is the atomic orbital coefficient b of molecular orbital i of p-th atom, C_j^c is the atomic orbital coefficient b of MO j and S_{bc} is the overlap matrix between the AO basis functions b and c. The excitonic coupling J_c was calculated using the equation (2)

$$J_c = J_c^{IJ} = \sum_{IJ} \frac{q_i \, q_j}{4 \pi \varepsilon_0 r_{ij}} \tag{4-2}$$

where r_{ij} is the distance between atom i and j of molecule I and J and ε_0 is the vacuum permittivity. The ATCs of each atom were calculated from isolated fluorene monomer for S_0-S_1 transition using DFT and TD-DFT at B3LYP / 6-31G++(d,p) level. Because the effective conjugation length of PFO is 8 monomer units, we multiplied the calculated J_c between the two fluorenes by 8 [36].

4-3. Results and Discussion

4-3-1. Immobilization of PFO onto substrate surface

In a previous study, the combination of amine group and epoxy group was used for single molecule force measurement of dendronized polymer [37]. Here, in a similar manner, to immobilize amino-terminated PFO onto the substrate surface, the surface of quartz substrate was functionalized with epoxy groups. Samples of three different concentrations of PFO were prepared and the presence of reacted PFO chains was confirmed by measuring the density of light emitting spots in fluorescence images in toluene. With respect to the samples prepared from the 10^{-6} and 10^{-7} M PFO solutions, fluorescence signal covers the whole image area with spatial variations of fluorescence intensity, indicating that the PFO chains are attached evenly to the whole surface of the quartz substrate (Fig. 4-6 (a-b)). Fluorescence image of the sample prepared from 10^{-8} M showed individual emitting spots with equal fluorescence intensity and these can be attributed to single PFO chains (Fig. 4-6 (c)). The higher concentration sample is suitable for nanofishing study because the collision of amino group at one end of the PFO chain with the epoxy group of AFM cantilever surface is required, and higher concentration increases the probability of such collision. On the other hand, single molecule study requires low density of light emitting spots separated by distances larger that the diffraction limit which is on the order of few hundreds nm. Thus, there is a trade-off between suitable concentrations of PFO chain for nanofishing experiments and for single molecule experiments. Therefore, the samples prepared from the 10^{-6} M and 10^{-8} M solutions are suitable for the nanofishing and the single molecule experiments, respectively. Fluorescence spectra of single PFO chains reacted with the substrate in toluene are shown in Fig. 4-7. Sigle PFO chains showed fluorescence with vibronic structure and peak wavelengths around 415 nm, 445 and 475 nm. These features can be attributed to emission of glassy phase PFO in solution. These results confirm that amino-terminated PFO chains are properly immobilized to the surface of quartz substrate by the amine and epoxy groups reaction.
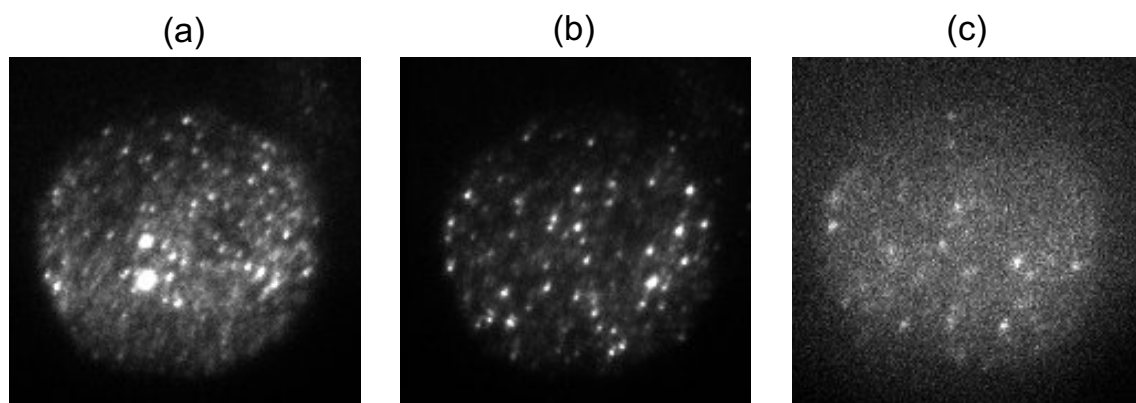
Fig. 4-6 Fluorescence images of immobilized PFO in toluene prepared from THF solution with different concentration, (a) 10^{-6} M, (b) 10^{-7} M, (c) 10^{-8} M.
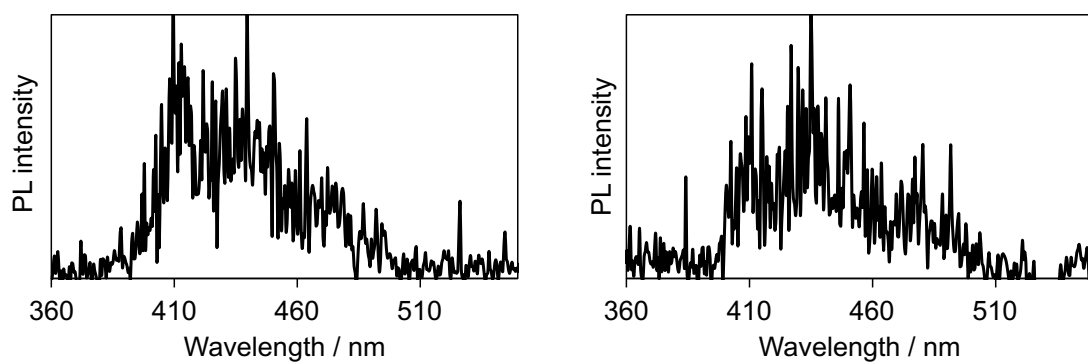

Fig. 4-7 Typical fluorescence spectra of fixed PFO chains in toluene

4-3-2. Nanofishing of single PFO chains in toluene

Typical examples of force-extension curves of single PFO chains in toluene are shown in Fig. 4-8. First, the AFM cantilever contacts the surface of the quartz substrate, and the amine group at one end of the PFO reacts with the epoxy group on the surface of the quartz substrate. Then, the AFM cantilever starts separating from the substrate, forcing the polymer chain to stretch until the chemical bond is broken. The peak force corresponding to the breaking of chemical bonds generally exceeds few hundreds pN [13, 37]. The force-extension curves in Fig. 4-8 show a single force peak with a magnitude of more than few hundreds pN, indicating that the amino-terminated PFO chains are correctly picked up by the functionalized AFM cantilever and extended to full length before the bond breakage. The extension length at the force peak is termed rupture length and corresponds to the length of fully stretched polymer chain. The rupture length has been measured for 51 single PFO chains and the values have been summarized in a histogram shown in Fig. 4-9. The molecular weight of the synthesized amino-terminated PFO was measured by GPC and a value of 27650 g/mol was obtained. From this value, the length of the polymer chain can be estimated as about 60 nm by using quantum chemical calculation to obtain the size of fluorene monomer and the bond length between two fluorenes. In the histogram in Fig. 4-9, the rupture length is distributed between 30 and 160 nm with an average value of 80.7 nm, which is longer than the 60 nm obtained from the GPC. One reason for the rupture length distribution is a distribution of molecular weight, characterized by an estimated PDI of 1.61. Further, the larger average rupture length value indicates that longer polymer chains are more easily picked up by the AFM cantilever. Amine group at the one end of the polymer chain can diffuse in a hemisphere whose diameter corresponds to chain length. When the AFM tip enters this hemisphere, the chain-end amine group can react with epoxy groups on the surface of the AFM tip and the polymer chain will be picked up. This consideration indicates that longer polymer chain is preferentially picked up because the area of the hemisphere increases as the polymer chain becomes longer.

116

4-3-3. The effect of excitation light on nanofishing of PFO chains in toluene

Next, in order to examine the effect of excitonic coupling on the unfolding of single PFO chains, we performed the nanofishing experiment in toluene in the presence of continuous excitation light. Fig. 4-10 shows examples of the force-extension curves of PFO chains exited by the 375 nm laser with 14.2 Wcm^{-2}. As the curves in the Fig. 4-10 show, there is one (or a few) additional small force peaks appearing in a range of extensions before the onset of the main force peak (which is attributed to the stretching of the chain). These small observed force peaks appear only under photoirradiation and their magnitude is less than 150 pN. We have verified this observation by measuring 56 single PFO chains under illumination and comparing with 51 single chains stretched in dark. The histogram of the magnitude of these small force peaks is shown in Fig. 4-11 (a). The average force obtained from the histogram is 47 ± 2 pN. In a previous theoretical study, exciton coupling between two PDI molecules was calculated and used to simulate a force peak in an AFM force experiment, yielding a predicted theoretical value of $50 \sim 100$ pN [26]. The small force peaks observed only under photoirradiation are of similar order of magnitude, and point can be attributed to the intrachain exciton coupling of PFO chain.

To further confirm the light-induced origin of the small force peaks, we performed the same experiment with different irradiation intensity. Fig. 4-11 (b) shows a histogram of the magnitude of the small force peaks measured on 40 single PFO chains with excitation intensity reduced to about 40 % of the first experiment. The average force obtained from the histogram is 29 ± 2 pN, which corresponds to 61% of the value of 47 pN obtained above. To analyze this result, we examine the details of the irradiation and absorption processes. In the experiment, a pulsed laser was used for excitation, and its repetition rate was 80 MHz. A laser pulse of 20 ps duration is thus irradiated on the sample at 12.5 ns intervals. Because the exciton lifetime of PFO is known to be $0.3 \sim 5.1$ ns (Chapter II), the PFO chain is not in the excited state all the time during the nanofishing experiment. Therefore, the number of excitations of the PFO chain is important. From these considerations, the force should be proportional to the excitation intensity, but the

experimental results showed a weak than linear dependence on the excitation intensity. Under the lower 40 % excitation condition, force of 18.5 pN would correspond to 40 % of 47 pN. However, since the noise of the force curve can be as large as about 10 pN, the smaller force peaks can be lost in the noise and only relatively larger peaks of the distribution could actually be measured. This is also reflected in the skewed shape of the histogram in Fig. 4-11 (b). Therefore, while we unambiguously verified the light-induced nature of the small force peaks, for the discussion of the excitonic coupling the force peaks measured at higher excitation intensities seem to be more reliable.
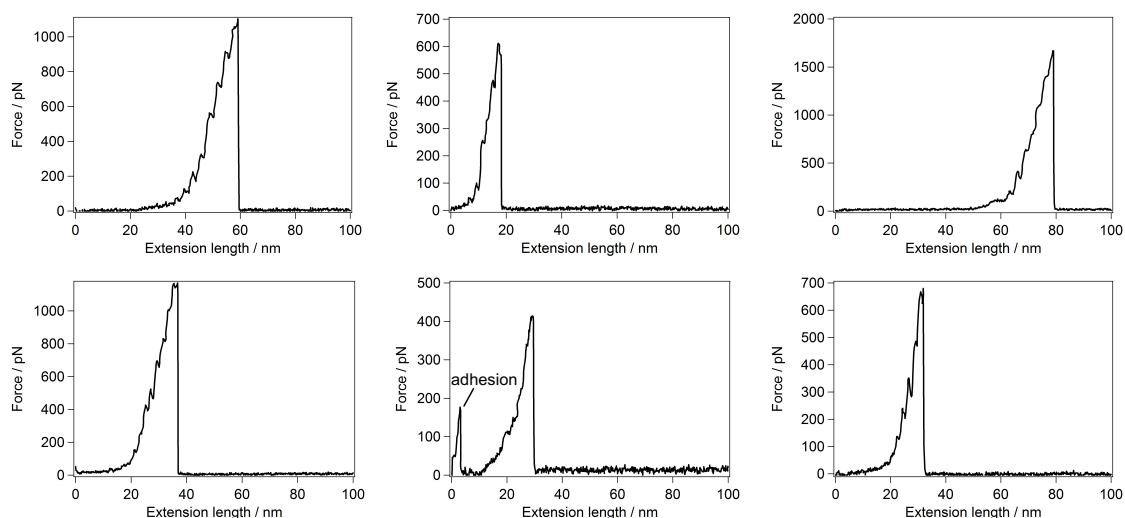
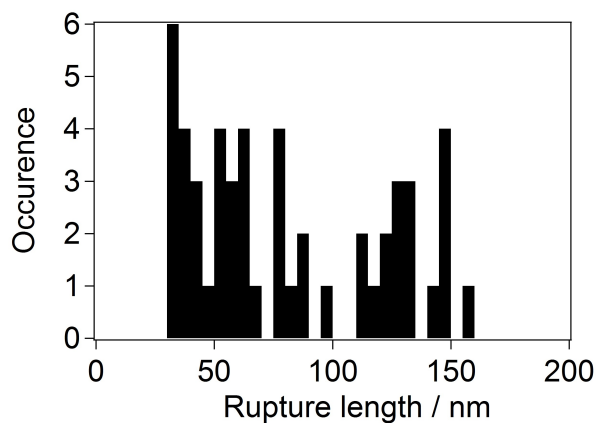Fig. 4-8 Typical force-extension curve of PFO single chain in toluene

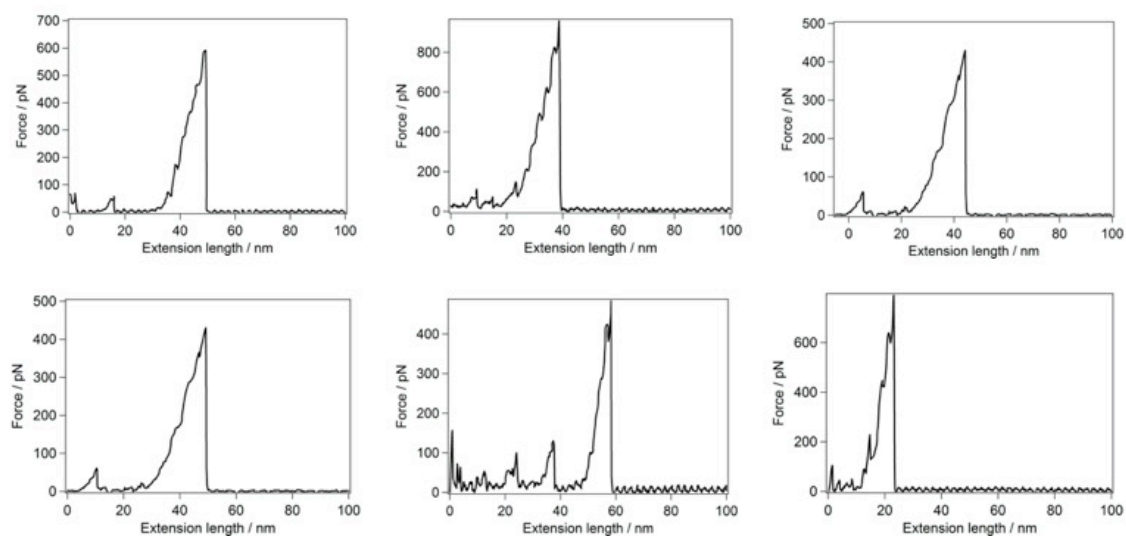Fig. 4-9 Histogram of rupture length of PFO in toluene

Fig. 4-10 Typical force-extension curves with small force peak of PFO single chain in toluene under photoirradiation. Excitation intensity: 14.2 W / cm^2
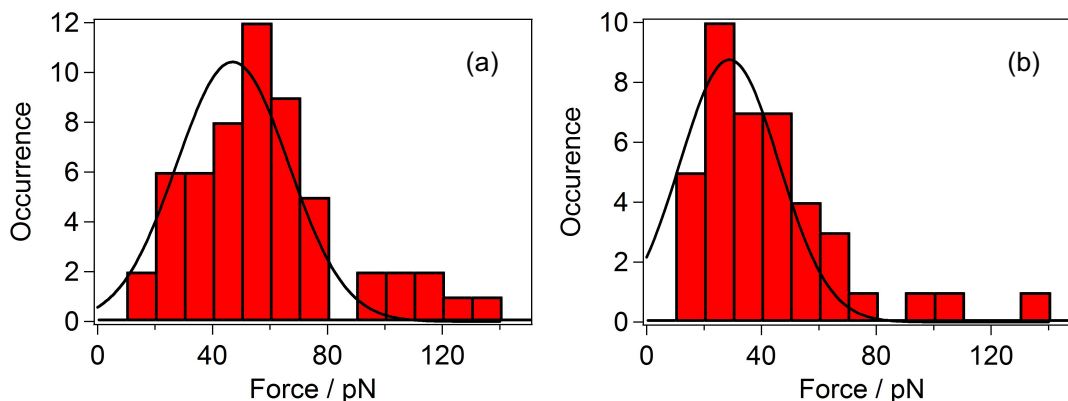
Fig. 4-11 Histogram of small unfolding force observed under photoirradiation with different excitation intensity. (a) 14.2 W/cm², (b) 5.6 W/cm²

4-3-4. Analysis of the exciton coupling energy between PFO segments

In the following, we analyze the data based on the assumption that the weak force peaks appearing only under illumination are caused by excitonic interactions between neighboring conjugated segments on a folded PFO chain. To obtain excitonic coupling energy (J) from the force-extension curves, we integrated the area under the small force peaks because energy is simply calculated by integrating the applied force along displacement as work (N・m). We note that the area of the force curve corresponds to the change of free energy including the difference of potential energy and entropy which can cause errors for estimating exciton coupling energy. Histogram of J obtained for the stronger illumination of 14.2 W/cm² on 56 single PFO chains is shown in Fig. 4-12. The mean excitonic coupling energy obtained by Gaussian fitting of the histogram is 0.54 ± 0.08 eV. We note that this value is underestimated because the PFO molecule is not in the excited state all the time. An average number of photons absorbed by a PFO chain during irradiation with a single laser pulse (N_{phot}) was calculated from the average excitation intensity, laser repetition rate, pulse width and absorption cross section. The obtained value was $N_{phot} = 1.61$ photon per pulse per chain. As mentioned above, with the repetition rate of 80 MHz, laser pulses arrive at 12.5 ns intervals. The mean time for which a PFO

120

chain stays in the excited state (T) during the 12.5 s was calculated by multiplying the exciton lifetime with N_{phot}. Even though this approach is not strictly correct, it simplifies the estimation of the coupling energy. In Chapter II, excited state of PFO in PMMA was shown to decay with lifetime components of 0.34, 1.4 and 5.1 ns, respectively, corresponding to monomer blue emission, green emissive H-aggregate or charge transfer like aggregate. The mean corresponding times that the chain stays in the excited state are thus $T_{5.1ns} = 5.1$ ns $\times 1.61 = 8.21$ ns, $T_{1.4ns} = 1.4$ ns $\times 1.61 = 2.25$ ns and $T_{0.34ns} = 0.34$ ns $\times 1.61 = 0.55$ ns. Next, we calculated the ratio (R) between these mean times and the laser pulse interval of 12.5 ns, and obtained 0.66, 0.18 and 0.044 for the 5.1 ns, 1.4 ns and 0.34 ns components, respectively. These R values are correction coefficients accounting for the fact that the PFO chain is not in the excited state all the time during the stretching experiment. To obtain the corrected exciton coupling energy, the experimentally obtained values are divided by the factor R result to obtain the coupling energy $J_{5.1ns}$, $J_{1.4ns}$ and $J_{0.34ns}$ of 0.82 eV, 3.0 eV and 12.3 eV, respectively. Generally, fluorescence lifetime depends on dielectric constant of the surrounding environment. Since the nanofishing experiments are performed in toluene, lifetime value of the g-band obtained in PS matrix is more suitable for calculation of the correction factor than the one obtained in PMMA. The excitonic coupling energy $J_{4.5\,ns}$ corrected by lifetime in PS of 4.5 ns was 0.93 eV.
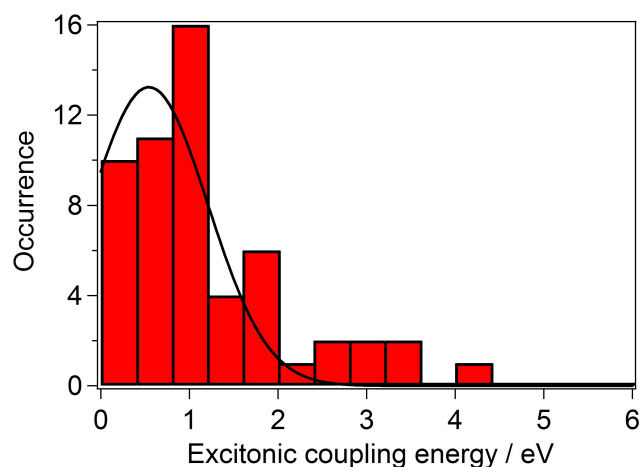

Fig. 4-12 The histogram of exciton coupling energy between PFO segments obtained by integration of the area of small force peak

As seen in Fig. 4-12, there is a wide distribution of J observed. Especially, the values of J above 2 eV are too large compared to spectral changes. The conceivable causes of the wide J distribution are (1) the number of monomer unit contributing to excitonic coupling (N_m), (2) structure of the aggregate, and (3) molecular weight distribution. J depends on the transition dipole moments of interacting conjugated segments. Large transition dipole moments cause strong excitonic coupling. The angle between two transition dipole moments also affects the magnitude of J. It is known that two transition dipoles aligned parallel show strong excitonic coupling, while perpendicularly aligned dipoles show very weak excitonic coupling. Therefore, we can assume that change of the aggregate structure from parallel to perpendicular (Fig. 4-13) is one of the factors behind the appearance of the small force peak during chain extension. If this assumption is correct, contact length (defined as the rupture length of H-aggregate in this study) should be related to the number of monomer units contributing to the excitonic coupling. The contact length was analyzed from the small force peaks and summarized in a histogram in Fig. 4-14. The contact length is distributed between 1.6 nm to 24 nm and the average value of the contact length obtained by Gauss fitting is 4.9 $\pm$ 0.3 nm. This value corresponds to N_m of 6.0 $\pm$ 0.4 monomer units. The conjugation length of glass phase PFO is 8 $\pm$ 1 monomer units. This value is almost same as the experimentally obtained N_m, indicating that two glass phase segments form an H-aggregate. Further, the relationship between excitonic coupling and contact length is shown in Fig. 4-15. There is a weak correlation between the two, but J generally increases in proportion to the contact length. By dividing the coupling energy J by the number of monomers N_m in the contact length, excitonic coupling energy per monomer (J_{mono}) was obtained, and its distribution is shown in histogram in Fig. 4-16. If each aggregate was stacked in the same geometry, there should be no distribution of J_{mono}. However, PFO in toluene showed large variety of J_{mono} (Fig. 4-17), indicating that there is variation of stacking structures in the H-aggregate. The details of the aggregate structure will be discussed later together with the results of theoretical calculations. The above results obtained by the force curve analysis show that both (1) N_m and (2) aggregate structure can affect the values of J. However, these two factors alone are not sufficient to explain the large distribution of J.
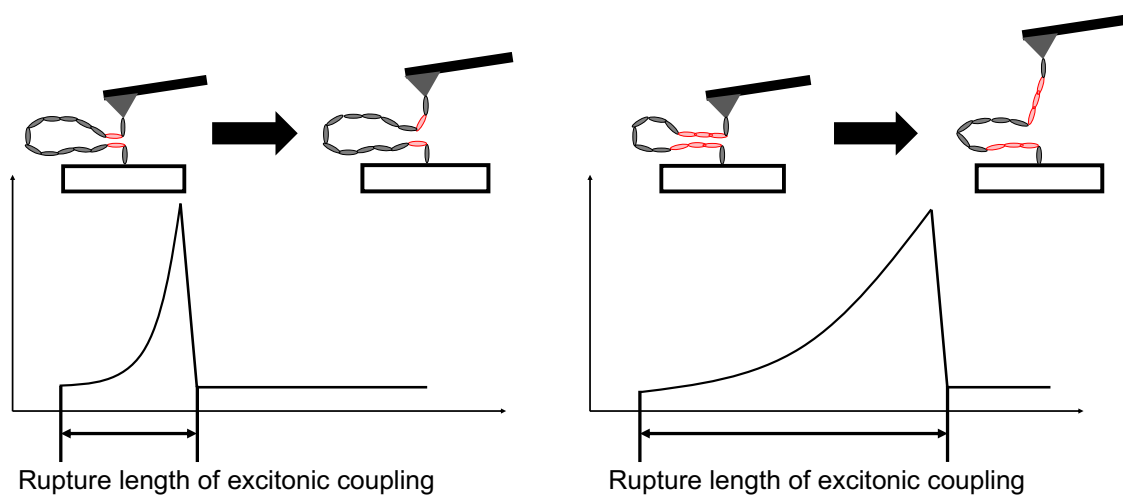
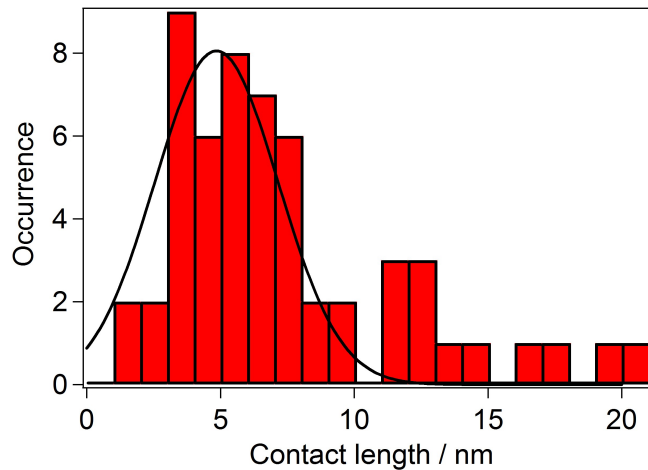Fig. 4-13 Schematic illustration of how aggregate structure affect force curve
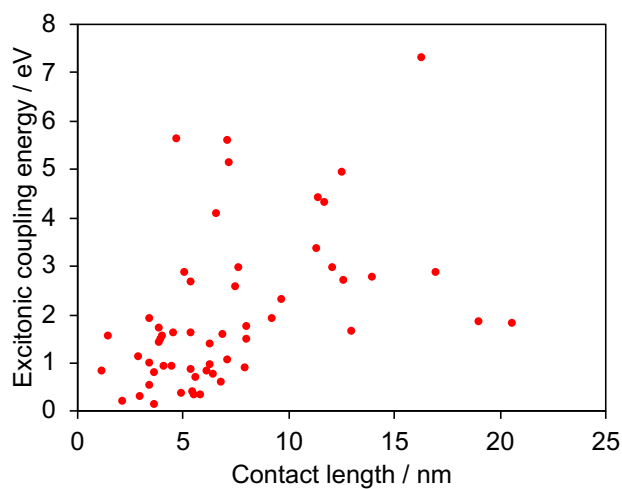

Fig. 4-14 Histogram of contact length

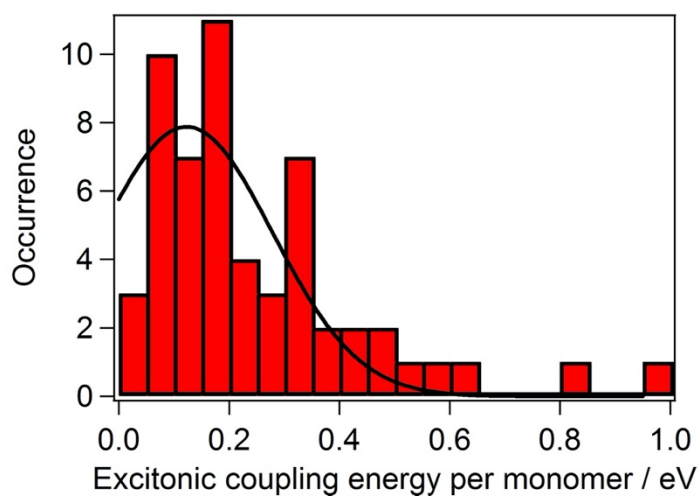Fig. 4-15 Excitonic coupling energy (J) as a function of contact length

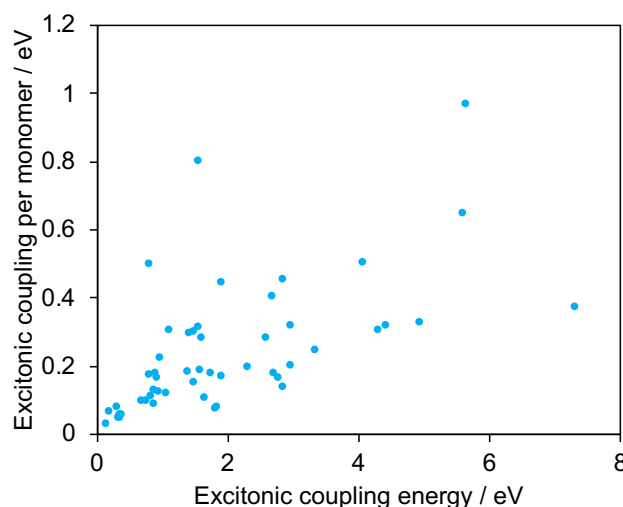Fig. 4-16 Histogram of Excitonic coupling energy per monomer (J_{mono})

Fig. 4-17 Excitonic coupling energy per monomer (J_{mono}) versus total excitonic coupling energy (J)

With respect to the above point (3) molecular weight distribution, higher molecular weight polymer chain has larger absorption cross-section and absorbs more photons during the nanofishing experiment, leading to an apparent increase in J. If molecular weight significantly affected the excitonic coupling, molecular weight characterization result (GPC curve) should coincide with the distribution of J. To analyze the effect of molecular weight on J, the values of J were converted to molecular weight by the following equation,

$$M_{\mathrm{c}} = \frac{J}{J_{\mathrm{ave}}} \times M_{\mathrm{n}} \qquad (4\text{-}3)$$

where M_{c} is converted molecular weight, J_{ave} is the average value of J and M_{n} is number average molecular weight. Histogram of converted molecular weight M_{c} and the GPC curve are shown in Fig. 4-18. The converted M_{c} reproduced the GPC curve well. This result shows that molecular weight distribution is the main causes of J distribution, and that the factors (1) the number of monomer unit and (2) structure of aggregate play minor roles.
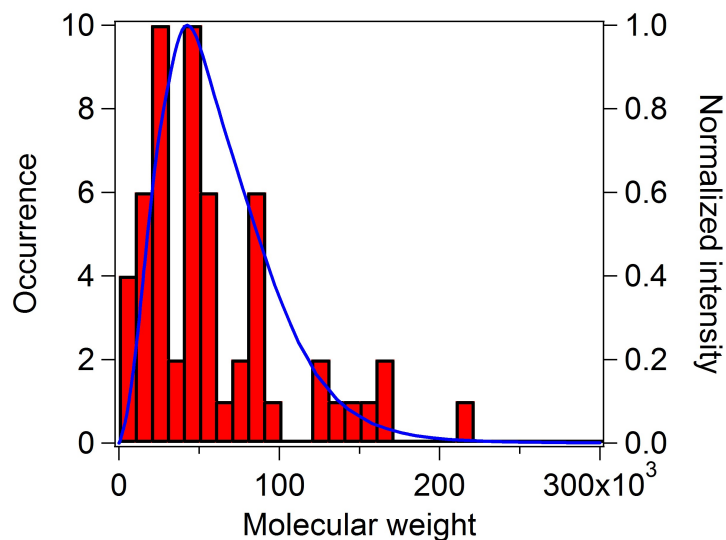
Fig. 4-18 Histogram of molecular weight obtained from J_{ex} and molecular weight distribution obtained by GPC (blue line)

4-3-5. Theoretical analysis of the exciton coupling energy between PFO segments

To examine the appropriateness of the experimentally obtained exciton coupling energy J, we also calculated J of face-to-face stacked fluorene dimer (Fig. 4-19) by the ATC method using quantum chemical calculation. While the ATC method only includes Coulombic contribution to the exciton coupling (J_c), it is known to sufficiently well describe the nature of the exciton coupling between organic molecules [26]. J_c depends strongly on the distance between two PFO segments. As shown in the calculation results in Fig. 4-20, the J_c values corresponding to a reasonable range of intermolecular distances (2.5 Å ~ 10 Å) range from 0.023 eV to 0.34 eV. These results show that the calculated value of J_c is of the same order as the experimentally obtained exciton coupling energy, especially the $J_{4.5ns}$ value. In addition, the energy difference between the blue emission band (420 nm) and the g-band (500 nm ~ 600 nm), which directly represents the exciton coupling (splitting) energy, is 0.47 eV ~ 0.89 eV which is also of the same order as $J_{4.5ns}$.

These results are fully consistent with the previous conclusion that the g-band to a large extent originates from emission of H-aggregates that are characterized by long emission lifetime due to the forbidden nature of the optical transition.
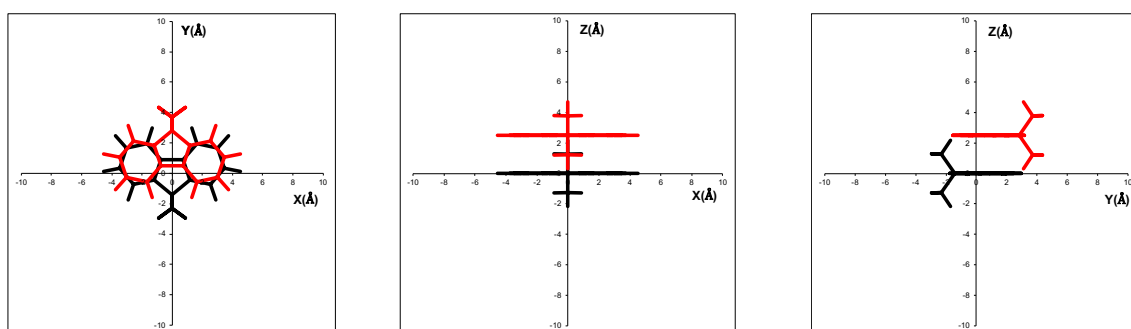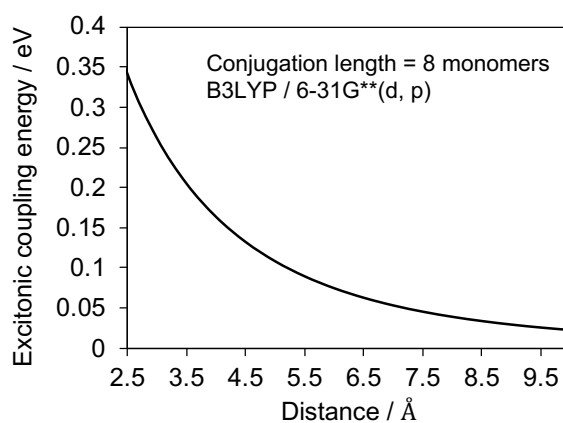

Fig. 4-19 Face-to-face stacked dimer

Fig. 4-20 Distance dependence of exciton coupling J_c in fluorene dimer stacked face-to-face calculated by ATC

Further, to analyze the effect of aggregate structure on the exciton coupling energy, J_c was calculated for various geometries of the fluorene dimer. Shifted aggregate structure (Fig. 4-21a) and rotated aggregate structure (Fig. 4-21b, c) show a slightly reduced excitonic coupling energy J_c of 0.23 eV and 0.16 eV, respectively. These values are still of the same order as $J_{4.5ns}$, indicating that these structural disorders are possible for H-aggregates in toluene. As expected, on the other hand, orthogonally aligned structures (Fig. 4-22a, b) do not form intrachain H-aggregates of PFO single chain because the J_c is too low. Compared to face-to-face stacking, the aggregate structures of Fig. 4-21a, c reduce J_{mono} so that the ratio of J_{mono}/J is small. In the case of Fig. 4-21b, J_{mono}/J is still large because J also decreased due to small contact length (or N_m). We can summarize the effect of aggregate structure of PFO on J using a scheme proposed in Fig. 4-23. With respect to the trends observed in Fig. 4-17, large fractions of intrachain aggregates tends to show low J_{mono} and large J (lower right region), or proportional J_{mono} and J (middle region). Together with the finding that the contact length was about the same as the conjugation length, this result indicates that face-to-face aggregates (Fig. 4-19) and slightly distorted aggregates of the type in Fig. 4-21a, c are the dominant aggregate structures of PFO.
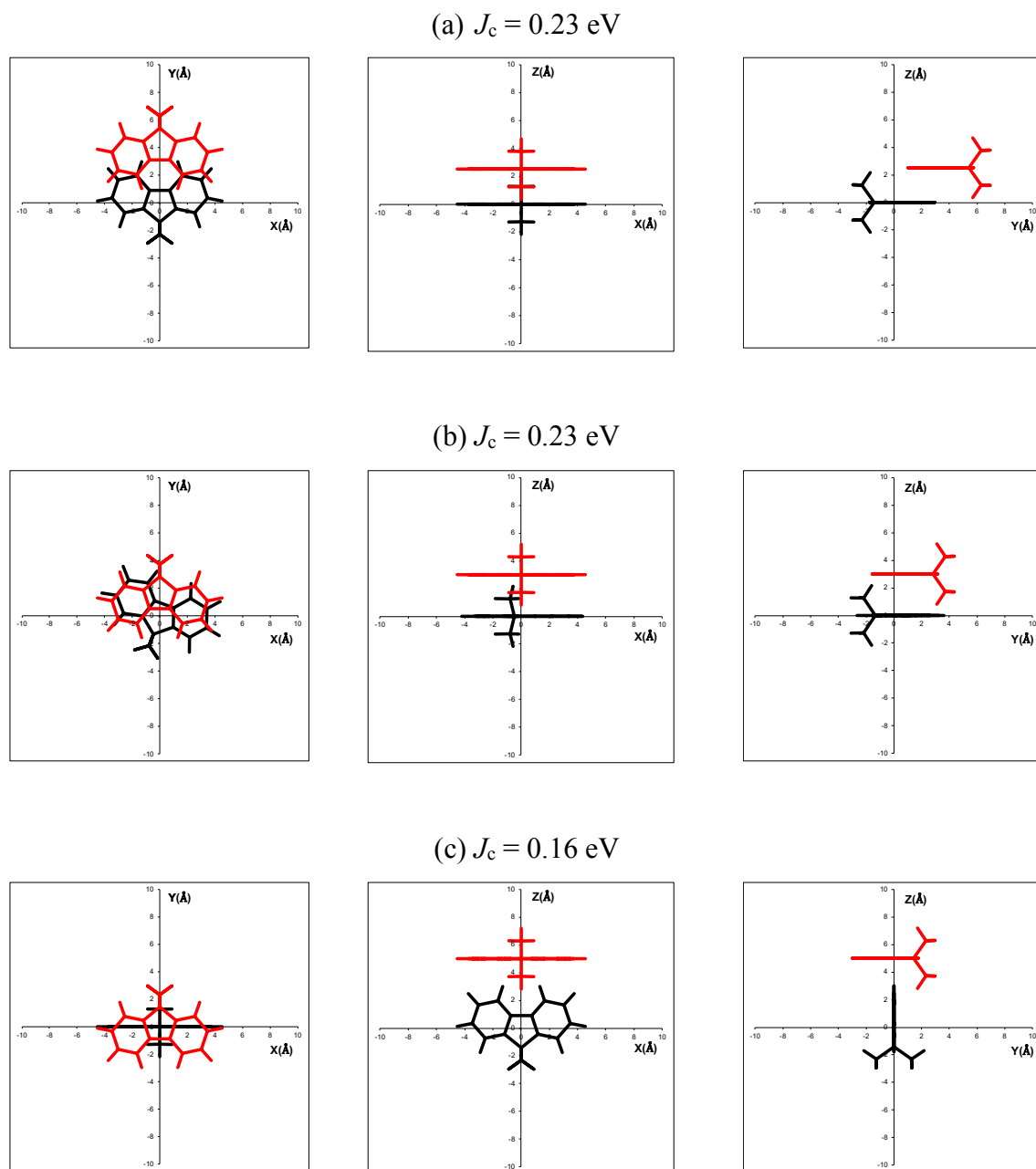
(a) $J_c = 0.23$ eV

(b) $J_c = 0.23$ eV

(c) $J_c = 0.16$ eV

Fig. 4-21 Aggregate structures which show slightly reduced J_c

(a) J_c = 0.02 eV

(b) J_c = 0.001 eV
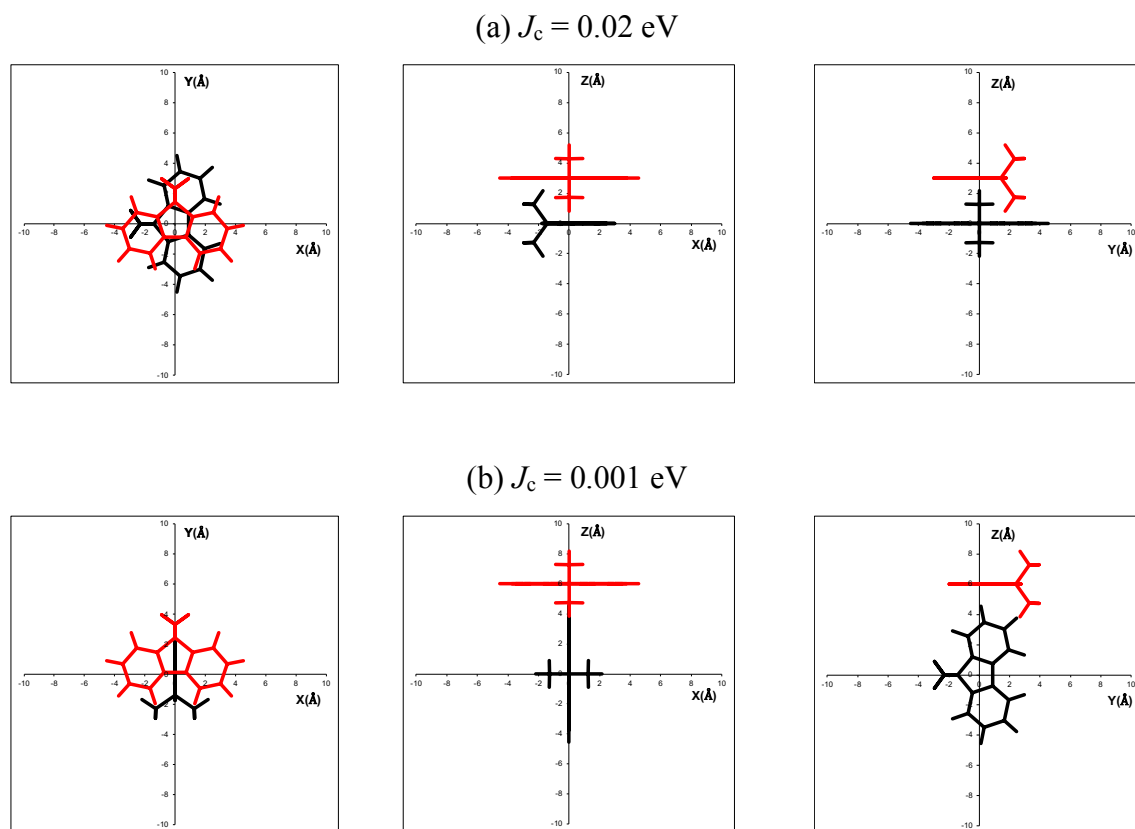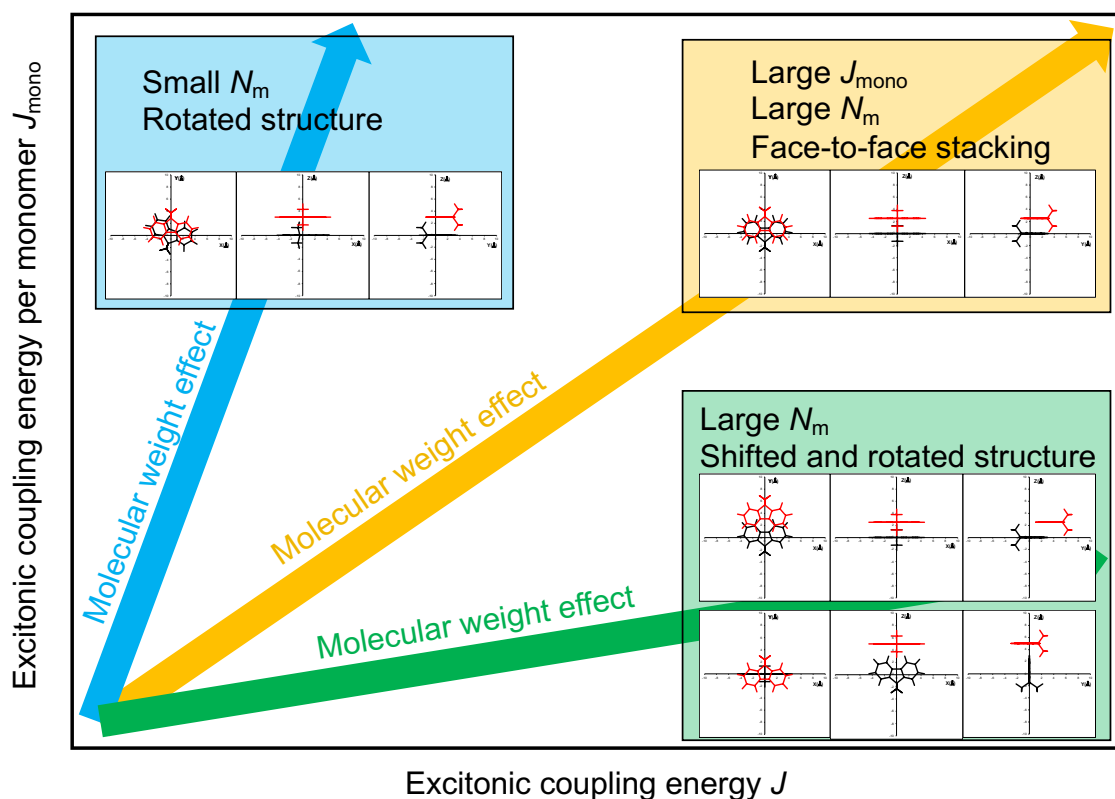
Fig. 4-22 Vertically aligned fluorene dimer

Fig. 4-23 Aggregate structure dependence of J_{mono} vs J

Another way to compare the experimental results with calculated values based on the exciton coupling theory is to use the values of the peak force. The experimentally obtained mean peak force is 47 pN which has to be corrected, in the same way as above, for the finite time that the chain stays in the excited state. Using the factors relevant for the g-band, i.e., 0.66 and 0.18, we obtain mean forces of 71.5 pN and 261 pN, respectively. The theoretical calculation of the peak force (F) uses the expression (4-4) obtained from (4-3)

$$J_c = \frac{1}{2} kx^2 \qquad (4\text{-}4)$$

$$F = kx = \sqrt{2 J_c k} \qquad (4\text{-}5)$$

where x is distance from its equilibrium position, J_c is the Coulombic contribution obtained using the ATC method and k is the spring constant of the AFM cantilever. In this experiment, several cantilevers of the same type were used, and the average value k of their actual spring constants is 0.08 N/m. The calculated peak force values corresponding to a reasonable range of intermolecular distances (2.5 Å ~ 10 Å) are shown in Fig. 4-24 and range from 24 pN to 93.5 pN. The experimental value of 71.5 pN obtained assuming the exciton lifetime of 5.1 ns falls within this range, and even the value of 261 pN is only a factor of 3 different. This result further supports the conclusion that the small force peaks observed during unfolding of the PFO chain are due to intrachain excitonic interactions, and that the nanofishing technique is an excellent tool to directly measure such interactions on single π conjugated polymer chains.
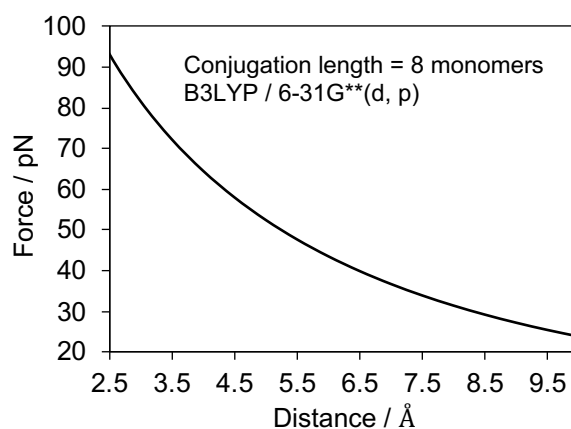

Fig. 4-24 Distance dependence of peak force calculated from J_c

4-3-6. Simultaneous measurement of force curve and fluorescence spectra of single PFO chains in toluene

In the following, we attempted to directly control the conformation od a single PFO chain by the extent of stretching to examine the relationship between the conformation and fluorescence properties. For this purpose, we simultaneously measured the force-extension curve and fluorescence spectrum on the same single PFO chain in toluene. This experiment was conducted using the sample prepared from the 10^{-8} M solution. Such concentration of PFO chains is extremely low to successfully find and pick up a single chain by the AFM cantilever. Therefore, the number of successful attempts to simultaneously obtain the force curve and fluorescence spectrum is limited.

The Fig. 4-25a shows a force-extension curve of a single PFO chain with two small force peaks superimposed on the main force peak. Because the excitation intensity is 40 W/cm^2 which is a factor of 2.8 larger than the intensity used above, the magnitude of the small peaks is about 100 ~ 200 pN which is also larger than the peak force in Fig. 4-10. These small peaks are possibly attributable to exciton coupling.

Simultaneously measured time trace of fluorescence spectra of the single PFO chain (Fig. 4-25b) showed that the PFO chain first exhibited green emission ranging from 500 nm to 600 nm, and that the green emission switched to blue emission just after starting pulling the polymer chain. This observation alone would be consistent with the idea that in the folded conformation in which the PFO chain is compressed by the AFM cantilever, the interchain interactions give rise to formation of H-aggregates and emission of the g-band. After the start of the nanofishing (pulling the cantilever), the aggregates are disrupted as the chain is unfolded by the stretching, and the chain starts emitting in the blue region. However, the timing of this spectral change does not coincide with an appearance of a small force peak. During the stretching of the polymer chain, PFO showed blue emission which is attributed to the glass phase. Although we might expect that β-phase could be formed when the polymer chain is sufficiently stretched, we have not observed any spectral change between the glassy and β-phases during the stretching interval. With the current limited data statistics we cannot make any conclusion about whether the β-phase can be formed by chain stretching, but there is a possibility that such

phase change could be difficult in solution due to the chain Brownian motion.

Although we have not yet obtained a direct link between an excitonic force peak and spectral change on the same polymer chain, the simultaneous nanofishing and fluorescence spectra measurement shows a great potential to directly control chain conformation and get insight into excitonic coupling of intrachain aggregates.
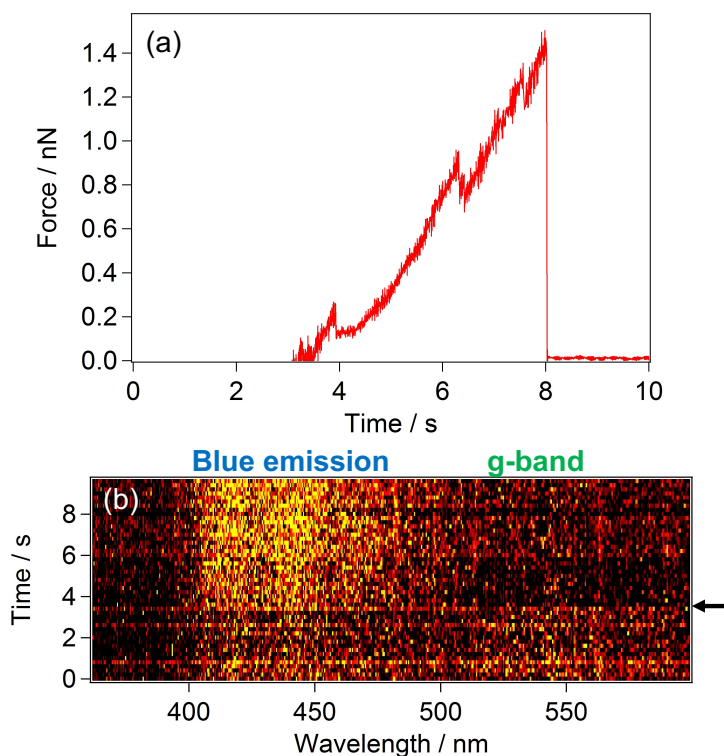

Fig. 4-25 (a) Force curve of PFO chain in toluene and (b) simultaneously measured fluorescence time trace. Black arrow located on right of figure points to the start time of nanofishing. Excitation intensity: 40 W / cm^2

4-4. Conclusion

In conclusion, we have performed simultaneous nanofishing and fluorescence spectroscopy of single PFO chains. Under photoirradiation, small force peaks were detected upon chain stretching and their magnitude depended on excitation intensity. These small force peaks are attributed to intrachain exciton coupling. Exciton coupling energy J between PFO segments estimated from the area of force curve and corrected for excitation conditions and exciton lifetime was on average 0.82 eV. This value is of the same order as theoretically calculated coupling energy. Apart from the effect of exciton coupling, force-extension curves and fluorescence spectra of PFO single chain were simultaneously measured. Spectral changes between blue and green emission regions were observed during the stretching of the chain. However, these changes were uncorrelated with the appearance of the small excitonic force peaks. Also, we have found no spectral switching between glass and β-phase emission during the nanofishing.

These results show that simultaneous nanofishing and fluorescence spectroscopy experiments have great potential for revealing the relationship between conformation and photophysical properties because nanofishing can directly control the chain conformation and it is possible to obtain information about conformational changes form the force curve. Extending this technique can provide new way to study the effect of conformation on optoelectrical properties of π conjugated polymers, leading to develop material design for application of π conjugated polymers in optoelectronic devices.

4-5. Appendix

ATCs of fluorene monomer

Calculated ATCs and xyz coordinates for each atoms of the fluorene monomer shown in Table 4-1.

Table 4-1 Calculated ATCs and xyz coordinates of fluorene

Atom	X	Y	Z	ATCs
C	-0.000005	1.417249	-0.000078	-0.000004
C	-1.181270	0.446225	-0.000051	0.026827
C	-2.543977	0.730094	0.000034	-0.009707
C	-3.463114	-0.327973	-0.000031	0.060968
C	-3.018307	-1.655910	-0.000079	-0.002944
C	-1.650684	-1.947135	-0.000123	0.044335
C	-0.734859	-0.891089	-0.000070	-0.039269
C	0.734866	-0.891085	-0.000040	0.039452
C	1.650694	-1.947129	0.000088	-0.044262
C	3.018317	-1.655898	0.000064	0.002929
C	3.463120	-0.327960	-0.000055	-0.061083
C	2.543981	0.730106	-0.000129	0.009769
C	1.181275	0.446230	-0.000053	-0.026020
C	-0.000035	2.305180	1.265877	-0.001155
C	0.000007	2.305744	-1.265512	0.001008
H	-2.901012	1.757020	0.000093	-0.000071
H	-4.528612	-0.116671	0.000012	0.000332
H	-3.742017	-2.465988	-0.000066	-0.000011
H	-1.311294	-2.979403	-0.000112	0.000221
H	1.311307	-2.979397	0.000137	-0.000221
H	3.742030	-2.465975	0.000105	0.000011

H	4.528618	-0.116657	-0.000178	-0.000332
H	2.901014	1.757031	-0.000334	0.000071
H	-0.000136	1.695111	2.174087	0.000001
H	-0.885814	2.949423	1.284944	-0.001724
H	-0.000111	1.696189	-2.174074	-0.000001
H	0.885875	2.949882	-1.284424	0.001095
H	-0.885645	2.950151	-1.284360	-0.001051
H	0.885745	2.949387	1.285108	0.000885

4-6. Reference

1. J. Kim and T. M. Swager, *Nature*, **2001**, *411*, 1030-1034.

2. Z. Zhu, T. M. Swager, *J. Am. Chem. Soc.*, **2002**, *124*, 9670-9671.

3. N. E. Jackson, B. M. Savoie, K. L. Kohlstedt, M. O. de la Cruz, G. C. Schatz, L. X. Chen and M. A. Ratner, *J. Am. Chem. Soc.,* **2013**, *135*, 10475-10483.

4. T. Lei, X. Xia. J. Y. Wang, C. J. Liu and J. Pei, *J. Am. Chem. Soc.,* **2014**, *136*, 2135-2141.

5. T. Huser, M. Yan and L. J. Rothberg, *Proc. Natl. Acad. Sci. USA*, **2000**, *97*, 11187-11191.

6. T. Sugimoto, Y. Ebihahra, K. Ogino and M. Vacha, *ChemPhysChem*, **2007**, *8*, 1623-1628.

7. T. Adachi, J. Brazard, R. J. Ono, B. Hanson, M. C. Traub, Z. Q. Wu, Z. Li, J. C. Bolinger, V. Ganesan, C. W. Bielawski, D. A. Vanden Bout and P. F. Barbara, *J. Phys. Chem. Lett.* **2011**, *2*, 1400-1404.

8. P. Y. Chen, A. Rassamesard, H. L. Chen and S. A. Chen, *Macromolecules*, **2013**, *46*, 5657-5663.

9. S. Onda, H. Kobayashi, T. Hatano, S. Furumaki, S. Habuchi and M. Vacha, *J. Phys. Chem. Lett.* **2011**, *2*, 2827-2831.

10. P. A. Dalgarno, C. A. Traina, J. C. Penedo, G. C. Bazan and I. D. W. Samuel, *J. Am. Chem. Soc.* **2013**, *135*, 7187-7193.

11. F. T. Carmona, S. Fronk, G. C. Bazan, I. D. W. Samue and J. C. Penedo, *Sci. Adv.* **2018**, *4*, eaao5786.

12. T. W. Tseng, H. Yan, T. Nakamura, S. Omagari, J. S. Kim and M. Vacha, *ACS Nano*, **2020**, *14*, 16096-16104.

13. K. Nakajima, H. Watabe and T. Nishi, *Polymer*, **2006**, *47*, 2505-2510.

14. G. Scheibe, *Angew. Chem.* **1937**, *50*, 51.

15. G. Scheibe, *Angew. Chem.* **1937**, *50*, 212-219

16. G. Scheibe, *Angew. Chem.* **1936**, *49*, 563

17. A. H. Herz, *Adv. Colloid Interface Sci.* **1977**, *8*, 237-298.

18. E. G. McRae, M. Kasha, *J. Chem. Phys.* **1958**, *28*, 721-722.

19. M. Kasha, R. Rawls, M. A. El-Bayoumi, *Pure Appl. Chem.* **1965**, *11*, 371-392.

20. F. Würthner, T. E. Kaiser and C. R. Saha-Möller, *Angew. Chem. Int. Ed.* **2011**, *50*, 3376-3410.

21. F. C. Spano, *Acc. Chem. Res.* **2010**, *43*, 429-439.

22. H. Yamagata and F. C. Spano, *J. Chem. Phys.* **2012**, *136*, 184901.

23. K. A. Kistler, F. C. Spano and S. Matsika, *J. Phys. Chem. B*, **2013**, *117*, 2032-2044.

24. H. Yamagata and F. C. Spano, *J. Phys. Chem. Lett.* **2014**, *5*, 622-632.

25. D. Bialas, A. Zitzler-Kunkel, E. Kirchner, D. Schmidt and F. Wüthner, *Nat. Commun.* **2016**, *7*, 12949.

26. A. Pirrotta, G. C. Solomon, I. Franco and A. Troisi, *J. Phys. Chem. Lett.* **2017**, *8*, 4326-4332.

27. U. Scherf and E. J. List, *Adv. Mater.* **2002**, *14*, 477-487.

28. M. Knaapila and A. P. Monkman, *Adv. Mater.* **2013**, *25*, 1090-1108.

29. E. Elmalem, F. Biedermann, K. Johnson, R. H. Friend and W. T. S. Huck, *J. Am. Chem. Soc.* **2012**, *134*, 17769-17777.

30. C. S. Fischer, M. C. Baier and S. Mecking, *J. Am. Chem. Soc.* **2013**, *135*, 1148-1154.

31. H. H. Zhang, Q. S. Hu and K. Hong, *Chem. Commun.* **2015**, *51*, 14869-14872.

32. H. H. Zhang, C. H. Xing, Q. S. Hu and K. Hong, *Macromolecules*, **2015**, *48*, 967-978.

33. H. H. Zhang, W. Peng, J. Dong and Q. S. Hu, *ACS Macro Lett.* **2016**, *5*, 656-660.

34. A. Yokoyama, H. Suzuki, Y. Kubota, K. Ohuchi, H. Higashimura and T. Yokozawa, *J. Am. Chem. Soc.* **2007**, *129*, 7236-7237.

35. S. Zhang, Z. Zhang, H. Fu, X. Li, H. Zhan and Y. Cheng, *J. Organomet. Chem.* **2016**, *825-826*, 100-113.

36. W. C. Tsoi, A. Charas, A. J. Cadby, G. Khalil, A. M. Adawi, A. Iraqi, B. Hunt, J. Morgado and D. G. Lidzey, *Adv. Funct. Mater.* **2008**, *18*, 600-606.

37. L. Grebikova, P. Maroni, B. Zhang, A. D. Schlüter and M. Borkovec, *ACS nano*, **2014**, *8*, 2237-2245.

Chapter V

Conclusion and outlook

5-1. Summary and Conclusion

The purpose of this thesis is to provide new insight into the effect of conformation and interchain interaction of PFO on its fluorescence properties. Optoelectrical properties of π conjugated polymers depend on conformation and interchain interactions. However, many details of the effect of conformation and interchain interactions are still unclear because it is difficult to distinguish between the effect of the two of them. In this thesis, we have controlled conformation and interchain interactions of PFO by external forces provided by combination of single molecule techniques.

Chapter I contains a background of light emitting polymers including basic concept of π conjugated polymers, in particular the features of polyfluorenes, as well as introduction to photophysical processes. In addition, by introducing key previous studies it was emphasized that single molecule spectroscopy is an essential technique to study the effect of conformation and interchain interactions on the photophysical properties.

In Chapter II, we systematically investigated how the processes of intrachain aggregation and oxidation affect the appearance of the g-band. To discuss the effect of aggregation, we measured fluorescence from PFO single chain in PS and PMMA matrices which were used as good- and poor-solvent for PFO, respectively. Although 27 % of PFO chain showed the g-band in PS, percentage of PFO chains showing the g-band increased to 58 % in PMMA. This result indicated that aggregation significantly affects the appearance of the g-band. To discuss the effect of oxidation on the g-band, fluorescence properties of PFO in PS solid matrix and in toluene solution were compared. In case of significant effect of oxidization on the appearance of the g-band, it can be expected that large number of PFO chains would show the g-band in toluene because molecules in liquid environment are more exposed to oxygen and are easily oxidized than in the PS. However, only 6 % of the PFO chains in toluene showed the g-band. From these results, a conclusion was drawn that aggregation has a greater effect on the appearance of the g-band than oxidation. With respect to the g-band fluorescence spectra, two different types of spectra were observed, one with a vibronic structure and a peak at around 500 nm and another one with a broad spectrum and peak at around 550 nm. Lifetime measurement

also indicated that there are two light emitting components in the green emission region, with lifetimes longer than the blue component which originates from unperturbed isolated sections of the PFO chain. Oscillator strength of the g-band obtained from lifetime and fluorescence quantum yield measurement was 100 times smaller than that of the blue component, indicating that H-aggregates and charge-transfer-like aggregates are the probable origin of the g-band.

The effects of conformation and interchain interactions in condensed state of PFO were studied using single PFO nanoparticles (PFONPs) and discussed in Chapter III. Individual (PFONPs) containing dominant fractions of PFO β-phase were mechanically compressed by applying external forces between 100 nN and 5 μN using an AFM tip to enhance interchain interaction. For forces between 100 nN ~ 1 μN, although fluorescence intensity decreased to about half of its original intensity, fluorescence spectrum and polarization dependence of PFONPs were unchanged, indicating that the β-phase conformation and its orientation were not affected. Enhanced interchain interaction without any conformational change promotes energy transfer as well as formation of quenching sites, leading to the observed decrease of intensity. To induce conformational change in PFONPs, the applied force was gradually increased up to 5 μN. After initial fluorescence quenching, fluorescence spectrum showed a blue shift and its intensity recovered to its initial value. In addition, polarization anisotropy of PFONPs during applying force of 5 μN was obviously reduced. These results indicate that applying excess force induces conformational change from ordered β-phase to randomly oriented glass-phase accompanied with increasing fluorescence intensity. Because the effective conjugation lengths of glass and β-phases are 8 ± 1 and 30 ± 12 fluorene units, respectively, a β-phase can generate about four glass-phase segments. Therefore, increasing the number of light emitting segments can contribute to increased fluorescence intensity. Although the difference of fluorescence quantum yield (PLQY) between glass and β-phase is also related to fluorescence intensity, we could not quantitatively discuss its effect because there is an ongoing controversy regarding the actual value of β-phase PLQY. However, the observed fluorescence quenching by applying force of 1 μN indicates that film morphology related to interchain interaction is one of the important

factors affecting the PLQY.

In Chapter IV, to directly control chain conformation, we performed nanofishing experiments of PFO chains. Small force peaks were only observed under photoirradiation and could be attributed to excitonic coupling between PFO segments. The average values of force at the peaks were measured with different excitation intensities of 14.2 W/ cm2 and 5.6 W/ cm2. The obtained forces were 47 ± 2 pN and 29 ± 2 pN, respectively, showing clear dependence on excitation intensity. This result indicates that the mean time (T) for which the PFO is staying in the excited state is important for the appearance of this small peak. Excitonic coupling energy J was estimated from the small peaks of the force curve and corrected by using the value of T. The obtained J was 0.82 eV which is of the same order as theoretically obtained excitonic coupling, indicating that small force peak is caused by intrachain excitonic coupling between different conjugated segments of a folded chain. To investigate the effect of conformational change on fluorescence properties, force curves and fluorescence spectra of single PFO chains were measured simultaneously. Although spectral change from green emission to blue emission was observed upon stretching the PFO chain, its timing was not correlated with an appearance of the small force peak. These results showed that the combination of SMS and nanofishing has great potential to investigate fluorescence properties and conformation of π conjugated polymers.

5-2. Outlook

π conjugated polymers have been widely studied for optoelectronic devices such as LED, solar cells. Conformation and interchain interaction are important factor to improve device efficiency. The study of Chapter II provides information of the origin of the g-band in PFs which can be useful to design highly efficient and stable luminescent PFs derivatives. In Chapter III and IV, fluorescence microscopy and AFM are combined to mechanically control interchain interaction and conformation of PFO chains. These experiments showed its great potential to investigate the effect of interchain interaction and conformation on properties. Nowadays, flexible materials and devices have attracted much attention and materials in devices is having more opportunity to be applied mechanical stress during use. Therefore, it is important to study the effect of mechanical stress on properties of π conjugated polymer and we hope that the experiment combining SMS and AFM becomes more important technique in this field. In addition, this technique can be developed to measure the conductivity of π conjugated polymer with controlling interchain interaction or conformation, providing new strategy of research.

List of Publications

Related to the Thesis

1. Intra-Chain Aggregates as the Origin of Green Emission in Polyfluorene Studied on Ensemble and Single Chain Level.
   T. Nakamura, D. K. Sharma, S. Hirata, M. Vacha, *J. Phys. Chem. C* **2018**, *122*, 8137-8146.

2. Mechanically Induced Conformation Change, Fluorescence Modulation, and Mechanically Assisted Photodegradation in Single Nanoparticles of the Conjugated Polymer Poly(9,9-dioctylfluorene)
   T. Nakamura, M. Vacha, *J. Phys. Chem. Lett.* **2020**, *11*, 8, 3103–3110.

3. Simultaneous nanofishing and SMS study of single π conjugated polymers: Towards the direct control of conformation and fluorescence properties
   T. Nakamura, S. Omagari, X. Liang, K. Nakajima, M. Vacha, *in preparation.*

Other Publication

1. Real-Time Monitoring of Formation and Dynamics of Intra- and Interchain Phases in Single Molecules of Polyfluorene
   T. W. Tseng, H. Yan, **T. Nakamura**, S. Omagari, J. S. Kim and M. Vacha, *ACS Nano* **2020**, *14*, 16096-16104.

Public appearances

1. Nanofishing of single conjugated polymer towards the study of conformation and fluorescence properties
    中村智則, バッハマーティン, 2019 年 web 光化学討論会, Zoom, 2020 年 9 月.

2. External pressure dependence of fluorescence properties of single conjugated polymer nanoparticles
    中村智則, バッハマーティン, 2019 年光化学討論会, 名古屋大学　東山キャンパス, 2019 年 9 月.

3. FLUORESCENCE PROPERTIES AND CONFORMATION OF POLYFLUORENE SINGLE CHAINS IN DIFFERENT ENVIRONMENTS
    Tomonori Nakamura, Shuzo Hirata, Martin Vacha, 81st PRAGUE MEETING ON MACROMOLECULES, Institute of Macromolecular Chemistry, Czech Academy of Sciences (IMC), Prague, Czech Republic, September, 2017.

4. 異なる媒体中におけるポリフルオレン単一鎖のコンフォメーションと発光特性
    中村智則, 平田修造, バッハマーティン, 2017 年光化学討論会, 東北大学青葉山キャンパス, 2017 年 9 月.

5. 異なるポリマーマトリックス中におけるポリフルオレン単一鎖の発光特性とコンフォメーション
    中村智則, 平田修造, バッハマーティン, 第 66 回高分子学会年次大会, 幕張メッセ, 2017 年 5 月.

Acknowledgements